

MINISTRY OF EDUCATION, RESEARCH, YOUTH AND SPORT



# THE ANNALS OF “DUNAREA DE JOS” UNIVERSITY OF GALATI

Fascicle IX  
**METALLURGY AND MATERIALS SCIENCE**

YEAR XXX (XXXV),  
September 2012, no.3

ISSN 1453-083X



2012  
GALATI UNIVERSITY PRESS



## Table of Content

<b>1. Lucica BALINT, Tamara RADU, Simion Ioan BALINT</b> - Corrosion of Composite Ferro-Niobium Layers in Cobalt Matrix.....	5
<b>2. Octavian POTECAȘU, Florentina POTECAȘU, Petrică ALEXANDRU, Francisco Manuel BRAZ FERNANDES, Rui Jorge CORDEIRO SILVA, Filipe Carlos de FIGUEIREDO PEREIRA DAS NEVES</b> - Research Regarding the Possibility of Obtaining Nitinol by Powder Metallurgy.....	9
<b>3. Simona BOICIUC, Constantin SPÂNU</b> - Modification of Surface Properties by Laser Cladding with Ni–Cr–B–Fe–Al Alloy.....	14
<b>4. Tamara RADU, Anișoara CIOCAN</b> - Electrochemical Behavior of Zinc Layers Passivated in Phosphate Solutions.....	22
<b>5. Florentina Simona ȘORCARU, Lidia BENEĂ</b> - Nanocomposite Coatings Obtained by Electro-Co-Deposition of Inert Particles with Cobalt–a Review....	27
<b>6. Carmela GURAU, Gheorghe GURAU</b> - Evolution of Copper Microstructure Subjected to Equal Channel Angular Pressing.....	36
<b>7. Ana DONIGA</b> - Influence of Niobium as Microalloying Element in 3%Si Steel Grade for Electrical Industry.....	44
<b>8. Daniela TASMA, Tănase PANAIT, Alexandrina TEODORU, Georgiana G. ROLEA</b> - Energetic and Exergetic Efficiencies of Biomass Gasification Processes.....	48
<b>9. Diana Daniela Daciana ZMARANDACHE, Rodica LUCA, Ioana-Andreea STANCIU, Cătălina FARCAȘIU</b> - The Consequences of Heavy Metals Impact on Primary Teeth.....	52
<b>10. Carmen CÎRNU, Marian BORDEI, Aurel CIUREA</b> - Evaluation of the Sonic System Efficiency for Raw Water Treatment.....	57
<b>11. Catalin Bogdan MOCANU, Tanase PANAIT, Alexandrina TEODORU, Daniela TASMA</b> - Comparison of the Efficiency of Three Types of Solar Collectors.....	63
<b>12. Viorel MUNTEANU, Viorel DRAGAN, Dan ZORLESCU</b> - Increase of BOF Converter Life by Own Slag Coating.....	67
<b>13. Elena Emanuela VALCU (HERBEI), Viorica MUSAT, Timothy LEEDHAM</b> - Thermal Decomposition of Hafnium Ethoxide-Mollecular Precursor for Hafnia Dielectric Thin Films.....	73



THE ANNALS OF "DUNAREA DE JOS" UNIVERSITY OF GALATI.  
FASCICLE IX. METALLURGY AND MATERIALS SCIENCE  
N<sup>o</sup>. 3 – 2012, ISSN 1453 – 083X

---

## **EDITORIAL BOARD**

### **PRESIDENT OF HONOUR**

**Prof. Olga MITOSERIU** - "Dunarea de Jos" University of Galati, Romania

### **EDITOR-IN-CHIEF**

**Prof. Nicolae CANANAU** - "Dunarea de Jos" University of Galati, Romania

### **EXECUTIVE EDITOR**

**Prof. Marian BORDEI** - "Dunarea de Jos" University of Galati, Romania

### **SCIENTIFIC ADVISORY COMMITTEE**

**Prof. Lidia BENEĂ** – "Dunarea de Jos" University of Galati, Romania  
**Acad. Prof. Ion BOSTAN** - Technical University of Moldova, Moldova Republic  
**Prof. Francisco Manuel BRAZ FERNANDES** - New University of Lisbon Caparica, Portugal  
**Acad. Prof. Valeriu CANTSER** - Academy of Moldova Republic, Moldova Republic  
**Prof. Jean Pierre CELIS** - Katholieke Universiteit Leuven, Belgium  
**Prof. Anisoara CIOCAN** - "Dunarea de Jos" University of Galati, Romania  
**Prof. Alexandru CHIRIAC** - "Dunarea de Jos" University of Galati, Romania  
**Assoc. Prof. Stela CONSTANTINESCU** - "Dunarea de Jos" University of Galati, Romania  
**Prof. Elena DRUGESCU** - "Dunarea de Jos" University of Galati, Romania  
**Prof. Valeriu DULGHERU** - Technical University of Moldova, Moldova Republic  
**Prof. Jean Bernard GUILLOT** – École Centrale Paris, France  
**Assoc. Prof. Gheorghe GURAU** - "Dunarea de Jos" University of Galati, Romania  
**Prof. Iulian IONITA** – "Gheorghe Asachi" Technical University Iasi, Romania  
**Prof. Philippe MARCUS** - École Nationale Supérieure de Chimie de Paris, France  
**Prof. Vasile MARINA** - Technical University of Moldova, Moldova Republic  
**Prof. Rodrigo MARTINS**–NOVA University of Lisbon, Portugal  
**Prof. Strul MOISA** - Ben Gurion University of the Negev, Israel  
**Prof. Daniel MUNTEANU** - Transilvania University of Brasov, Romania  
**Prof. Viorel MUNTEANU** - "Dunarea de Jos" University of Galati, Romania  
**Prof. Viorica MUSAT** - "Dunarea de Jos" University of Galati, Romania  
**Prof. Maria NICOLAE** - Politehnica University Bucuresti, Romania  
**Prof. Petre Stelian NITA** - "Dunarea de Jos" University of Galati, Romania  
**Prof. Pierre PONTIAUX** – École Centrale Paris, France  
**Prof. Florentina POTECASU** - "Dunarea de Jos" University of Galati, Romania  
**Assoc. Prof. Octavian POTECASU** - "Dunarea de Jos" University of Galati, Romania  
**Prof. Cristian PREDESCU** - Politehnica University Bucuresti, Romania  
**Prof. Iulian RIPOSAN** - Politehnica University Bucuresti, Romania  
**Prof. Rami SABAN** - Politehnica University Bucuresti, Romania  
**Prof. Antonio de SAJA** - University of Valladolid, Spain  
**Prof. Wolfgang SAND** - Duisburg-Essen University Duisburg Germany  
**Prof. Ion SANDU** – "Al. I. Cuza" University of Iasi  
**Prof. Georgios SAVADIS** - Aristotle University of Thessaloniki, Greece  
**Prof. Ioan VIDA-SIMITI** - Technical University of Cluj Napoca, Romania  
**Prof. Mircea Horia TIHEREAN** - Transilvania University of Brasov, Romania  
**Assoc. Prof. Petrica VIZUREANU** – "Gheorghe Asachi" Technical University Iasi, Romania  
**Prof. Maria VLAD** - "Dunarea de Jos" University of Galati, Romania  
**Prof. François WENGER** – École Centrale Paris, France



## CORROSION OF COMPOSITE FERRO-NIOBIUM LAYERS IN COBALT MATRIX

**Lucica BALINT, Tamara RADU, Simion Ioan BALINT**

„Dunarea de Jos” University of Galati

email: lbalint@ugal.ro

### ABSTRACT

*The ferro-niobium composite layers in cobalt matrix were obtained by cathode depositing from electrolyte solutions on steel base. The electrolyte included in its composition cobalt sulphate and cobalt chloride, boric acid was also added for pH stabilization. The ferro-niobium, powder with granulation smaller than 5 $\mu$ m, niobium content of 98% and 2% iron, were introduced into the electrolyte with 20g/L concentration. Electrodepositing was performed at different current densities: 615A/m<sup>2</sup>, 570A/m<sup>2</sup>, 458A/m<sup>2</sup> and the result was layers of cobalt and composite from ferro-niobium particles in cobalt matrix, with thickness varying between 50 – 90 $\mu$ m. Corrosion resistance was assessed by linear voltammetry test watching the corrosion behavior depending on composition and structure of deposited layers. The potentiodynamic polarization curve was analysed for composite layers compared with cobalt layers. From Tafel curves was determined the corrosion rate for each type of coatings.*

KEYWORDS: electrodeposition, corrosion resistance, ferro-niobium, cobalt

### 1. Introduction

Improved characteristics of cobalt layers can be made by the deposition of nickel or tungsten cobalt alloy [1] or cobalt matrix composite coatings [2].

This paper propose to obtain corrosion-resistant materials, consisting of a sheet steel support with low carbon content, covered by electrochemical method with a layer of cobalt where ferro-niobium particles were introduced.

The aim of this work was to determine the influence of current density on the kinetics of the cathodic reaction as well as composition, layers thickness and corrosion resistance of Co/ferro-niobium composite coatings. The paper describes the possibilities of electrocodeposition of ferro-niobium particles with cobalt matrix. Also, in this work, a comparative study is made of the corrosion electrodeposited cobalt and cobalt-ferro-niobium coatings.

The amount of embedded phase in the composite depends on the type bath-metal-particle combination and is governed mainly by the powder concentration in the plating bath, current density and agitation rate [2].

### 2. Experimental procedure

Composite coatings in cobalt matrix were electrodeposited from solution containing: 300 g/L CoSO<sub>4</sub>·7H<sub>2</sub>O, 50 g/L CoCl<sub>2</sub>·6H<sub>2</sub>O, and 30 g/L H<sub>3</sub>BO<sub>3</sub> [3]. Suspensions contained ferro-niobium technical particles (98%Nb) at concentrations of 20 g/L. Size of the particles was smaller than 5  $\mu$ m. To wet and distributed uniformly the particles in the electrolyte, the suspension was agitated with a magnetic stirrer with a rotation rate of 1500 rpm. Cobalt and composite ferro-niobium in cobalt matrix layers was made on steel support with chemical composition shown in Table 1.

*Table 1. Chemical composition of steel support, in %*

C	S	Mn	P	S	Al	Ti	V	Ni	Cr	Mo
0.025	0.015	0.210	0.013	0.010	0.046	0.002	0.001	0.008	0.025	0.001

Prior to the electrodeposition, the steel surfaces were polished, degreased in 100g/L NaOH, 50g/L Na<sub>2</sub>CO<sub>3</sub> and 10g/L Na<sub>2</sub>SiO<sub>3</sub> solution at 90<sup>o</sup>C, washed in distilled water, pickling in 15% HCl solution, finally rinsed again with distilled water [4]. The steel support samples as substrates and two graphite anodes were used. All electrodes were in a vertical position in the cell. The conditions for the electrochemical process was: time 60 min; pH 5; concentration of FeNb particles in bath solution was

20g/L and current density of 615A/m<sup>2</sup> (code samples S1, S4), 570 A/m<sup>2</sup> (code samples S2, S3) and 458 A/m<sup>2</sup> (code samples S5).

Composite coated samples were heat treated at 1150 °C for one hour to remove hydrogen and stimulate diffusion processes between particles and matrix [5].

The chemical composition of the layers, determined by X ray diffraction is presented in Table 2.

**Table 2.** Chemical composition of the layers

Code	Chemical composition in gravimetric percentage			
	Co	Nb	Fe	other
S1	99,01	0	0.70	bal
S2	98,87	0	0.64	bal
S3	80,2	0.17	19.64	bal
S4	77.37	0.35	22.28	bal
S5	51.81	0.97	46.32	bal

The aspect of the different areas of the two types of coatings, cobalt and cobalt-ferro-niobium, shows that niobium particles in the composite material

determined finishing texture, increase compactness, uniformity, reduce ridges dendrites and inter-dendrites space (Figure 1 and 2).



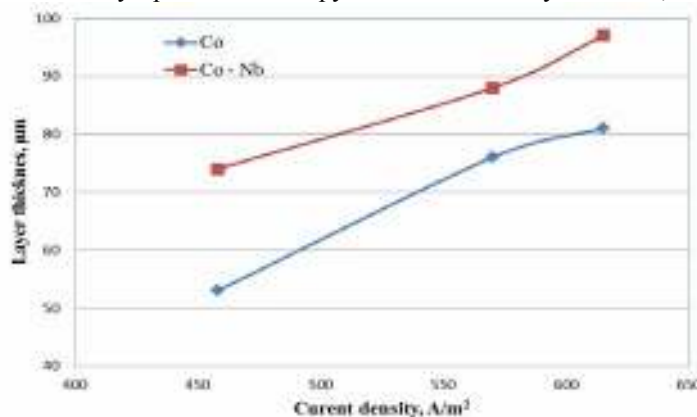
**Fig. 1.** Cobalt layer;  
current density: 570A/m<sup>2</sup>; 50X



**Fig. 2.** Co/ferro-niobium composite layers;  
current density: 570A/m<sup>2</sup>; 50X

Layer thickness of cobalt layers and composite coatings layers was measured by optical microscopy.

It was established that the thickness increases when current density increases, as shown in Figure 3.



**Fig. 3.** Layer thickness variation with current density

The corrosion behaviour was carried out with potentiostat type VOLTAMASTER 4 (PGP 201). A three electrode system with an electrochemical cell volume of 100mL was used to perform the experiments. The auxiliary electrode was a platinum sheet and the reference electrode was saturated electrode calomel (SCE).

The working electrode was the experimental samples which has an electro active area of 1cm<sup>2</sup>. Before the experiments, the samples was degreased in acetone and alcohol, rinsed with distilled water and then, dried in air. Linear voltammetry curves of the codeposited layers were measured from -1000 mV

toward the anodic direction of 500mV, with scan rate of 50mV/min. The corrosion behaviour of codeposited films has been observed by introducing them in corrosive environments: 0.1N HCl solution.

The Tafel curves were used as a method to study corrosion behaviour.

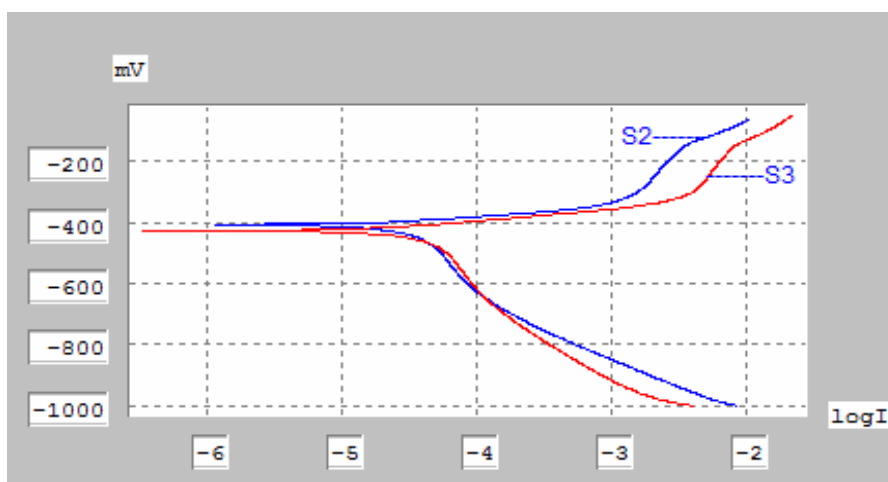
From the anodic and cathodic polarization curves the main electrochemical parameters of the corrosion process were obtained: corrosion potential  $E_{corr}$ , corrosion current density  $i_{corr}$ , polarization resistance  $R_p$  and corrosion rate  $V_{corr}$ , automatically calculated by specialized computer software – Table 3.

**Table 3.** Electrochemical parameters of the corrosion process

Code	$i_{cor}$ [ $\mu\text{A}/\text{cm}^2$ ]	$R_p$ [ $\Omega\text{cm}^2$ ]	$E$ [mV]	$v_{cor}$ [ $\mu\text{m}/\text{y}$ ]
S1	16.1084	709.62	-446,3	0.357
S2	13.6000	613.04	-408,4	0.301
S3	15.0000	597.91	-431.1	0.331
S4	9.7476	1170	-447.5	0.216
S5	4.1946	3000	-328.9	0.093

The polarization curves for cobalt coatings and Co/ferro-niobium composite coatings obtained at 570A/m<sup>2</sup> current density, are shown in Figure 4. In Figure 5 are shown the polarization curves of cobalt

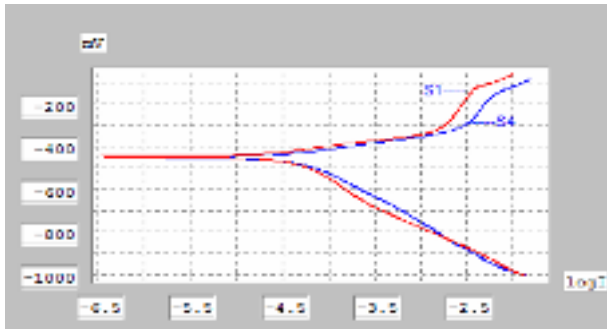
coating and Co/ferro-niobium composite layers obtained at 615A/m<sup>2</sup> current density. The polarization curves of Co/ferro-niobium composite layers obtained at different current density are shown in Figure 6.



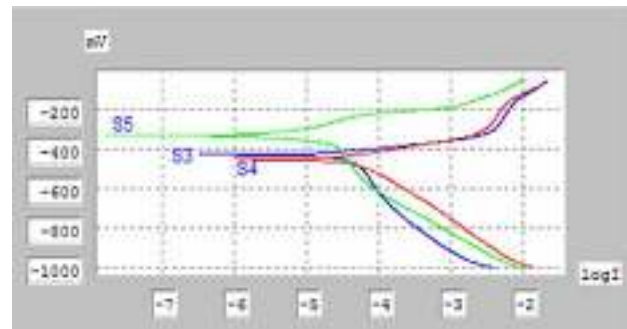
**Fig. 4.** Polarization curves of cobalt coatings and Co/ferro-niobium composite coatings, obtained at 570A/m<sup>2</sup> current density

Polarization measurements in 0.1N HCl indicate similar results of corrosion resistance for cobalt and ferro-niobium particles in cobalt matrix obtained in some conditions for electrodeposition.

As show in Figure 6, the corrosion resistance of Co/ferro-niobium composite layers increases with niobium content from the layers.



**Fig. 5.** Polarization curves of cobalt coating and Co/ferro-niobium composite coatings obtained at  $615A/m^2$  current density



**Fig. 6.** Polarization curves of Co/ferro-niobium composite layers obtained at different current density

### 3. Conclusion

- Composite thin films which consist of ferro-niobium particles in a cobalt matrix were deposited on a steel substrate using the electrocodeposition method.
- The surface morphology of the cobalt-ferro-niobium coatings is different from the pure cobalt coatings. The presence of niobium particles in composite layers determined the finish texture, uniform ridges dendrites and diminishing interdendrites space.
- The thickness of the layer increases non-linearly with increasing current density. The best value of thickness corresponds to composite coatings obtained at  $615A/m^2$ .
- Polarization measurements in 0.1N HCl indicate a similar results of corrosion resistance for cobalt and ferro-niobium particles in cobalt matrix obtained in some conditions for electrodeposition.
- Generally, the corrosion resistance of cobalt-ferro-niobium composite layers increased with niobium content from composite layers.

### References

- [1]. **A. Bodaghi, J. Hosseini** - Corrosion Behavior of Electrodeposited Cobalt-Tungsten Alloy Coatings in NaCl Aqueous Solution. *Int. J. Electrochem. Sci.*, 7 (2012) 2584 - 2595 [www.electrochemsci.org](http://www.electrochemsci.org)
- [2]. **E. Rudnik, L. Burzyńska, W. Jakubowska**, Codeposition of SiC particles with cobalt matrix, *Journal of Achievements in Materials and Manufacturing Engineering* 41/1-2 (2010) 195-199.
- [3]. **L. Balint, T.Radu, O. Mitoseriu, S. Balint, A. Doniga** - Ferroniobium composite coatings in cobalt matrix on steel support, obtained by electrochemical deposition Proceedings of the International Metallurgy and Materials Congress, may 2000, Istanbul, Turkey.
- [4]. **Lucica Balint, Simion Balint, Florentina Potecaşu** - Soft magnetic composite by ferrotitanium particles in cobalt matrix, International Conference on Materials Science and Engineering 24-26 February 2005, Brasov – Romania, p. 97.
- [5]. **L. Balint, S. Balint, T. Radu, E. Stratulat** - Analysis of diffusion processes at interface cobalt –steel sheets, *The Annals of 'Dunarea de Jos' University of Galați, Fascicle IX. Metallurgy and Material Science*, 2003, no. 2, p.78-84.





## RESEARCH REGARDING THE POSSIBILITY OF OBTAINING NITINOL BY POWDER METALLURGY

Octavian POTECAȘU<sup>1</sup>, Florentina POTECAȘU<sup>1</sup>, Petrică ALEXANDRU<sup>1</sup>,  
Francisco Manuel BRAZ FERNANDES<sup>2</sup>, Rui Jorge CORDEIRO SILVA<sup>2</sup>,  
Filipe Carlos de FIGUEIREDO PEREIRA DAS NEVES<sup>2</sup>

<sup>1</sup>Center of Nanostructures and Functional Materials, "Dunărea de Jos" University of Galați

<sup>2</sup>CENIMAT/Materials Science Department, Nova University of Lisbon, Caparica, Portugal

email: [opotec@ugal.ro](mailto:opotec@ugal.ro)

### ABSTRACT

*In the paper the obtaining of nitinol by pressing and sintering of a mixture of nickel and titanium powders is presented. The fabrication of NiTi alloys by powder metallurgy allows avoiding the usual problems related to classical casting obtaining methods (problems related to defects caused by segregation or excessive growth of the grains), it also assures an exact control of the chemical composition and offers the possibility of manufacturing a variety of components very close to their final shape.*

*Although the advantages of manufacturing products by powder metallurgy are certain, the first research presented in this paper in the case of nickel and titanium powders have showed some unwanted aspects related to powder metallurgy processing which are yet to be resolved, that is, the high oxide content, the high content of secondary phases, also the difficulty of obtaining dense materials. The main conclusion is that it is imperative to do the sintering in a protecting system (if possible in vacuum), because of the high content of oxygen observed in the measured sintered products.*

KEYWORDS: powder metallurgy, Ti powder, Ni carbonil, NiTi, sintering, X-ray diffractometry, SEM

### 1. Introduction

Nitinol is a group of materials defining the alloys of the Ni-Ti family situated around the stoichiometric concentration (50% Ni). Nitinol, the material discovered in 1959, at the Naval Ordnance Laboratory (now Naval Surface Warfare Center) is the first commercial name which became the most known in time and accepted with the same name in the materials science, after the binary Ni-Ti system that it belongs to [1][2].

The first experiments related to shape memory phenomenon (pseudo-elasticity, simple shape memory effect, double ways shape memory effect, vibration damping effect, pre-martensitic effects etc.) have been made on monocrystals. Because monocrystals are easier to obtain on copper based alloys, these were the experimental materials which allowed, in the 70's, to establish the microstructural origin of the shape memory phenomenon, and also

the connection between those and the martensitic transformation [3].

The special properties of the shape memory alloys make them extremely important in present, through their extraordinary usage potential in high tech domains as biomedical technologies, nanoelectronic systems, microelectronic systems or the complex bio and optoelectromechanical ones [4].

The technology of obtaining sintered products is fundamentally different from the classical metallurgical technologies, where the semi-products are manufactured through casting of melted metals and alloys, which, afterwards, are subjected to mechanical processing (forging, lamination, dye pressing etc.); thus getting to the end product involves a big number of difficult operations, expansive and long lasting.

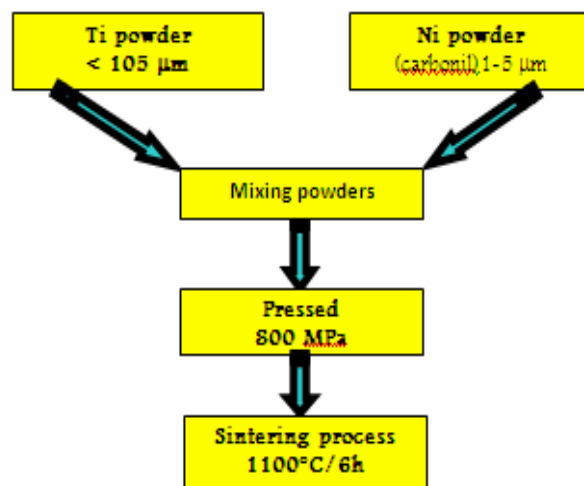
In powder metallurgy the products are usually obtained without ever having the materials in liquid phase.

The complexity of powder metallurgy stands in the interaction between three necessary factors in order to make the end product. These factors are: powder, pressing and sintering. A high level of knowledge of the relationship between these ingredients is of utmost importance in order to make components with high resistance and in order to carry on requests regarding quality and costs. Recently, two new processing method using powder metallurgy named MARFOS (mechanically activated reactive forging synthesis) and MARES (mechanically activated reactive extrusion synthesis) have been studied in order to produce raw NiTi alloys, being considered promising technologies for producing raw intermetallic compounds [5].

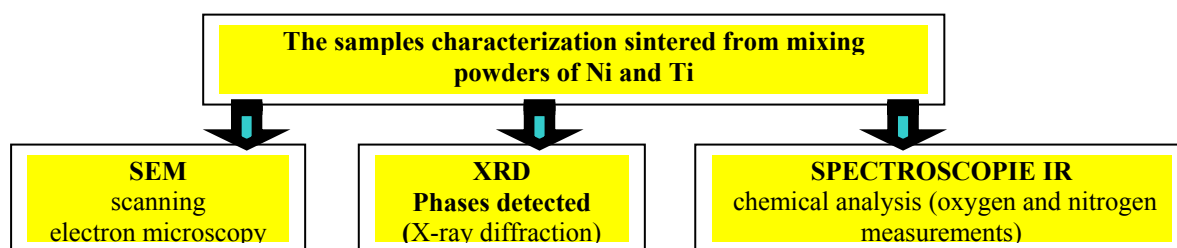
## 2. Experimental results

The samples analyzed in this paper were made according to the diagram shown in Figure 1, starting from raw materials from metallic powders of nickel and titanium. From the homogenized mixture of the two types of metallic powders were realized by

compression products that undertook afterwards a sintering process.



*Fig. 1. Processing scheme of the nitinol samples obtained from metallic powders*

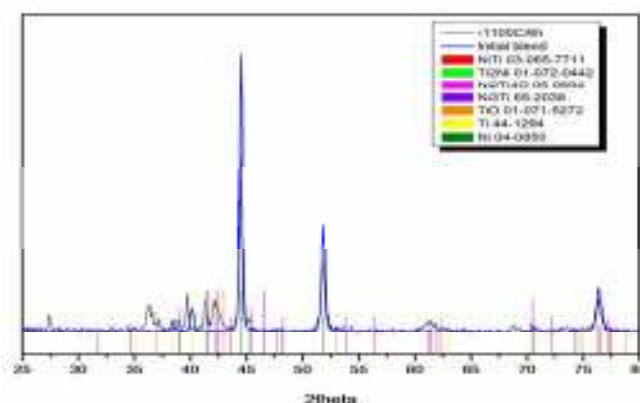


*Fig. 2. Characterization of the nitinol samples obtained by sintering the mix of the metallic powders (according to the process presented in fig. 1)*

The nitinol samples made after mixing, homogenizing, compressing and sintering the powders had a complex characterization in order to understand the nature of the resulted phases after diffusion (Figure 2).

## 2. Results and Discussion

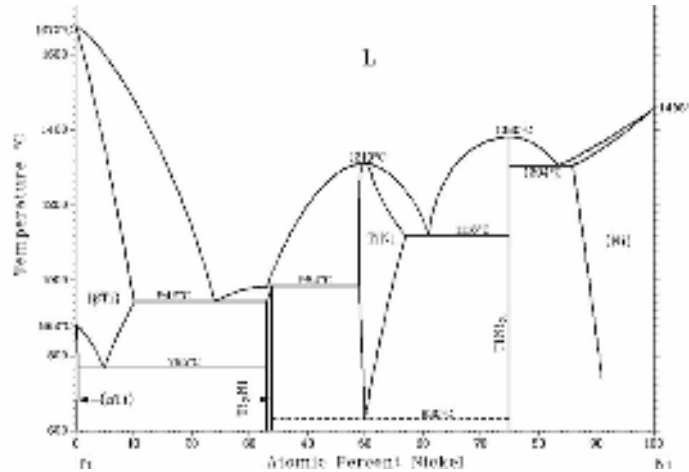
The investigation through X-ray diffraction (XRD) presented in Figure 3, was made in order to identify the phases that came out after the diffusion processes in the sintered compressed products from the powder mix.



*Fig. 3. Phases detected (by XRD)*

One can notice that if, after the pressing step the phases were Ni and Ti, after the sintering step intermetallic compounds and oxydic phases were formed: **NiTi**, **Ti<sub>2</sub>Ni**, **Ni<sub>3</sub>Ti**, **Ni<sub>2</sub>Ti<sub>4</sub>O**, **TiO**, **NiO**. Analyzing the binary equilibrium diagram Ti-Ni (Fig. 4), that

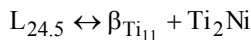
gives back the areas of the phasic stability for the Ti-Ni alloys from liquid state to the environment temperature, one can notice that similar phases are being formed after invariant reactions (except for the oxydic ones).



**Fig. 4.** Scheme of the Ti-Ni binary phase diagram

The invariant transformations that take place of Ti-Ni binary phase diagram are:

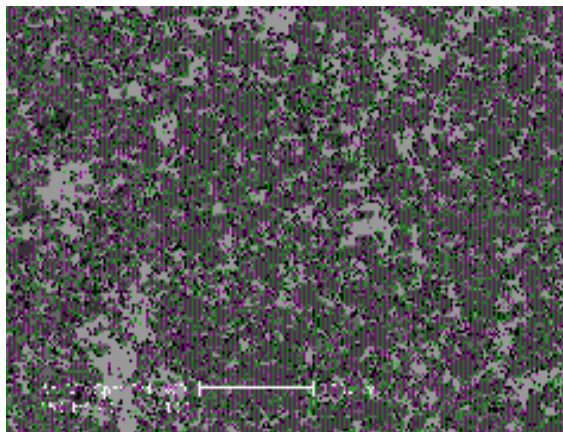
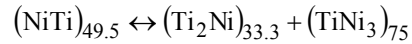
- three eutectic reactions:



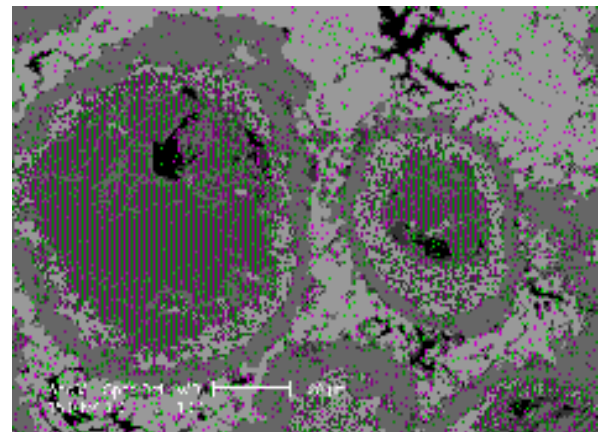
- one peritectic reaction:



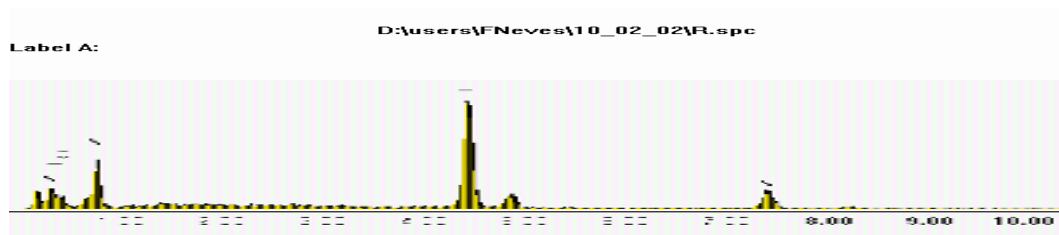
- one eutectoid reaction:



a)



b)



Total area of Fig. 5a

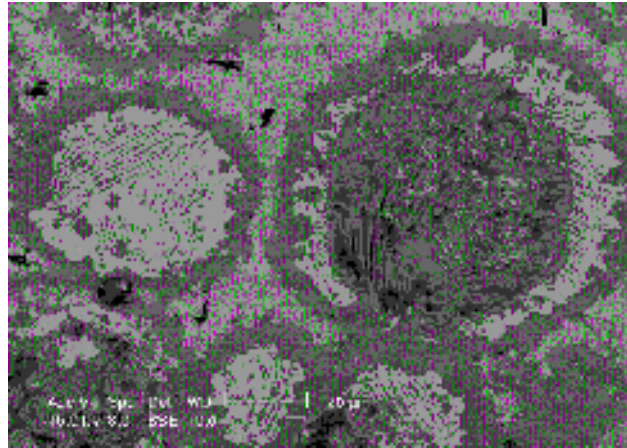
**Fig. 5.** The SEM microstructure of the sintered products from Ni-Ti powder mix (a, b)

The explanation of forming the oxydic phases was cleared out after making the spectral analysis, chemical analysis (oxygen and nitrogen measurements). Oxygen and nitrogen contents (wt%) (LECO - The ONH836 Oxygen/Nitrogen/Hydrogen Elemental Analyzer is designed for wide-range measurement of oxygen, nitrogen, and hydrogen content of inorganic materials, ferrous and non-ferrous alloys, and refractory materials using the inert

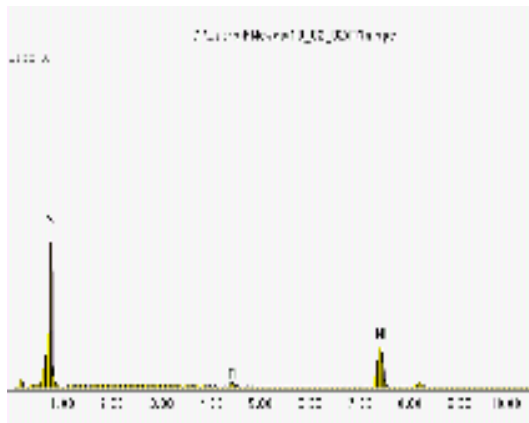
gas fusion technique). As-pressed: oxygen 0.280.03; nitrogen 0.0410.007. As-sintered: **oxygen over 15 (IR cell saturated)**; nitrogen 2.5490.358.

The results of the SEM analysis of the sintered compressed products in the given conditions are presented in Fig. 5.

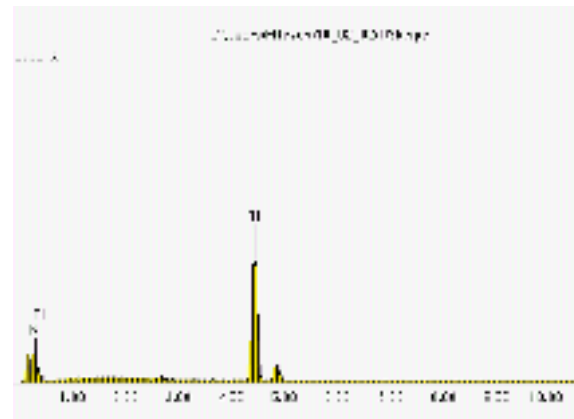
Figure 6 presents the chemical composition of 4 zones with different microstructures resulted during sintering after diffusion.



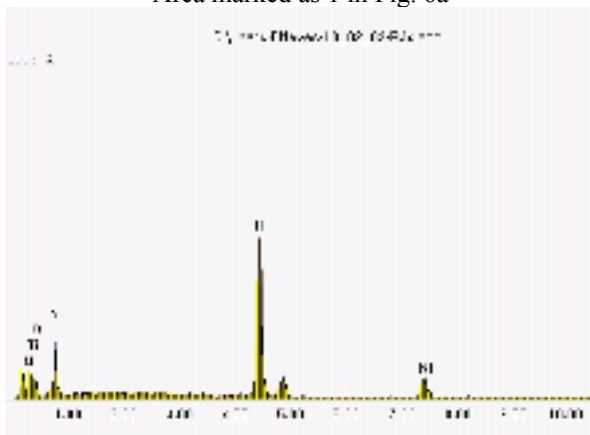
a)



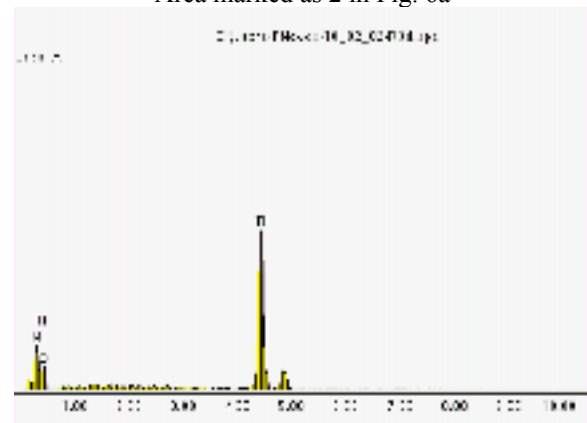
Area marked as 1 in Fig. 6a



Area marked as 2 in Fig. 6a



Area marked as 3 in Fig. 6a



Area marked as 4 in Fig. 6a

**Fig. 6.** SEM results sintered material



### 3. Conclusions

The processing of Ni and Ti metallic powders of through technologies specific to MP lead to forming some materials known as nitinol.

The nitinol obtaining technology must be improved as the XRD, spectral and SEM analysis highlighted in the sampled obtained after sintering similar inter-metallic compounds with those from the binary system Ti-Ni (NiTi, Ti<sub>2</sub>Ni, Ni<sub>3</sub>Ti) and also oxydic phases (Ni<sub>2</sub>Ti<sub>4</sub>O, TiO, NiO).

The main conclusion of the present study is that it is required that the future sintering step to be made in a protection system (preferably vacuum) due to the high levels of oxygen detected in the sintered samples.

### References

[1]. Schumann, H. – *Metallurgie fizică* (traducere din limba germană), Editura Tehnică, București, (1962).

[2]. George B. Kauffman – California State University, Fresno Fresno, CA 93740-0070 ISAAC MAYO College of Veterinary Medicine Cornell University Ithaca, NY 14853-6401, The Story of Nitinol: The Serendipitous Discovery of the Memory Metal and Its Applications, The Chemical Educator 3/Vol. 2, No. 2, (1996) SPRINGER-VERLAG NEW YORK, INC.

[3]. Frémond, M. and Miyazaki, S. – Shape Memory Alloys. CISM Courses and Lectures, Springer, Wien-New York, (1996), ISBN 3-211- 82804-4.

[4]. C.M. Craciunescu – *Shape memory alloys micro and nanoengineering*, Ed. Politehnica, Timisoara, Romania, (2005).

[5]. F. Neves, F.M. Braz Fernandes, I. Martins, J.B. Correia, M. Oliveira, E. Gaffet, T.-Y. Wang, M.Lattemann, J. Suffner and H. Hahn - *Nonconventional production technologies for NiTi shape memory Alloys* - ESOMAT 2009, 05023 (2009), DOI:10.1051/esomat/200905023.

[6] Y. Sutou a, T. Omoria, J.J. Wang b, R. Kainumaa, K. Ishida – *Characteristics of Cu-Al-Mn- based shape memory alloys and their applications*, Materials Science and Engineering A 378 (2004) 278-282

[7]. F. Neves, I. Martins, J.B. Correia, M. Oliveira, E. Gaffet - *Intermetallics* 15, 1623 (2007)

[8]. F. Neves, I. Martins, J.B. Correia, M. Oliveira, E. Gaffet, *Intermetallics* 16, 889, (2008).

[9]. Wayman, C.M., *Deformation - Mechanisms and other characteristics of shape memory alloys*, Shape Mem. Eff. All., (Perkins, J., ed.), Plenum Press, (1975), 1-27.





## MODIFICATION OF SURFACE PROPERTIES BY LASER CLADDING WITH Ni–Cr–B–Fe–Al ALLOY

**Simona BOICIUC, Constantin SPÂNU**

„Dunarea de Jos” University of Galati

email: [simonaboiciuc@yahoo.com](mailto:simonaboiciuc@yahoo.com)

### ABSTRACT

*The paper is focused on modification of surfaces properties by laser cladding. To follow the corrosion behavior in different media of laser cladding layers made of nickel based alloy Ni - Cr - B - Fe - Al. It was studied using the potentiodynamic method. Elasto – plastic behavior of the assembly base material - deposited layer was monitored by using sliding indentation, in dry friction conditions. It was determined the bearing capacity of surfaces.*

KEYWORDS: laser cladding, microstructure, potentiodynamic method, sliding indentation

### 1. Introduction

Laser cladding is predominantly used to obtain highly resistant layers to wear and corrosion. Laser cladding was defined as a process used to melt, with a laser beam on a substrate, a material having different physical and mechanical properties. In order to maintain the original properties of the material deposited, only a very thin layer of the substrate must be melted to obtain the minimum dilution (0.5 - 3%) of the metallurgical bond of the additional material with the substrate.

Both structure and properties depend on the melting temperatures of the support and the material deposited, the chemical composition and they may vary by applying various thermal regimes and granulation of the powder added [1, 2].

Thus it was found that by altering the power density, duration of laser action, feed speed, powder feed speed, granulation and powder density, the complex of physical – mechanical properties within the superficial layers of preset size. Also a good quality of the layers deposited implies lack of cracks, of porosity, good bond with the substrate and a low dilution of the material covering the substrate and minimum roughness.

Corrosion is a real calamity for facilities and equipment in all industry sectors, causing premature removal from service, interruptions, damaging for the production processes and especially the loss of huge amounts of metal.

Thus, in parallel with the development of industry there is concern for the study of corrosion

processes and the development of new methods of corrosion protection.

To provide a complete characterization of the laser cladded layers with Ni alloys, corrosion behavior was studied using the potentiodynamic method (polarization curves plotting) for determining the corrosion potential ( $E_{cor}$ ), maximum corrosion current intensity ( $I_{cor}$ ) and polarization resistance ( $R_p$ ).

The potentiodynamic tests aim to plot the polarization curves by varying the current density according to the potential. Proportionality between potential and current density arises from the overlap of the two cathodic and anodic processes, both obeying the logarithmic laws. In a corrosion process, the two reactions occur on the same metal surface, equipotential so that the experimental measurements will give values that correspond to the potential and anodic and cathodic current densities, i.e. mixed values. Mixed potential and corresponding current intensity are also called corrosion potential, and corrosion current density, respectively.

The potentiodynamic method implies modification of the electrode potential continuously at a preset scanning speed. The sliding indentation test is today widely used, especially by the coating industry and by coating development laboratories, as well as in research for evaluating the tribological properties of coatings and other hard surfaces. In the sliding indentation test, an indenter (in this case a ball bearing) is pressed by a normal force on the workpiece surface, while being pushed by a force tangential to it.

A material behaviour within an elasto-plastic

range depends on: construction parameters (shape, dimensions) and operating parameters (kinematics, energy, environmental) of the contact; the surface layer parameters - microgeometry, metallurgical characteristics (chemical composition, purity, microstructure) and mechanical parameters (hardness, tension) [6].

It was found [7, 8, 9, 10, 11] that the value of the hertzian stress at which plastic deformation occurs in contact increases with the surface hardness. Also, the larger the frictional forces, the lower the plastic deformation where the seizing tendency occurs.

The choice of surface hardening processes, suitable to a certain material, is an important way to increase the bearing capacity of the contacting surface and reduce the tendency of seizing. Thus laser cladding with alloy Ni - Cr - B - Fe - Al constitutes an effective way to increase the surface hardness that directly affects their behavior to plastic deformation.

Characterization of the surface layers can be highlighted by an installation with a point contact sphere-plane which provides a sliding indentation in dry friction conditions. The evolution of the plastic deformation of the material tested when applying various normal forces led to the determination of the bearing capacity.

According to the literature [1, 2, 3, 4] with the surface hardened materials transition from elastic to plastic deformation is continuous, so that the strain at the beginning of the plastic deformation ( $\delta_p = 0.1$  to  $10 \mu\text{m}$ ) can be expressed with an acceptable approximation by Hertz's equations.

For the point contact sphere-plane, the features are:

- Hertzian pressure:

$$P_{\max} = \left( \frac{6F \cdot E^*}{\pi^3 \cdot R^2} \right)^{1/3} \quad (1)$$

where:  $F$  – normal force,  $E^*$  - reduced elasticity module,  $R$  – indenter radius,  $P_{\max}$  max pressure at Hertzian contact

$$E^* = \frac{10^5}{0.85}, \quad \frac{1}{E^*} = \frac{1-\nu_1^2}{E_1} + \frac{1-\nu_2^2}{E_2} \quad (2)$$

where:  $\nu_1$ ,  $\nu_2$  - Poisson coefficients,  $E_1$ ,  $E_2$ , elasticity modules of the indenter and surface being tested.

The present study is focused on the corrosion behavior in different media of laser cladding layers made of nickel based alloy Ni - Cr - B - Fe - Al, and of the elasto – plastic behavior of some laser cladded samples with alloys of Ni - Cr - B - Fe - Al (code A

and B) and the base material (code Mb) made from steel improved 1C45, SR EN 10083-1: 2007.

There were determined the pressures where the elasto – plastic transition is initiated for the three samples analyzed.

## 2. Experimental conditions

„Alliages Speciaux 7569 Alliajes Frittes, France” powder, with the following chemical composition 8.9%Cr; 4.5%Fe; 5.1%B; 2.4%Al; 0.6%Cu; rest Ni [5, 6], was used for cladding.

Grain fractions in the 80-90 $\mu\text{m}$  range were screened separately in order to be used as addition material. The powder had a spherical shape which provided a fluid flow of addition material through the injection system. Before the addition material feeding into the system tank, the power was dried at 110°C temperature for 15 minutes.

Cladding was performed on a 1C45, SR EN 10083-1:1994 steel sample in refined conditions.

Lab experiments were performed by a Laser GT 1400W (Romania) type CO<sub>2</sub> continuous wave installation with x-y-z coordinate running table and computer programmed running, provided by powder injection system on the laser melt surface, which exists at S.C. UZINSIDER ENGINEERING Galați.

For laser cladding a 1.8 mm diameter laser beam was used, with 1150 W power, 7.5 mm/s sweeping speed, which cladded parallel overlapped stripes with 1.5 mm cross travel pass. Addition material flow was 105 mg/s. Final thickness of the cladding layer was 2.07 mm resulted by 4 layers overlapping.

Determining susceptibility to corrosion was achieved at room temperature (24°C) using a Voltalab 21 system connected to a computer using a VoltaMaster 4 software for experimental data processing.

The potentiostat is connected to the electrochemical cell by three electrodes: reference electrode, auxiliary electrode and working electrode. In the experimental determinations, as reference electrode was used a saturated calomel electrode Hg/Hg<sub>2</sub>Cl<sub>2</sub>/saturated K<sub>2</sub>SO<sub>4</sub>, (SCE=+241 mV/EHS), and as auxiliary electrode (counterelectrod) a platinum electrode.

The working electrode, that is the laser cladding samples on nickel base has been previously prepared, polished, made shiny and degreased in accordance with ASTM G1 standard. To study only the behavior of the laser deposited layers non treated areas were covered with a protective lacquer. Also, the surface submerged into solution was measured and data were entered in the program.

Thus the polarization curves were obtained by means of which the corrosion behavior of Ni based alloy by laser cladding was assessed. Elasto – plastic behavior of the assembly base material - deposited layer was monitored by using sliding indentation, in dry friction conditions. There were determined the pressures where the elasto – plastic transition is initiated for the three samples analyzed.

### 3. Experimental results and discussions

Corrosion testing of each sample began with monitoring the corrosion potential (open potential circuit - OCP) after immersing samples in the test solution until it reached a stationary value.

Table 1 shows the results of corrosion of the laser deposited layers on Ni alloy base.

**Table 1.** Results of corrosion of the laser deposited layers on Ni alloy base.

Corrosion environment	Parameters achieved							
	E (i=0)	R <sub>p</sub>	I <sub>cor</sub>	B <sub>a</sub>	B <sub>c</sub>	Corrosion	Initial mass	Final mass
	[mV]	[Ω.cm <sup>2</sup> ]	[mA/cm <sup>2</sup> ]	[mV/dec.]	[mm/year]	[g]		
NaOH, 1N	-342.3	245.66	0.03821	34.9	- 56.8	0.01304	2.7709	2.7687
NaCl, 3%	-965.7	315.55	0.22932	438	- 269	0.07826	2.9564	2.9527
HCl, 1N	-505.3	24.65	0.45619	55.70	- 48.4	0.15569	2.8068	2.8016
H <sub>2</sub> SO <sub>4</sub> 1N	-472.8	6.18	2.066408	82.5	- 45.7	0.70525	2.7687	2.7417

Note: E – corrosion potential; R<sub>p</sub> – polarization resistance; I<sub>cor</sub> – intensity of corrosion current; B<sub>a</sub>, B<sub>c</sub> – correspond to constants Tafel for anodic and cathodic reaction.

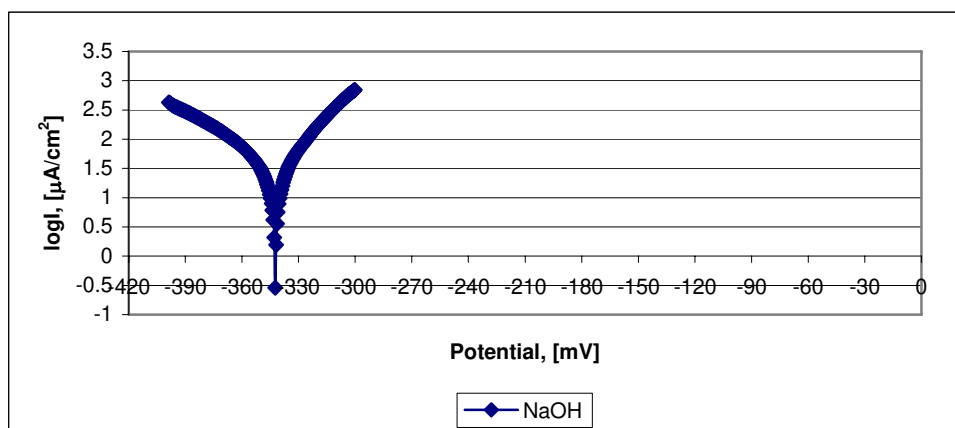
From Table 1 it may be noted that laser cladding layer based on Ni alloy is corrosion resistant in environment 1N NaOH and H<sub>2</sub>SO<sub>4</sub> 1N presents the lowest resistance therefore it causes the highest corrosion rate. The corrosion caused by Cl<sup>-</sup> ions is weaker than that caused by SO<sub>4</sub><sup>2-</sup> ions therefore in these cases a lower rate of corrosion is reported. Polarization resistance R<sub>p</sub> is representative for the degree of protection of layer deposited on the steel surface. The higher the polarization resistance, the more resistant the alloy and lower the I<sub>cor</sub>. Thus we can see that the polarization resistance is higher in NaOH and NaCl environments and I<sub>cor</sub> is lower which indicates that coating with Ni based alloy resists

corrosion in these environments, a fact also visible from the values of the corrosion rate.

Corrosion potential and corrosion current intensity characterize the general corrosion resistance. The more electropositive corrosion potential values and the lower the I<sub>cor</sub> values of the corrosion current intensity, the higher the overall corrosion resistance. We can therefore conclude that the deposit features good behavior in NaOH environment.

The polarization curves provide additional information on the corrosion behavior of these laser deposited layers.

Fig. 1 shows the Tafel curve resulting from corrosion in NaOH 1N.



**Fig. 1.** The Tafel curve - NaOH, 1N environment

Analyzing Fig. 1 we can see that in this solution a general corrosion may occur. On the alloy surface no protective passive layer is formed.

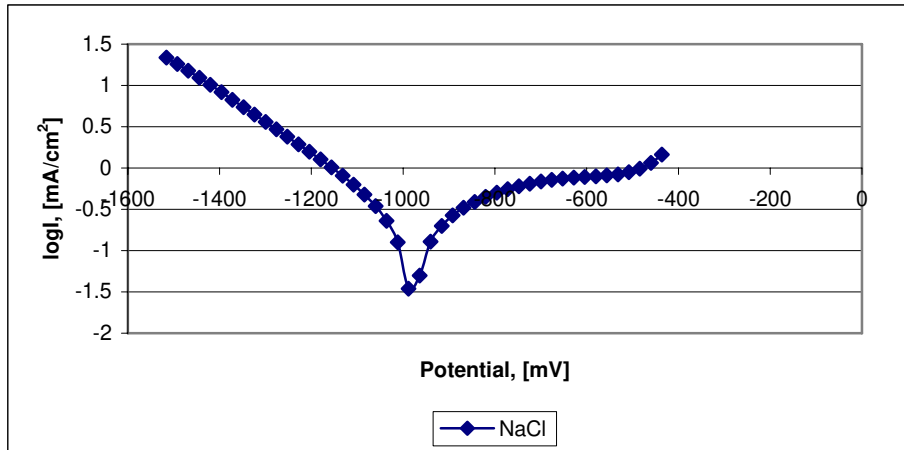
Fig. 2 shows the Tafel curve resulting from corrosion in NaCl 3%. Fig. 2 shows that the nickel based deposition resists corrosion on a wide range of



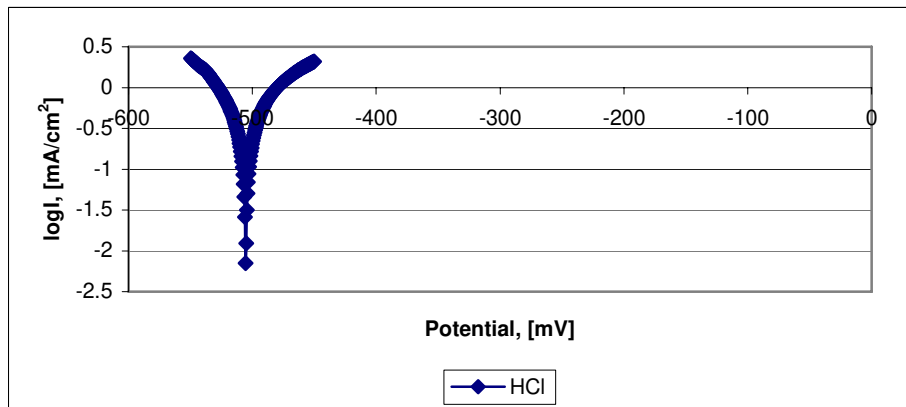
potential. This may undergo localized corrosion (pitting) caused by the chloride ions.

Fig. 3 illustrates the Tafel curve resulting from corrosion in HCl 1N. Looking at Fig. 3 it can be noticed the presence of widespread high-speed corrosion can be noticed.

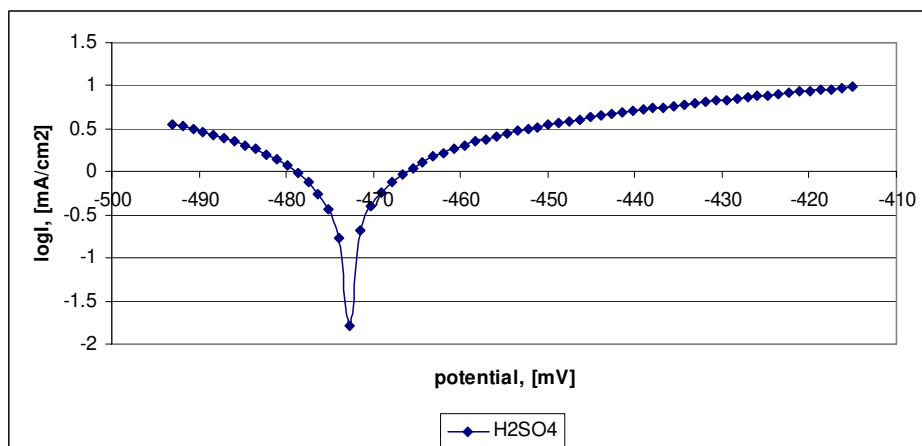
Fig. 4 illustrates the Tafel curve resulting from corrosion in H<sub>2</sub>SO<sub>4</sub> 1N. Fig. 4 reveals a general corrosion. Analyzing Figures. 1, 2, 3, 4 it may be noticed that the laser cladding with Ni-alloy layer is corrosion resistant in environment 1N NaOH and in H<sub>2</sub>SO<sub>4</sub> 1N environment features the lowest resistance.



*Fig. 2. Tafel curve - NaCl, 3% environment*



*Fig. 3. Tafel curve - HCl, 1N environment*



*Fig. 4. Tafel curve - H<sub>2</sub>SO<sub>4</sub>, 1N environment*

Porosity and inclusions may play an important role on the corrosion behavior when they are frequent and high enough. Inclusions facilitate formation of micro-corrosion cells on the surface of the sample which worsens its resistance to corrosion. If inclusions are high enough local corrosion will occur. Influence of porosity on the layer corrosion resistance consists of a long process and their effect at the beginning of corrosion is not important until porosities are not penetrating. The presence of porosity can weaken the cohesion forces within the layer, resulting in a greater mass loss under the action of the electrolyte. In principle, the lower the number of defects on the surface, the greater its resistance to corrosion. Data presented in the literature [3, 4, 5] indicate that corrosion of the Ni-base alloy coating occurs first around the particles that were not melted during deposition and around defects such as pores, inclusions and micro cracks, being followed by its propagation along the paths formed by pores, micro cracks or lamellar structure, further causing exfoliation.

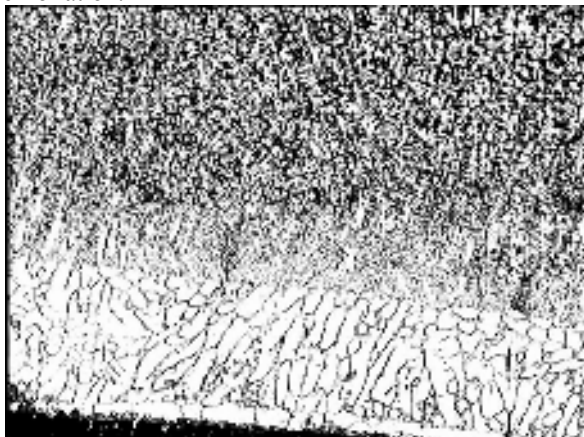
Adjusting the coating parameters to reduce the electrochemical non uniformities or the pore coating may increase the layer resistance to corrosion.

Microstructures of the mark sample and the layers subject to corrosion layers are presented in Figures 5, 6, 7, 8, 9.

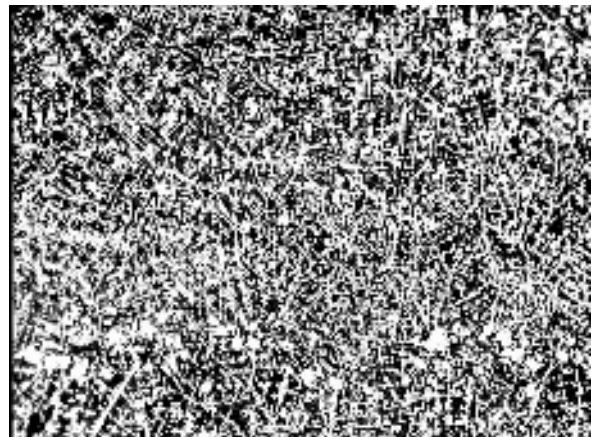
Fig. 5, 6, 7, 8, 9 indicate the presence of a columnar dendritic fine structures of the deposit containing nickel-based solid solution and Eutectic colonies of borides (NiB, Ni<sub>2</sub>B, CrB, Cr<sub>3</sub>B<sub>4</sub> and FeB), the main hardening phase being CrB.

The presence of corrosion at the boundary of the grain could also be observed in some areas.

To determine the bearing capacity were made series of marks on each specimen. For this type of testing, the mobile tribo-element (ball) is subject to two forces: one normal on the fixed tribo-element and one tangential to its surface. Initially the normal force is applied, the ball making a plastic deformation, and then the tangential one resulting a trace in the form of an elongated groove.



a



b

**Fig. 5.** Microstructure of the laser cladding layer on Ni based alloy, mark sample; a- layer base, b-layer cross section (x500). Electrolyte attack, solution 50% HNO<sub>3</sub>



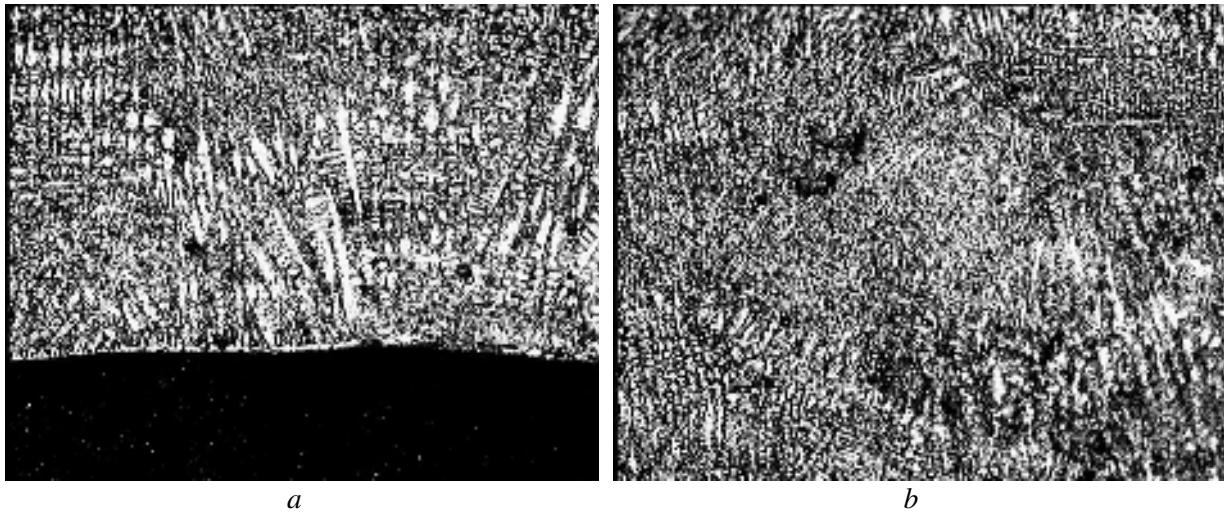
a



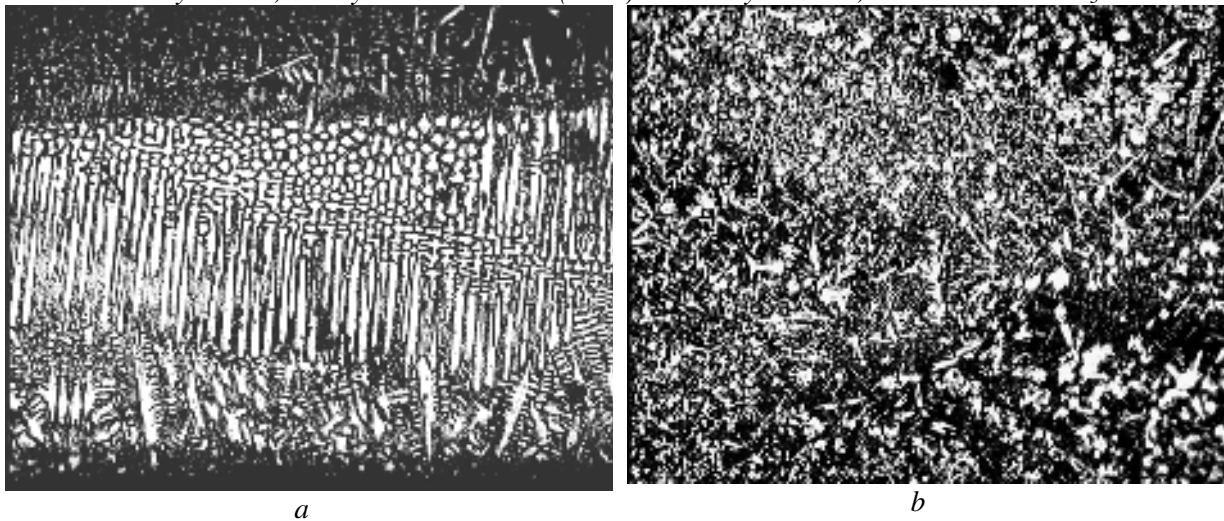
b

**Fig. 6.** Microstructure of the laser cladding layer, subjected to corrosion in NaOH, 1N; a - layer base, b - layer cross-section (x500). Electrolyte attack, solution 50% HNO<sub>3</sub>

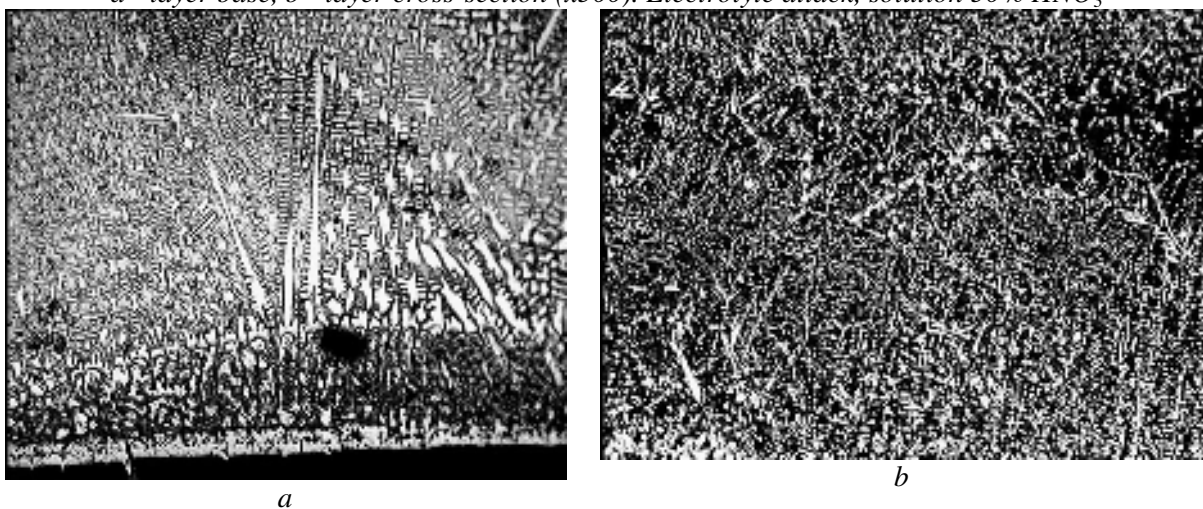




**Fig. 7.** Microstructure of the laser cladding layer, subjected to corrosion in NaCl, 3%;  
*a* - layer base, *b* - layer cross-section (x500). Electrolyte attack, solution 50% HNO<sub>3</sub>



**Fig. 8.** Microstructure of the laser cladding layer, subjected to corrosion in HCl, 1N;  
*a* - layer base, *b* - layer cross-section (x500). Electrolyte attack, solution 50% HNO<sub>3</sub>



**Fig. 9.** Microstructure of the laser cladding layer, subjected to corrosion in H<sub>2</sub>SO<sub>4</sub>, 1N;  
*a* - layer base, *b* - layer cross-section (x500). Electrolyte attack, solution 50% HNO<sub>3</sub>

The indenter speed is 0.2 mm/s, diameter  $\phi$  12.675mm, is made from Rul 1 (SR EN ISO 683-17:2002), hardened and annealing steel. After each test, the ball bearing has been replaced and degreased. Before carrying out any test, the sample surfaces have been degreased with alcohol, to provide conditions for dry friction. The normal forces  $F_N$ , used for indentation were:  $F_1 = 2.886\text{kN}$ ;  $F_2 = 4.330\text{kN}$ ;  $F_3 = 5.773\text{kN}$ ;  $F_4 = 7.216\text{kN}$ . Roughness  $R_a$ , as measured by a roughness gauge Surtronic 3+, is  $R_a \approx 0.210\mu\text{m}$  for all surfaces. Max. pressures obtained by relation (1) for the normal forces used are given in Table 2. The graphical representation of the variation of plastic deformation of the depth profile depending on

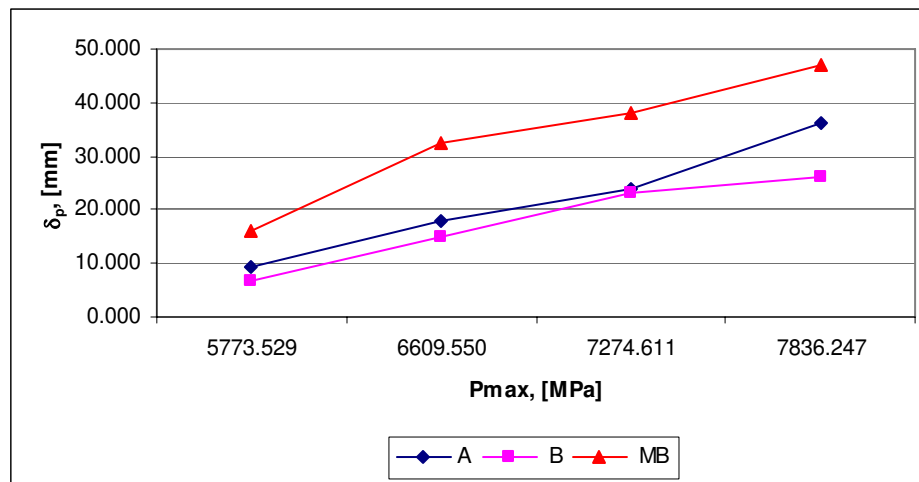
Hertzian pressure  $P_{\max}$  in Figure 10 shows the higher behavior of laser deposited layers to plastic deformation.

For the experimental data obtained, there were determined regression curves showing the dependence of plastic deformation given by the Hertz pressure under dimensionless form on the bearing capacity values for  $\delta_p/R < 0.001$ , where  $\delta_p$  is the trace depth, and R the indenter radius.

Table 3 provides the regression coefficients for the materials investigated which allowed for the determination of the max pressure when elasto-plastic transition is initiated.

**Table 2.** Maximum pressure obtained for the normal strains applied

$P_{\max}$ [MPa]	Normal force, $F_N$ [kN]
5773.529	2.886
6609.550	4.330
7274.611	5.773
7836.247	7.216



**Fig. 10.** Variation of plastic deformation of the depth profile depending on Hertzian pressure

**Table 3.** Determination of the max pressure when elasto-plastic transition is initiated

Sample code	Function	Coefficients				$P_{\max}$ [MPa]
		a	b	c	d	
MB	$y=(a+bx)/(1+cx+dx^2)$	185896.2	-73.287	30643.098	3.083	2536.56
A	$y=(a+bx)/(1+cx+dx^2)$	101921.62	-20.880	-5772.622	0.560	4881.09
B	$y=(a+bx)/(1+cx+dx^2)$	1357861.8	-257.846	-29288.481	1.174	5266.16

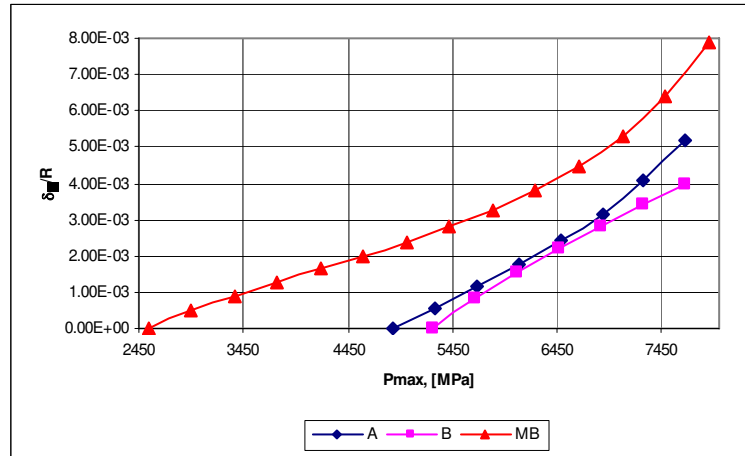
Thus the graphical representation of the relative plastic deformation variation  $\delta_p/R$  according to the hertzian pressure  $P_{\max}$  in Figure 11 shows the maximum bearing capacity of the laser clad layers.

Analyzing Figure 11 it appears that plastic deformation is initiated at 4881.09MPa maximum pressure for the sample code A, to 5266.16MPa for sample code B (which features higher hardness) and to 2536.56MPa for base material (MB).



Thus the bearing capacity is increased by over 100% in laser cladding. The efficiency of the laser cladding in increasing the bearing capacity and the

extension of elasticity range of steel 1C45 becomes obvious.



**Fig. 11.** Variation of the relative plastic deformation acc.to Hertz pressure for the samples code A, B, MB

#### 4. Conclusions

By multi-layer deposition with beam laser in continuous wave it can be achieved thick compact layers of nickel alloy resistant to wear and corrosion, from the Ni-Cr-B-Fe-Al system with good adherence to the substrate by a low dilution layer.

The research on the behavior of laser deposited layers with the nickel alloy base in different corrosive environments revealed that the layer is corrosion resistant in environment 1N NaOH, and 3% NaCl, while in H<sub>2</sub>SO<sub>4</sub> 1N environmental it features the lowest resistance and the highest corrosion rate. The corrosion caused by Cl<sup>-</sup> ions is weaker than that caused by SO<sub>4</sub><sup>2-</sup> ions and the rate of corrosion is lower.

It was noted that the presence of porosity and inclusions affect corrosion behavior. Thus adjusting the deposit parameters to reduce or eliminate electrochemical non uniformities or pores may increase the layer corrosion resistance.

Experimental research on sliding indentation test revealed the following conclusions:

- ❖ laser cladding is an efficient way to move the elasto-plastic transition at higher contact pressures;

- ❖ with increased layer hardness and normal force, the friction coefficient decreases, and the material can be used at higher pressures;

- ❖ with increase layer hardness the trace depth is reduced; plastic deformation is initiated at the maximum pressure of 4881.09 MPa with sample code A, to 5266.16 MPa for the sample code B (which has higher hardness) and to 2536.56 MPa for the base

material (MB). Thus the bearing capacity is increased by 92.42% at the sample code A and to 107.61% for sample code B, as compared with the sample code MB.

#### References

- [1]. **M.F. Schneider** - *Laser cladding with powder*, Ph. D. Thesis University of Twente, Enschede, Olanda, (1998), <http://doc.utwente.nl/fid/1558>
- [2]. **H. Gedda** - *Laser surface cladding - a literature survey*, Lulea University of Technology, Division of Materials Processing, iulie (2000), Suedia, <http://epubl.luth.se/1402-1544/2004/41/>
- [3]. **Zhao Wei-Min, Yong Wang, Tao Han, Wu Kai-Yuan, Jin Xue** - *Electrochemical evaluation of corrosion resistance of NiCrBSi coatings deposited by HVOF*, Surface & coatings technology, vol. 183, n<sup>o</sup>1, (2004), pp. 118-125.
- [4]. **Zhao Wei-Min, Yong Wang, Dong Li-Xian, Wu Kai-Yuan, Jin Xue** - *Corrosion mechanism of NiCrBSi coatings deposited by HVOF*, Surface & coatings technology, vol. 190, n<sup>o</sup> 2-3, pp. 293-298.
- [5]. **TsingHua** - *Electrochemical Corrosion Failure of NiCrBSi Welded Surfacing Coating*, Materials Protection, 30 april, (2005).
- [6]. **S. Levcovici, D.T. Levcovici, C. Gheorghies, S. Boiciuc** - *Laser Cladding of Ni-Cr-B-Fe-Al Alloy on a Steel Support*, The International Thermal Spray Conference and Exposition (ITSC), 15 - 17 mai, Seattle, USA (ISBN 0-87170-836-1).
- [7]. **Krageliskii I.V.** - *Trenie i iznos*, MAŞGIZ, Moskova, (1962).
- [8]. **Popinceanu N, Gafiţanu C, Diaconescu E, Creţu S, Mocanu D.R.** - *Fundamental problems of rolling contact*, Ed. Tehnică, Bucureşti, (1985).
- [9]. **Levcovici S. M.** - *Contributions to the laser surface treatment of tool steel*, Doctoral thesis, Galaţi. (1997).
- [10]. **Z. Liu, J. Sun, W. Shen** - *Study of plowing and friction at the surfaces of plastic deformed metals*, Tribology International 35 (2002) 511-522.
- [11]. **Crudu I** - *Contributions to the study of the influence of normal stress on static destruction by pitting of the point contacts*, Doctoral thesis, Iaşi, (1969).



## ELECTROCHEMICAL BEHAVIOR OF ZINC LAYERS PASSIVATED IN PHOSPHATE SOLUTIONS

**Tamara RADU, Anișoara CIOCAN**

Faculty of Metallurgy, Materials Science and Environment  
"Dunarea de Jos" University of Galati  
email: tradu@ugal.ro

### ABSTRACT

*Phosphate conversion coatings are used on the galvanized steel. By forming a thin protective film on the surface of the steels this treatment enhances corrosion resistance. This paper presents studies on phosphate passivation solutions. The results of treatments for different treatment times and more compositions were analyzed in terms of layer thickness, structural aspects, adherence, and continuity of films. Corrosion resistance was assessed by the linear voltammetry test. Active-passive curves were analysed and compared with unpassivated galvanised samples. For each passivation solution experimented Tafel curves were drawn and corrosion rates were determined. The optimal passivation conditions were settled as function on obtained results.*

**KEYWORDS:** galvanized steel, phosphate conversion coatings, corrosion behaviour

### 1. Introduction

The phosphate-based conversion is a method used to protect the metal against corrosive environments. This is one of the chemical conversion methods and involves a surface modification that increases the passivation tendency of zinc coated steel. By forming a physical barrier on the surface of galvanizing steels the appearance of the "storage stain" or "white rust" is inhibited.

These are more attractive alternatives to chromate conversion treatments that involve the use of chromic acid containing Cr<sup>6+</sup> species. The chromate conversion coating based on Cr<sup>6+</sup> presents environmental and health risks and was banned by the EC today. There are numerous restrictions of hexavalent chromium bearing chromate conversion coatings as top-coat of zinc coated steel [1, 2]. As a result, environmentally friendly chromate free passivation treatments were developed. As potential alternatives to hexavalent chromium, molybdates, tungstates, permanganates, vanadates, rare earth elements (especially cerium) and organic compounds were studied [3-7].

The phosphating is a common chemical conversion treatment that is applied to enhance corrosion resistance [8-10]. It is preferred because it is economical, demonstrates speed of operation and ability to afford excellent corrosion resistance, wear

resistance, adhesion and lubricative properties. For the first reliable record of phosphate coatings applied to prevent rusting of iron and steel (a British patent of 1869 [11]), numerous developments have taken place. Certain factors influenced the processes and, as a consequence, the formation of a stable and uniform coating for corrosion protection remains a challenge. To improve the quality of conversion coatings the works have been concentrated on the study of process parameters and their optimization. [12]. The structure and composition of the phosphate deposition is influenced by numerous factors. Working temperatures, the degree of agitation of the bath and the concentrations of the constituents in the phosphating bath are the most important parameters that affecting the process. On point of economical view to achieve the coating formation in a practicable time a wide variety of acceleration methods (chemical, mechanical, electrochemical) for the immersion processes must be applied as an alternative to Cr(VI) post treatment. The addition of specific compounds to the phosphating baths has also its own influence on phosphating. A wide variety of phosphating compositions are available and new types of phosphate coatings were developed in respect to the regulations imposed by the environmental pollution control. For example, the molybdate-phosphate system was introduced by Tang et al. for corrosion protection of galvanized steel [13,

14]. In this paper a passivation treatment based on phosphate stabilization was analysed. The quality of the phosphating deposition was analysed by some characteristics. Coating thickness and coating porosity were observed. The stability of the phosphate coating as an important property was characterized in terms of the electrochemical behaviour of the zinc layer in phosphate passivation solutions.

## 2. Experimental results and discussion

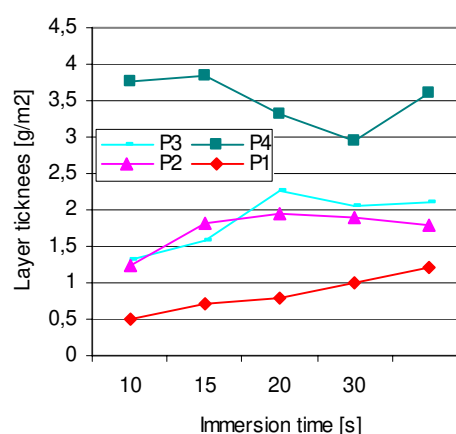
The hot dip galvanized steel sheet has been passivated by total immersion of samples into zinc phosphating solution.

Its chemical composition is given in Table 1. The phosphating was carried out at variable times: 10, 15, 20, 30 and 60 seconds respectively.

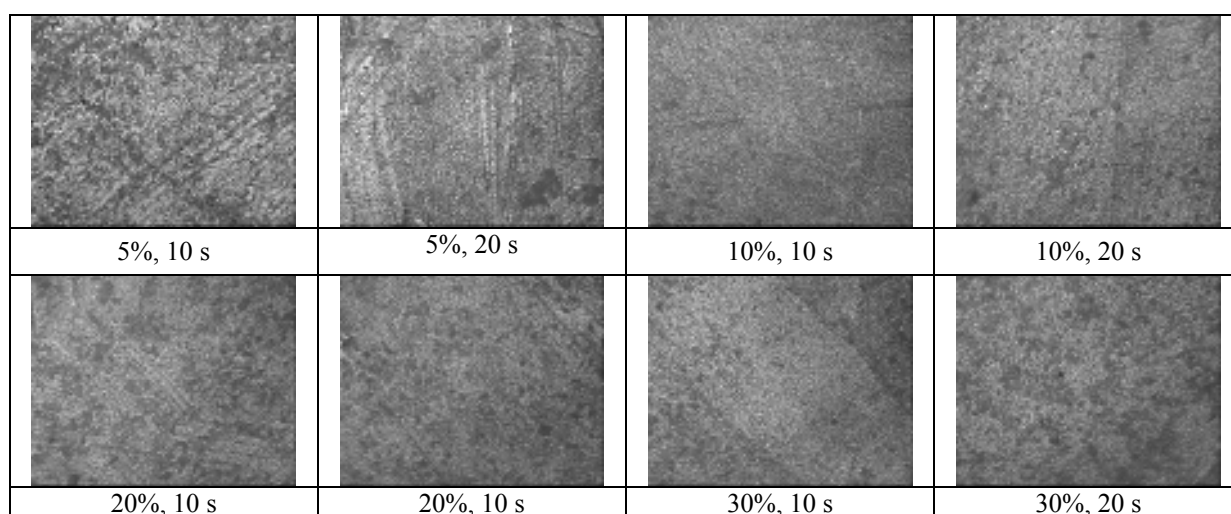
**Table 1.** Chemical composition of the pasivation coating

Code	Zinc dihydrogen phosphate	Fluotitanic acid	Molybdate diamonium
	[g/L]		
P1	1.0	0.25	0.25
P2	2.0	0.5	0.5
P3	4.0	1.0	1.0
P4	6.0	1.5	1.5

For fastening of the conversion coating the samples were heated at 120°C. The thickness of the deposition has been quantified in terms of weight per unit area (as g/m<sup>2</sup>). This has been determined by weighing of the samples before and after immersion into solution and drying of the passivating layer. The thickness of the layer depends on the chemical composition of the solution and the immersion time as show the results in Figure 1. The thickest layers are obtained for samples treated in the passivating solution code P4 and the thinnest for those immersed in the solution code P1. The thickness of the zinc passivating layers varies between 1 and 3g/m<sup>2</sup>. From this point of view the zinc passivating solutions P<sub>2</sub> and P<sub>3</sub> are optimal. The phosphating coatings were examined by optical microscopy (Figure 2). For the sample immersed in solution code P<sub>2</sub> and 10 seconds for treatment time, uniform layers were obtained.



**Fig. 1.** Thickness of layer depending on the immersion time and composition of the passivating solution



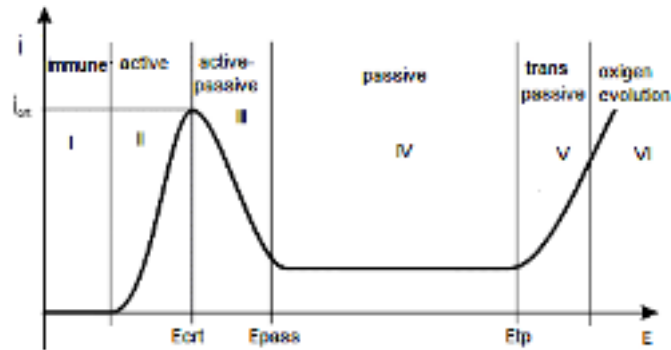
**Fig. 2.** Appearance of the surface of samples depending on passivating conditions (X500)

The corrosion behaviour was carried out with a potentiostat. The linear voltammetry  $i=f(E)$  method was applied from -2000mV toward the anodic direction of 1000mV with a scan rate of 100 mV/min

The corrosion behaviour of the layers has been observed by introducing them in corrosive environments, 3%NaCl solution. A three electrode system with an electrochemical cell volume of

100mL was used to perform the experiments. The auxiliary electrode was a platinum sheet and the reference electrode was calomel. The working electrode was the experimental samples which has an electroactive area of 1cm<sup>2</sup>.

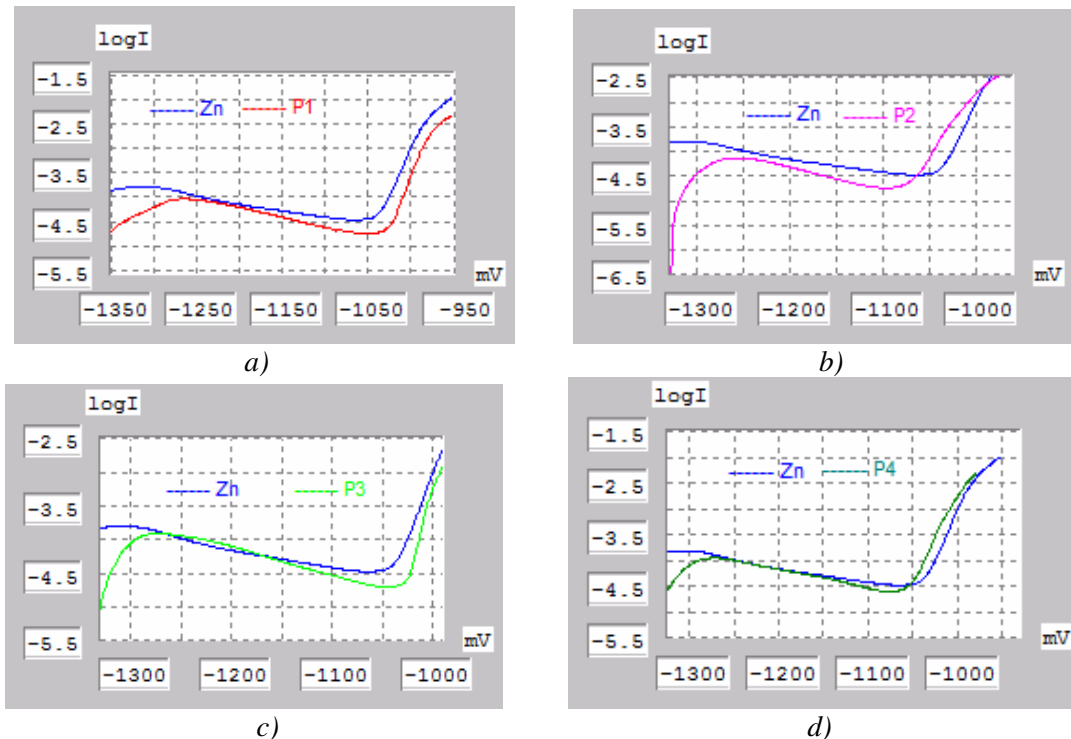
Before the experiments, samples was degreased in acetone and alcohol, rinsed with distilled water and then, dried in air.



**Fig. 3.** Schematic representation of cyclic voltammogram

The electrochemical evaluation of corrosion resistance of phosphate coatings can be done by analysing the curve of polarization of the metal in question. This allows potential electrochemical separation in the areas of: immune, active, active-passive, passive, transpassive and oxygen evolution as shown schematically in Figure 3. The corrosion process takes place in the active zone where the metal

passes into corrosive media as ions by the reaction  $M \rightarrow M^{n+}$ . In this interval the current density is increased up to a critical value ( $i_{crit}$ ) and then start to decline until the passivating potential ( $E_{pass}$ ). The passivation is the result of formation of corrosion products film in accordance with the corrosion reaction  $M \rightarrow M_xO_y$ . In the transpassive region, the oxide film starts to dissolve oxidatively [15].



**Fig. 4.** Anodic polarization curves obtained for zinc phosphate coated steel compared with galvanized sample



Figure 4 presents the anodic polarization curves obtained for zinc phosphate coated samples compared with an untreated hot dip galvanized steel sample. It should be noted that all of the four solutions ensure for material a lower active zone than for zinc. Also this is valid for the critical potential ( $E_{\text{crt.}}$ ), respectively:  $E_{\text{crt.P2}} < E_{\text{crt.P3}} < E_{\text{crt.P1}} < E_{\text{crt.P4}} < E_{\text{crt.Zn}}$ .

Sample 2 (Figure 4b) is the most rapidly passivated ( $E_{\text{pass}} \approx -1100\text{mV}$ ) compared with the galvanized sample ( $E_{\text{pass}} \approx -1050\text{mV}$ ).

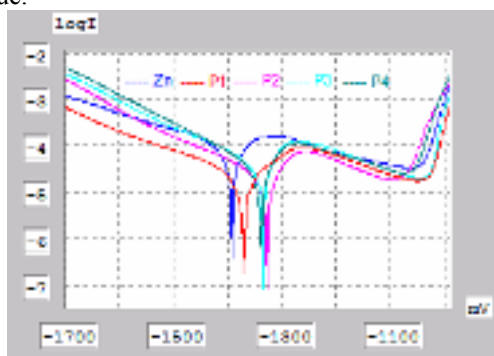
From the experimental data obtained from measurements we chose the Tafel method to study the corrosion behaviour.

The analysis of the graphical representations made it possible to determine the electrochemical parameters of the corrosion process: corrosion potential  $E_{\text{corr}}$ , corrosion current density  $i_{\text{corr}}$ , polarization resistance  $R_p$  and corrosion rate  $V_{\text{corr}}$  (Table 2).

**Table 2.** Electrochemical parameters of the corrosion process

Code	$I_{\text{cor}}$	$E (i=0)$	$R_p$	$V_{\text{cor}}$
	[mA]	[mV]	[ $\text{k}\Omega \cdot \text{cm}^2$ ]	[mm/y]
Zn	31.300	-1392.1	0.30166	0.366
P1	16.2355	-1374.4	1.15	0.190
P2	8.2595	-1328.0	1.01	0.097
P3	12.9615	-1335.0	0.53508	0.152
P4	15.7984	-1344.0	0.64429	0.185

Figure 5 shows the Tafel curves in case for each sample studied. The  $E_{\text{corr}}$  potential was shifted to most negative values. The passivated sample into solution code P<sub>2</sub> has the most negative  $E_{\text{corr}}$  value potential, thus confirming the highest corrosion rate value.



**Fig. 5.** Tafel curves for galvanized sample and respectively for passivated samples

### 3. Conclusion

Surface quality of the passivated galvanized steel is important for the corrosion behavior of the coating. The passivated surfaces show a yellow-green appearance for solutions code P<sub>1</sub>, and green for code P<sub>4</sub>.

Microscopic appearance for high immersion times has shown a continuous and thin layer.

Layer thickness is high for solution code P<sub>4</sub>, minimum for the solution code P<sub>1</sub>, medium for solution code P<sub>2</sub> and P<sub>3</sub>. For each solution the layer thickness increases at the immersion time.

In all solutions tested, result coatings more resistant to corrosion in seawater compared with galvanized steel.

The highest rate of corrosion corresponds to passivating solutions P<sub>2</sub>, P<sub>3</sub> and P<sub>4</sub>; the best being the solution P<sub>2</sub>.

### References

- [1]. Thierry, L., Pommier, N. - *Hexavalent Chromium - Free Passivation Treatments in the Automotive Industry*, Coventya SAS - Lionel Thierry et Nicolas Pommier – April, (2003).
- [2]. Duprat, J.J. - *CrVI Free Conversion Coatings on Zinc and Zinc Alloy Coatings*, CONVENTYA SAS, November, (2007).
- [3]. LIU Guangming, YU Fei, YANG Liu, TIAN Jihong, DU Nan - *Cerium-tannic acid passivation treatment on galvanized steel*, RARE METALS, Vol. 28, No. 3, Jun, (2009), p. 284.
- [4]. Bexell U. and Grehk T.M. - *A corrosion study of hot-dip galvanized steel sheet pre-treated with  $\gamma$ -mercaptopropyl-trimethoxysilane*, Surf. Coat. Technol., (2007), 201 4734
- [5]. Deflorian F., Rossi S., Fedrizzi L., and Bonora P.L. - *EIS study of organic coating on zinc surface pretreated with environmentally friendly products*, Prog. Org. Coat., (2005), 52: 271
- [6]. Swaminatha P. Kumaraguru, Basker Veeraraghavan, and Branko N. Popov - *Development of an Electroless Method to Deposit Corrosion-Resistant Silicate Layers on Metallic Substrates*, Journal of The Electrochemical Society, 153\_7\_B253-B259\_2006
- [7]. Danqing Zhu, Wim J. van Ooij - *Enhanced corrosion resistance of AA 2024-T3 and hot-dip galvanized steel using a mixture of bis-[triethoxysilylpropyl]tetrasulfide and bis-[trimethoxysilylpropyl]amine*, Electrochimica Acta 49 (2004) 1113–1125.
- [8]. Lorin G. - *Phosphating of metals: constitution, physical chemistry and technical applications of phosphating solutions* [M]. Hampton Hill: Finishing Publications, (1974), 146–155.
- [9]. Freeman D B. - *Phosphating and metal pre-treatment* [M]. New York: Industrial Press, (1986), 134–139.



[10]. **Rausch W.** - *The phosphating of metals* [M]. Ohio: ASM International, (1990), 112–116.1–3  
[11]. **Ross, W.A.** - British Patent 3,119 (1869).  
[12]. **Sankara Narayanan, T.S.N.** - Surface Pretreatment by Phosphate Conversion Coatings. A Review, *Rev.Adv.Mater.Sci.* 9 (2005) 130-177.

[13]. **Song, Y.K., Mansfeld, F.** - *Development of a Molybdate–Phosphate–Silane–Silicate (MPSS) coating process for electrogalvanized steel*, *Corrosion Science* 48 (2006) 154–164.  
[14]. **Tang, P.T., Nielsen, G.B., Moeller, P.** - *Plat. Surf. Finish.* 81 (1994) 11.  
[15]. \*\*\* - *ASM Metals Handbook vol. 13, Corrosion*, (1992) 67-71.



## NANOCOMPOSITE COATINGS OBTAINED BY ELECTRO-CO-DEPOSITION OF INERT PARTICLES WITH COBALT-A REVIEW

**Florentina Simona ȘORCARU, Lidia BENEĂ\***

Dunarea de Jos University of Galati, Faculty of Metallurgy and Materials Science,  
Competences Centre: Interfaces-Tribocorrosion-Electrochemical Systems (CC-ITES)

email: [Florentina.Sorcaru@ugal.ro](mailto:Florentina.Sorcaru@ugal.ro),

\*Corresponding author: [Lidia.Benea@ugal.ro](mailto:Lidia.Benea@ugal.ro)

### ABSTRACT

*The paper focuses on review investigations of electrodeposition processes of metallic coatings containing dispersed nanosized particles. The nanosized particles, suspended in the electrolyte by agitation and/or use of surfactants, can be electro-co-deposited with the metal. The inclusion of nanosized particles can give (i) increased microhardness and corrosion resistance, (ii) modified growth to form a nanocrystalline metal deposit and (iii) a shift in the reduction potential of a metal ion. Many operating parameters influence the quantity of incorporated particles, including current density, bath agitation (or movement of work piece) and electrolyte composition. High incorporation rates of the dispersed particles have been achieved using (i) a high nanoparticle concentration in the electrolyte solution, (ii) smaller sized nanoparticles; (iii) a low concentration of electroactive species, (iv) ultrasonication during deposition and (v) pulsed current techniques. Compositional gradient coatings are possible having a controlled distribution of particles in the metal deposit and the theoretical models used to describe the phenomenon of particle co-deposition within a metal deposit are critically considered.*

KEYWORDS: metal–matrix composites (MMCs), nano composites, coating, functional composite, nano particles

### 1. Introduction

The number of publications dealing with obtaining functional materials has considerably increased lately. In addition, to the increased number of publications in this area, a comprehensive review of the mechanism and process of electrodeposition of nano composite layers is necessary.

In this case the purpose of this paper is to address the need for reviewing the publications in the literature. Composite layers in cobalt matrix may provide properties comparable or even better (hardness, corrosion resistance and abrasion resistance) than other composite layers especially for high temperature applications. The objective of this paper is to investigate the parameters for obtaining nanocomposite layers in cobalt matrix. There are few reports in the literature on the preparation of composite layers in cobalt matrix by using inert particles incorporation namely carbides - SiC [1, 2, 3]

oxides (Cr<sub>2</sub>O<sub>3</sub>, [4], ZrO<sub>2</sub> [5, 6], CeO<sub>2</sub> [7] lanthanides [7]).


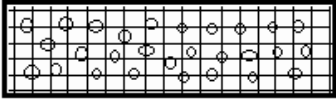

### 2. Electrochemical method

Nanocomposite layers with unique properties may be produced by different methods [8].

The most widely used method of obtaining composite materials is electrochemical co-deposition as it features clear advantages in comparison with other similar methods (chemical deposition by evaporation, electrochemical deposition by evaporation, plasma spraying vacuum spraying) (Table 1) [9].

The electrochemical co-deposition is easier to apply because it requires simple facilities and low cost reactants as compared with the other methods; therefore the basic advantage of this method is efficiency. Table 1 lists a number of nanostructures materials obtainable by electrodeposition [9].

**Table 1.** Various types of nanostructured materials which may be produced by electrodeposition methods [9].

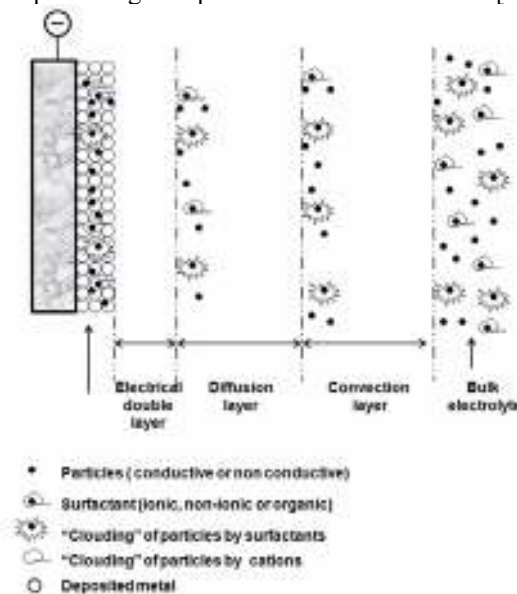
Methods of electrodeposition	Nanoparticles in a metal deposit
Direct current (DC) Pulsed direct current (PDC)	Single metal deposit and nanoparticles 
Pulsed reverse current (PRC) Potentiostatic (P)	Alloy deposit 
Pulsed potentiostatic (PP)	Multilayer deposit 

Nanocomposite structures have long been known for their properties due to extremely fine microstructures [8]. Functional surfaces of improved and extremely complex optical, magnetic, mechanic, chemical and tribological properties are attractive for industrial and biomedical applications [8, 10]. Electrodeposition is a method involving co-electrodeposition of metal, nonmetal or polymer particles into the metal layer under the effect of an electric field. Thus, the co-electrodeposition of various metal matrices such as Ni and Zn, with a large variety of powders from hard carbides like SiC, oxides ZnO, has been intensively studied by Abdel Aal & al. [8]. During this process, particles are suspended in a solution of conventional electrolyte, captured in the metallic matrix producing composite

layers. Moreover, the degree of particles inclusion depends on the nature of used particles (size, shape), and the working conditions (current density, temperature, pH of solution, deposition time, concentration of the particles used in the electrolyte solution) [8].

Functional surfaces are considered nanocomposite layers when one of the sizes of the components is of nanometric order, of typical dimensions below 100 nm. There is a variety of nanometric particles, ranging from 1nm to 100nm, that have successfully been incorporated into metallic matrix by electrodeposition [9].

Particles such as oxides of Al<sub>2</sub>O<sub>3</sub> [12, 13, 14, 15], ZrO<sub>2</sub> [16, 17], TiO<sub>2</sub> [18, 19], CeO<sub>2</sub> [20, 21] or carbides like SiC [1, 2, 3].



**Fig. 1.** Mechanism of particle co-deposition in a metallic matrix adapted acc to (Low 2006) [9]

The inclusion of dispersed particles into a metal matrix has been a scientific novelty and composite layers feature quite interesting properties. The inclusion of the disperse phase into composite layers implies a complex interaction (Fig. 1) of the particles with the hydrodynamic electric field with the metal crystal growth surface and depends on the electrolyte concentration [11]. The metallic matrices most widely used are Ni [23, 24, 28, 29, 30, 31, 56], Cu [15], Zn [10], Co [1, 2, 3]. In spite of all these also attractive are metallic alloys such as Ni-Zn, Ni-Co [25], [26]. Obtaining functional surfaces by electro-co-deposition requires stable suspensions, ceramic particles positively charged. It is extremely important to prevent particles clustering in suspension so as to ensure a controlled deposition and an even distribution of particles in the composite layers. The most investigated composite systems have been Ni-SiC due to their potential technological applications [23-31]. Taking into account the wide variety of metals that can be used; the process of co-electrodeposition makes it possible to produce a wide range of composite layers which, unlike pure metallic layers, feature improved physical, chemical and electro-chemical properties [11, 27, 31]. The use of composite layers starts back in 1950 on automotive engines [4] which progressively develop [11]. In 1970 and 1980, researches have focused on the need to produce layers of improved mechanical properties, to increase steadiness to corrosion and wear. In the 90s' new areas emerged, such as electrocatalysis associated with an increased interest in particle sizes. In his work, Musiani comments upon the new applications reached by the process of electrodeposition [32]. The concentration of the particles incorporated into the electrolyte solution is the essential parameter to successfully obtain composite layers, as they determine to a great extent the properties of the composite layers such as corrosion and wear resistance, corrosion protection to

high temperatures as compared with the corresponding values of the pure metals or alloys [32]. Another essential factor is the even distribution of particles in metallic matrix [33]. It should, however, be underlined that the morphological and structural characteristics of the metallic matrix are strongly affected by the presence of nanoparticles [11]. The future of these materials strongly depends on the capacity of producing them by low cost reliable procedures. The co-electro-deposition method meets part of these requirements since it is an economical and less costly technique than other preparation procedures. These are some of the reasons why this method has become so popular [4, 11, 32]. The processing temperature (room temperature) reduces to a minimum the chemical reactions and the interdiffusion between substrate and composite layers. The layer thickness can be accurately controlled by monitoring the time, the current density and the bath composition (pH) which can be adapted as shown by Bicelli & Co in 2008 [34]. Therefore the structure, morphology and properties of the composite layers are fundamentally affected by the electrodeposition parameters such as electrolysis conditions (composition and the electrolytical bath stirring speed, presence of additives, temperature, pH) [11] and the particle properties (type, size, shape, concentration and dispersion into the electrolytical bath) [9, 27, 32].

### 3. Mechanism of co-electro-deposition of inert particles in a metallic matrix

Much information on the electrodeposition mechanism is obtained from the literature. Co-deposition mechanisms for inert particles co-deposition into the metallic matrix have been developed by means of micrometric – sized particles [9, 27, 35].

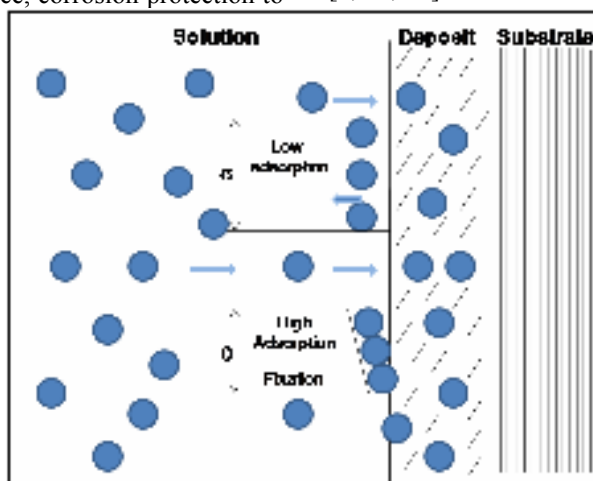
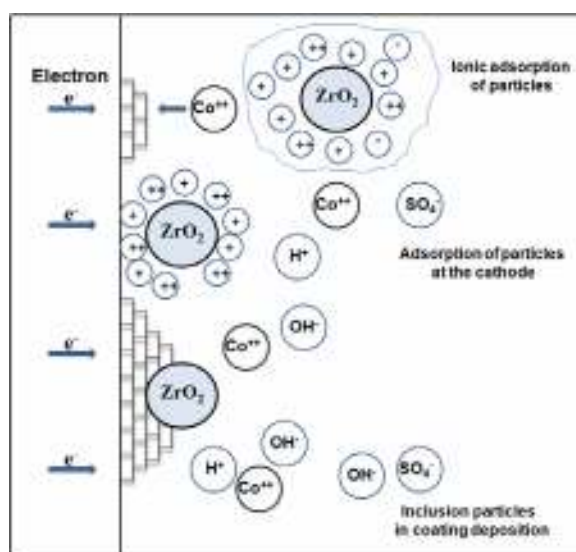


Fig. 2. Electrodeposition process proposed by Guglielmi, adapted after [36]

The first proposed model was reported in 1962 by Whithers followed by the model advanced by Martin & Williams in 1964 [35]. But the first model applied even today is the model of Guglielmi [36] who regards the deposition process as a succession of two phases: a slight electrochemical adsorption phase and a strongly chemical phase. The physical sense of both phases has not been assigned a clear mathematical expression yet and the model fails to consider the issues related to the electrolyte stirring (Fig. 2), a model verified for particles of SiC and

TiO<sub>2</sub> in Ni matrix and for alumina particles in Cu matrix.

The model proposed by Celis & co (1987) [37] makes use of the concept of probability to describe the amount of particles to be incorporated at a given current density and implies the existence of some stages of incorporation of particles into the metallic matrix: (i) reduction of ions at cathode, (ii) adsorption of particles onto the cathode. This model has been validated by examining the (Al<sub>2</sub>O<sub>3</sub>) particles in Cu matrix [37].



**Fig. 3.** Electrodeposition process proposed by Celis, Buelens *et al.* adapted for the system Co/ZrO<sub>2</sub> after [37]

Out of the experimental results reached accounting to this model, we mention: Ni-AZY [38], Ni-SiC [22, 29, 30, 31], Ni-TiO<sub>2</sub> [19], CeO<sub>2</sub>-SiO<sub>2</sub>/Ni-W-P [40], Ni-Al<sub>2</sub>O<sub>3</sub> [41, 42, 43, 44, 48], Ni-SiO<sub>2</sub> [45, 46], Ni-Co/SiC [38] and Ni-MoS<sub>2</sub>/Al<sub>2</sub>O<sub>3</sub> [47], Cu-CeO<sub>2</sub> [49], Co-ZrO<sub>2</sub>/CeO<sub>2</sub> [50], Ni-CeO<sub>2</sub> [51].

However, the interaction particle-electrode, their relative importance and attraction force is still an issue for further discussions. On these principles focused Vereecken and collaborators [52] who stated that the transport of particles up to the surface of a substrate is controlled by diffusion and the influence of the particle gravity force is represented by the different current densities used to obtain composite layers.

More recently, in 2007, Lee and Talbot [11] proposed a model by which it can be found the amount of nanoparticles incorporated into a kinetic process and the mass transfer in the electro-chemical deposition region which is consistent with the experimental data provided on the system Cu-Al<sub>2</sub>O<sub>3</sub>.

Nowadays, the models used to describe particle inclusion are limited to certain conditions and

empirical studies in laboratory are still very important in this respect. Future models describing the process of particle co-electro-deposition in a metallic or non metallic matrix shall need special attention to be focused on: characteristics and properties of nanoparticles (composition, dimension, density, crystallographic structure), along with the operating parameters during the co-electrodeposition process [11].

The validity of the theoretical models of incorporation underlying the inclusion of particles into a metallic matrix requires special attention because the electrochemical process of co-electrodeposition is not fully understood yet [11, 27, 32].

#### 4. Process parameters

The amount of particles incorporated into the metallic matrix (metal or alloy) is the most important parameter taken into account when such functional surfaces are being obtained. As shown in previous sections, composite properties are determined to a large extent. In order to obtain a composite of





exceptional properties, the effect of the process parameters on the content of the particles should therefore be known. Besides the practical meaning of these effects, also a necessary condition is to understand the mechanism of particle co-deposition.

In the long run it has been found that there are many, direct or indirect process parameters which

affect the content of particles in the composite layers [9, 37, 53, 54].

A large variety of particles (micro and nanometric dimensions) has successfully been incorporated by co-electro-deposition. Table 2 shows a number of types of particles included into a metallic matrix by co-electro-deposition.

**Table 2.** Inclusion of other types of particles into metal deposits by electrodeposition

Nanoparticles	Metallic matrix	Substrate	Ref.
SiC	Ni	steel	[55, 56, 57]
SiC	Ni-Co	Cu	[22, 58]
CeO <sub>2</sub>	Cu	steel	[21]
Al <sub>2</sub> O <sub>3</sub>	Ni, Co	steel	[59, 60]
CeO <sub>2</sub> , L <sub>2</sub> O <sub>3</sub>	Co	steel	[7, 61]
ZrO <sub>2</sub>	Cu	steel	[62]
TiO <sub>2</sub>	Zn	steel	[63]
CeO <sub>2</sub>	Ni	steel	[64]
Al <sub>2</sub> O <sub>3</sub>	Ni	steel	[41, 66]
SiC	Co	steel	[3]
ZrO <sub>2</sub>	Co	steel	[67]

The inclusion of nanometric particles into metal layers depends on process parameters including the particle characteristics, concentration [11, 68, 69], type, shape dimension, electrolyte composition (concentration of electrolytes, additives, temperature, pH) [11], current density [9, 11, 27, 32] and electrodes geometry (disc, plate or other variants), stirring speed [11].

Composition of the electrolyte is known as an important factor which influences the process of co-electro-deposition [7, 9, 11]. However, an accurate image of the effect of the experimental parameters is often hard to get. In most recent papers reported it is suggested the existence of three global factors to be identified as affecting the co-deposition, namely (1) density of the applied current, (2) type and concentration of particles and (3) electrolyte stirring speed [9, 11, 27, 32].

## 5. Current density

There is a variety of techniques to be used, such as direct current, pulse current and reverse pulse current. In electrodeposition, the method most widely used to obtain nanocomposites, the most important parameter is the current density. This technique is based on the concept that inclusion of nanoparticles occurs simultaneously with the reduction reaction on the metal layer surface. Hong-Kee Lee [70] researches the effect of SiC particles of micro and nanometric sizes in a Ni matrix.

Taking into account the effects of the deposition parameters, pH of the deposition bath, the current

density and the stirring speed, the particle concentration, some authors notice two different effects of the current density:

- 1) a small or zero influence of the current density on the number of particles incorporated;
- 2) others say that a significant effect takes place along with the presence of one or more particles stirring speed depending on the current density resorted to (Ni-SiC) [71].

It has been found that the degree of inclusion of the disperse phase decreases with increased current density for the systems Cu-ZrO<sub>2</sub> [62], Ni-Al<sub>2</sub>O<sub>3</sub> [41, 66], and also that an increased current density leads to a higher inclusion of the dispersed phase in the metallic matrix [1] for the systems Ni-TiO<sub>2</sub> [7], Co-SiC [72]. The current density also was found to affect the amount of alumina nanoparticles in the Ni matrix electrodeposited [73].

## 6. Electrolyte stirring

Particles to be included into a metallic matrix should be carried away from the solution to further reach the cathode surface [1, 9, 27, 32] According to the literature [74] it becomes obvious that the electrolyte stirring speed enables particle transport and an increased stirring speed results in a larger amount of particles being incorporated [9, 11]. In spite of this, Hovestad & Co (1995) [27] reported that a too high electrolyte stirring speed decreases the particle co-deposition, because a too high speed makes the particles collide and thus remove the particles from the cathode surface before inclusion.

Therefore, all researchers have made use of a certain type of electrolyte bath stirring and sometimes [9, 11, 27, 32, 75] have mixed the electrolyte particles before experiments so as to reach a stable suspension. The electrolyte mixture help the clustered particles separate and homogenous deposits be obtained, containing finely dispersed and well distributed particles [11].

The effects of such a parameter on co-electrodeposition should be accounted for by the fact that particles affect suspension stability. Beside particles conveyance, stirring is also used to keep particles in the suspension.

Suspension stability increases with reduced degree of inclusion of particles ( $\theta$ ), which in the case of spherical particles is given by Stokes law [27].

$$\vartheta = 2gr_p^2(\rho_p - \rho_e)/9\eta \quad (1)$$

with:  $v$  - rate of incorporation of the particles,  $g$  - acceleration due to gravity ( $g = 9,81 \text{ m/s}^2$ ),  $r_p$  - particle radius (m),  $\rho_p$  - particle density ( $\text{kg/m}^3$ ),  $\rho_e$  - density of the solution ( $\text{kg/m}^3$ ),  $\eta$  - viscosity (expressed in  $\text{kg/m s}$ ).

Suspension stability directly depends on the particles size and density which is different for each particular type of particles. Moreover, density and viscosity of the electrolyte are determined by the elements of the bath and temperature [11, 27].

The basic purpose of the electrolyte stirring speed is to keep the particles in suspension and prevent their settlement or floating in the electrolytic solution. Stirring may be reached through air bubbling, by electrolyte recirculation or by means of a laboratory magnetic stirrer [9, 11, 27].

## 7. Bath composition

Although these parameters are less investigated than particle properties, current density or stirring speed, the electrolyte composition is also an important parameter in the co-electrodeposition process [9, 11, 27, 32]. From the researches it is found that the composite layers the easiest to obtain are those in matrix of Ni, Fe, Zn, the more difficult to obtain are those based on Ag, while the most difficult are those related to chrome (due to the higher hydrogen current output and the presence of a cathodic film on these metals) [4]. A certain electrolyte composition and certain electrolysis conditions facilitate inclusion of the dispersed phase into the matrix or its removing (ex: Cu-Al<sub>2</sub>O<sub>3</sub>: easier to obtain from base electrolytes) [4].

## 8. pH of plating baths

Investigations [27, 32, 74, and 75] on the effect of the bath pH provide comparable results. Particle inclusion drastically decreases in acid electrolyte

solutions (pH from 2 to 3) and stays almost constant or slightly decreases over this level [11, 27].

- *electrolyte pH* plays an essential role in making composite coatings especially in case of particles interaction with the matrix being formed due to the variation of the dispersed phase as a result of the excess ions of OH<sup>-</sup> or H<sub>3</sub>O<sup>+</sup>, and interaction of the hydrogen which gets separated [11, 27, 74, 75].

## 9. Additives

In order to incorporate particles into the metallic matrix, an important role is played by additives [11, 27, 76, 77]. By adding small amounts of monovalent cations such as tetra-etilen pentamina (TEPA), alanina, etilendiamino tetraacetic acid (EDTA), gelatin, dodecil sodium sulphate [64] favourise particle co-deposition. Inclusion of nanoparticles of TiO<sub>2</sub> in a Zn matrix [75] is improved by adding cetyltrimethyl-ammonium bromide which is an anionic tension active agent.

Kanagalasara Vathsala [27] adds a surfactant (SDS) in the electrodeposition bath to stabilize the suspension of ZrO<sub>2</sub> particles. Tension activators improve the suspension stability by increasing the moistening of the particles in suspension thus providing a better adhesion to the cathode surface [27]. The moistening capacity of the particles is not a major problem in co-deposition but there are additional advantages when using cationic tension activators [27, 76]. These cationic tension activators provide a positive degree of inclusion of the particles, prevents clustering and electrostatic attraction at the cathode. Similarly, by using a tension activator agent, H. Gül & Co [65] have made Ni coatigns containing about five times more particles of alumina (Al<sub>2</sub>O<sub>3</sub>), as compared with other experiments. The disadvantage of using tension activators is that these are incorporated in the deposit [65].

## 10. Conclusions

Co-electrodeposition of inert particles in a metallic matrix is a suitable technique of making functional layers. Especially in this field it provides a good alternative to other techniques and makes it possible to produce functional surfaces of unique properties. Many independent parameters influence the process of co-deposition.

An accurate classification of the effect for each parameter is hard to obtain as these are often different and in some cases even contradictory. Particle concentration, current density and stirring speed seem to be the most meaningful parameters. Most researchers suggest that the mechanism of growing the codeposited layers plays an important role and this calls for further investigations.





The mechanism of co-electrodeposition implies transportation of particles to the cathode surface by means of the stirring speed and inclusion into the metal takes place by reducing the ions adsorbed. The attempts to develop models capable of predicting the mass of particles inclusion under experimental conditions have failed so far. Nowadays, models involving detailed descriptions of particles transportation and particles interactions with the cathode provide a promising perspective of obtaining functional surfaces.

A number of co-electro-deposition techniques (DC, PVD, etc) have been used to include particles of nanometric dimensions in metallic matrix. Such techniques made it possible to obtain functional surfaces featuring a wide range of properties which are clearly better than those of pure metals or alloys.

In some cases (DC), it has been shown that this method is inferior to PVD for making nanocomposites. Benefits of these procedures include surface nanostructures, increased degree of inclusion into the metallic matrix and selectively, the particles size.

Inclusion of nanometric particles may provide a growth of the metallic crystals forming a deposit of nanocrystalline metal. Inclusion of nanometric particles may increase microhardness and corrosion resistance.

The different theoretical methods that describe the dispersed phase behavior in a metallic matrix require special attention; the experimental studies are carried out on current densities, mass transport, and degree of inclusion of nanoparticles.

Co-electro-deposition of particles is significantly better by decreasing the pH and adding additives into the electrolytes. Inclusion of particles in a metal matrix results in functional surfaces with physical, chemical or mechanical properties depending on thickness.

Now the process of co-electro-deposition of the nanoparticles is still in progress but has already shown certain advantages for various applications. This technology of functional surfaces has a great potential for further developments in industry and biomedicine.

### Acknowledgement

The authors gratefully acknowledge project C2-02/01-03-2012 (CEA-IFA) for funding.

### References

- [1]. B. J. Hwang, C. S. Hwang - *Mechanism of codeposition of silicon carbide with electrolytic cobalt*, Journal of the Electrochem. Soc. 140(4) (1993) 979-984.
- [2]. E. Rudnik - *Influence of surface properties of ceramic particles on their incorporation into cobalt electroless deposits*, Appl. Surf. Sci. 255 (2008) 2613-2618
- [3]. E. Rudnik, L. Burzynska, W. Jakubowska - *Codeposition of SiC particles with cobalt matrix*, J. Achievements in Materials and Manufacturing Engineering 41 (2010) 195-199.
- [4]. K. Kumar, R. Chandramohan, D. Kalyanaraman - *Effect of heat treatment on cobalt and nickel electroplated surfaces with Cr<sub>2</sub>O<sub>3</sub> dispersions*, Appl. Surf. Sci. 227 (2004) 383-386.
- [5]. E. P. Rajiv, A. Iyer, S. K. Seshadri - *Tribological properties of cobalt-partially stabilized zirconia (PSZ) composites in dry sliding conditions*, Wear 189 (1995) 100-106.
- [6]. L. Benea, P. Ponthiaux, F. Wenger - *Co-ZrO<sub>2</sub> electrodeposited composite coatings exhibiting improved micro hardness and corrosion behaviour in simulating body fluid solution*, Surface Coatings Technology, 205 (2011) 5379-5386.
- [7]. G. Cârâc, G. A. Bund, D. Thiemig - *Electrocodeposition and characterization of cobalt lanthanide oxides composite coatings*, Surf. Coat. Technol. 202(2) (2007) 403-411.
- [8]. A. Abdel Aal, H. B. Hassan - *Electrodeposited nanocomposite coatings for fuel cell application*, J. Alloys Compounds xxx (2008) xxx-xxx.
- [9]. C. T. J. Low, R. G. A. Wills, F. C. Walsh - *Electrodeposition of composite coatings containing nanoparticles in a metal deposit* Surface Coatings Technology 201 (2006) 371-383, <http://dx.doi.org/10.1016/j.surfcoat.2005.11.123>
- [10]. W. Wang, F. Y. Hou, H. T. Guo, *Fabrication and characterization of Ni-ZrO<sub>2</sub> composite nano-coatings by pulse electrodeposition*, Scripta Materialia 53 (2005) 613-618.
- [11]. A. Gomes, I. Pereira, B. Fernández, R. Pereiro - *Electrodeposition of Metal Matrix Nanocomposites: Improvement of the Chemical Characterization Techniques*, Adv. Nanocomposites - Synthesis, Characterization and Industrial Applications, 503-526.
- [12]. Y. Liu, L. Ren, S. Yu, Z. Han - *Influence of current density on nano-Al<sub>2</sub>O<sub>3</sub>/Ni+Co bionic gradient composite coatings by electrodeposition*, Journal of University of Science and Technology Beijing, 15 (5) (2008) 633.
- [13]. B. R. Tian, Y. F. Cheng - *Electrolytic deposition of Ni-Co-Al<sub>2</sub>O<sub>3</sub> composite coating on pipe steel for corrosion/erosion resistance in oil sand slurry*, Electrochimica Acta 53 (2007) 511-517, <http://dx.doi.org/10.1016/j.electacta.2007.07.013>.
- [14]. A. Bund, D. Thiemig, *Influence of bath composition and pH on the electrocodeposition of alumina nanoparticles and nickel*, Surface Coatings Technology 201 (2007) 7092-7099, <http://dx.doi.org/10.1016/j.surfcoat.2007.01.010>.
- [15]. D. Thiemig, A. Bund - *Influence of ethanol on the electrocodeposition of Ni/Al<sub>2</sub>O<sub>3</sub> nanocomposite films*, Applied Surface Science 255 (2009) 4164-4170, <http://dx.doi.org/10.1016/j.apsusc.2008.10.114>
- [16]. K. Vathsala, T.V. Venkatesha, *Zn-ZrO<sub>2</sub> nanocomposite coatings: Electrodeposition and evaluation of corrosion resistance*, Applied Surface Science, In Press, Corrected Proof, (2011), doi:10.1016/j.apsusc.2011.05.067.
- [17]. R. Arghavani, N. P. Ahmadi - *The effect of co-electrodeposited ZrO<sub>2</sub> particles on the microstructure and corrosion resistance of Ni coatings*, J Solid State Electrochem 15 (2011) 2199-2204, DOI 10.1007/s10008-010-1229-z.
- [18]. B. M. Praveen, T. V. Venkatesha - *Electrodeposition and properties of Zn-nanosized TiO<sub>2</sub> composite coatings*, Applied Surface Science xxx (2007) xxx-xxx.
- [19]. M. S. Ali Eltoun, A. M. Baraka, M. Saber, Elfatih A. Hassan - *Electrodeposition and Characterization of Nickel-Titania Nanocomposite Coatings from Gluconate Baths*, International Journal Of Multidisciplinary Sciences And Engineering, 2 (4) (2011), [ISSN: 2045-7057], [www.ijmse.org](http://www.ijmse.org).
- [20]. M. Srivastava, V. K. William Grips, K. S. Rajam - *Electrodeposition of Ni-Co composites containing nano-CeO<sub>2</sub> and their structure, properties*, Appl. Surf. Sci. 257 (2010) 717-722.
- [21]. V. Mangam, K. Das, S. Das - *Structure and properties of electrocodeposited Cu-CeO<sub>2</sub> nanocomposite thin films*, Materials Chemistry and Physics 120 (2010) 631-635
- [22]. B. Bahadormanesh, A. Dolati - *The Kinetics of Ni-Co/SiC Composite Coatings Electrodeposition*, J. Alloys Compd., 504 (2010) 514-518.



- [23]. S. C. Wang, W. C. J. We - *Kinetics of electroplating process of nano-sized ceramic particle/Ni composite* Materials Chemistry and Physics 78 (2003) 574–580
- [24]. B. R. Tian, Y. F. Cheng - *Electrolytic deposition of Ni–Co–Al<sub>2</sub>O<sub>3</sub> composite coating on pipe steel for corrosion/erosion resistance in oil sand slurry*, Electrochimica Acta 53 (2007) 511–517, <http://dx.doi.org/10.1016/j.electacta.2007.07.013>.
- [25]. N. Fenineche, C. Coddet, A. Saida - *Effect of electrodeposition parameters on the microstructure and mechanical properties of Co-Ni alloys*, Surface and Coatings Technology, 41 (1990) 75 - 81.
- [26]. A. Abdel Aal - *Hard and corrosion resistant nanocomposite coating for Al alloy*, Materials Science and Engineering A 474 (2008) 181–187, <http://dx.doi.org/10.1016/j.msea.2007.04.058>.
- [27]. A. Hovestad, L.J.J. Janssen - *Electrochemical codeposition of inert particles in a metallic matrix*, J. Appl. Electrochem., 25 (1995) 519–527.
- [28]. L. Benea, P. L. Bonora, A. Borello, S. Martell - *Wear corrosion properties of nano-structured SiC–nickel composite coatings obtained by electroplating*, Wear 249 (2002) 995–1003.
- [29]. L. Benea, V. Iordache, F. Wenger, P. Ponthiaux - *Nanostructured SiC-Ni composite coatings obtained by electrodeposition a tribocorrosion study*, The Annals of "Dunarea De Jos" University of Galati, Fascicle IX Metallurgy and Materials Science, 1 (2005) 1453–1457.
- [30]. A. F. Zimmerman, G. Palumbo, K. T. Aust, U. Erb - *Mechanical properties of nickel silicon carbide nanocomposites*, Materials Science and Engineering A 328 (2002) 137–146.
- [31]. Y. Zhou, H. Zhang, B. Qian - *Friction and wear properties of the co-deposited Ni–SiC nanocomposite coating*, Applied Surface Science 253 (2007) 8335–8339, <http://dx.doi.org/10.1016/j.apsusc.2007.04.047>.
- [32]. M. Musiani - *Electrodeposition of composites: an expanding subject in electrochemical materials science*, Electrochimica Acta 45 (2000) 3397–3402.
- [33]. E. J. Podlaha, Y. Li, J. Zhang, Q. Huang, A. Panda, A. Lozano-Morales, D. Davis, Z. Guo - *Electrochemical Deposition of Nanostructured Metals*, Copyright 2006 by Taylor & Francis Group, LLC.
- [34]. L. P. Bicelli, B. Bozzini, C. Mele, L. D'Urzo - *A Review of Nanostructural Aspects of Metal Electrodeposition*, Int. J. Electrochem. Sci., 3 (2008) 356 – 408.
- [35]. P. Berçot - *Dépôts composites par électrolyse. Modélisation*, Techniques de l'Ingénieur, traité Matériaux métallique, M 1622, (2003).
- [36]. N. Guglielmi - *Kinetics of the Deposition of Inert Particles from Electrolytic Baths*, Journal of Electrochemical Society, vol. 119 (1972) 1009–1012.
- [37]. J. P. Celis, J. R. Roos, C. Buelens - *A Mathematical Model for the Electrolytic Codeposition of Particles with a Metallic Matrix*, J. Electrochem. Soc., 134 (1987) 1402–1408.
- [38]. M. Srivastava, V. K. W. Grips, A. Jain, K. S. Rajam - *Influence of SiC particle size on the structure and tribological properties of Ni–Co composites*, Surf. Coat. Technol. 202 (2007) 310–318.
- [39]. S. T. Aruna, V. K. W. Grips, K. S. Rajam - *Ni-based electrodeposited composite coating exhibiting improved microhardness, corrosion and wear resistance properties*, J. Alloy. Compd., 468 (2009) 546–552.
- [40]. R. Xu, J. Wang, Z. Guo - *High-Temperature Oxidation Behavior of CeO<sub>2</sub>-SiO<sub>2</sub>/Ni-W-P Composites*, Trans. Nonferrous Met. Soc. China, 19 (2009) 1190–1195.
- [41]. A. C. Ciubotariu, L. Benea, M. Lakatos–Varsany, V. Dragan - *Electrochemical Impedance Spectroscopy and Corrosion Behaviour of Al<sub>2</sub>O<sub>3</sub>-Ni nano Composite Coatings*, Electrochim. Acta, 53 (2008) 4557–4563.
- [42]. B. Szczygiel, M. Kolodziej - *Composite Ni/Al<sub>2</sub>O<sub>3</sub> coatings and their corrosion resistance*, Electrochim. Acta 50 (2005) 4188–4195.
- [43]. Y. Liu, L. Ren, S. Yu, Z. Han - *Influence of Current Density on nano-Al<sub>2</sub>O<sub>3</sub>/Ni+Co Bionic Gradient Composite Coatings by Electrodeposition.* Materials, 15: (2008) 633.
- [44]. Q. Feng, T. Li, H. Teng, X. Zhang, Y. Zhang, C. Liu, J. Jin - *Investigation on the Corrosion and Oxidation Resistance of Ni–Al<sub>2</sub>O<sub>3</sub> Nano-Composite Coatings Prepared By Sediment Co-Deposition*, Surf. Coat. Technol., 202 (2008) 4137–4144
- [45]. X. Bin-shi, W. Hai-dou, D. Shi-yun, J. Bin, T. Wei-yi, *Electrodepositing Nickel Silica Nano-Composites Coatings*, Electrochem. Commun, 7 (2005) 572–575 (2005)
- [46]. W.Y. Tu, B.S. Xu, S.Y. Dong, H. Wang - *Electrocatalytic Action of Nano-SiO<sub>2</sub> with Electrodeposited Nickel Matrix*, Mater. Lett, 60 (2006) 1247–1250.
- [47]. Z. Huang, D. Xiong - *MoS<sub>2</sub> Coated with Al<sub>2</sub>O<sub>3</sub> for Ni–MoS<sub>2</sub>/Al<sub>2</sub>O<sub>3</sub> Composite Coatings by Pulse Electrodeposition*, Surf. Coat. Technol., (2007).
- [48]. G. Cârâc, C. Iticescu, L. Benea, T. Lampke, S. Steinhäuser - *The effect of nano-Al<sub>2</sub>O<sub>3</sub> dispersed phase in nickel matrix electrocodeposited*, Revue Roumaine de Chimie, 52(11), 2007, 1057–1062.
- [49]. V. Mangam, K. Das, S. Das - *Structure and Properties of Electrocodeposited Cu–CeO<sub>2</sub> Nanocomposite thin Films*, Mater. Chem. Phys., 120 (2010) 631–635.
- [50]. A. Machocki, A. Denis, W. Grzegorzczak, W. Gac - *Nano- and Micro-Powder of Zirconia and Ceria-Supported Cobalt Catalysts For the Steam Reforming of Bio-ethanol*, Appl. Surf. Sci., 256 (2010) 5551–5558.
- [51]. N. S. QU, D. Zhu, K. C. Chan - *Fabrication of Ni–CeO<sub>2</sub> Nanocomposite by Electrodeposition*, Scr Mater., 54 (2006) 1421–1425.
- [52]. P. M. Vereecken, I. Shao, P.C. Searson - *Particle Codeposition in Nanocomposite Films* Journal of the Electrochemical Society, 147(2000) 2572.
- [53]. J. P. Celis, J. R. Roos - *Kinetics of the Deposition of Alumina Particles from Copper Sulfate Plating Baths*, J. Electrochem. Soc., 124 (10) (1977) 1508–1511.
- [54]. C. Buelens, J. P. Celis, J. R. Roos - *Electrochemical aspects of the codeposition of gold and copper with inert particles*, J. Appl. Electrochem., 13 (1983) 541.
- [55]. M. H. Fini, A. Amadeh - *Corrosion Resistance of AZ91 Magnesium Alloy with Pulse Electrodeposited Ni-SiC Nanocomposite Coating*, Journal of Nano- and Electronic Physics, 4 (1), (2012) 01008.
- [56]. L. Benea, P. L. Bonora, A. Borello, S. Martelli, F. Wenger, P. Ponthiaux, J. Galland - *Preparation and investigation of nanostructured SiC–nickel layers by electrodeposition*, Solid State Ionics 151 (2002) 89–95.
- [57]. C. Muller, M. Sarret, M. Benballa, *ZnNi/SiC composites obtained from an alkaline bath*, Surface and Coatings Technology 162 (2002) 49–53.
- [58]. M. Srivastava, V.K. W. Grips, K. S. Rajam - *Electrochemical deposition and tribological behaviour of Ni and Ni–Co metal matrix composites with SiC nano-particles* Applied Surface Science 253, (2007) 3814–3824, <http://dx.doi.org/10.1016/j.apsusc.2006.08.022>.
- [59]. B. R. Tian, Y. F. Cheng, *Electrolytic deposition of Ni–Co–Al<sub>2</sub>O<sub>3</sub> composite coating on pipe steel for corrosion/erosion resistance in oil sand slurry*, Electrochimica Acta 53 (2007) 511–517, <http://dx.doi.org/10.1016/j.electacta.2007.07.013>
- [60]. L. M. Chang, M. Z. An, H.F. Guo, S. Y. Shi - *Microstructure and properties of Ni–Co/nano-Al<sub>2</sub>O<sub>3</sub> composite coatings by pulse reversal current electrodeposition*, Applied Surface Science 253 (2006) 2132–2137, <http://dx.doi.org/10.1016/j.apsusc.2006.04.018>.
- [61]. Y. Matsumoto, H. Ohmura, T. Goto - *Effect of lanthanide ions on the electrodeposition of cobalt and manganese oxides*. Journal of Electroanalytical Chemistry 399 (1995) 91–96
- [62]. L. Benea - *Electrodeposition of Zirconia Particles in a Copper Matrix*, Materials and Manufacturing Processes, Vol. 14, No. 2 (1999) 231–242, <http://dx.doi.org/10.1080/10426919908914820>
- [63]. A. Vlăsa, S. Varvara, A. Pop, C. Bulea, L.M. Muresan - *Electrodeposited Zn–TiO<sub>2</sub> nanocomposite coatings and their corrosion behavior*, J Appl Electrochem, 40 (2010) 1519–1527, DOI 10.1007/s10800-010-0130-x.



- [64]. M. Srivastava, V. K. W. Grips, K. S. Rajam, - *Electrodeposition of Ni-Co composites containing nano-CeO<sub>2</sub> and their structure, properties*, Appl. Surf. Sci. 257 (2010) 717–722.
- [65]. H. Gül, F. Kılıç, S. Aslan, A. Alp, H. Akbulut - *Characteristics of electro-co-deposited Ni-Al<sub>2</sub>O<sub>3</sub> nano-particle reinforced metal matrix composite (MMC) coatings*, Wear 267 (2009) 976–990, <http://dx.doi.org/10.1016/j.wear.2008.12.022>.
- [66]. D. Thiemig, A. Bund - *Influence of ethanol on the electrocodeposition of Ni/Al<sub>2</sub>O<sub>3</sub> nanocomposite films*, Applied Surface Science 255 (2009) 4164–4170, <http://dx.doi.org/10.1016/j.apsusc.2008.10.114>.
- [67]. E. P. Rajiv, A. Iyer, S. K. Seshadri - *Tribological properties of cobalt-partially stabilized zirconia (PSZ) composites in dry sliding conditions*, Wear 189 (1995) 100-106.
- [68]. Kyle Jiang - *Electrochemical Co-deposition of Metal-Nanoparticle Composites for Microsystem Applications*, School of Mechanical Engineering, University of Birmingham, UK, B15 2TT, 391-412.
- [69]. R. C. Alkire, D. M. Kolb - *Advances in Electrochemical Science and Engineering, volume 7*, IWILEY-VCH Verlag GmbH, 69469 Weinheim (Germany), (2002), SBNs: 3-527-29830-4 (Hardcover); 3-527-60026-4 (Electronic), <http://www.wiley-vch.de>
- [70]. H. Lee, Y. Lee, J. M. Jeon - *Codeposition of Micro- and Nano-sized SiC Particles in the Nickel Matrix Composite Coatings Obtained by Electroplating*, Surf. Coat. Technol., 201 (2007) 4711-4717.
- [71]. I. Dobosz, E. Rudnik, L. Burzynska - *Codeposition of SiC particles with electrolytic Nickel* Archives of metallurgy and materials, 56 (2011)
- [72]. X. Bin-shi, W. Hai-dou, D. Shi-yun, J. Bin, T. Wei-yi - *Electrodepositing Nickel Silica Nano-Composites Coatings*, Electrochem. Commun., 7 (2005) 572–575.
- [73]. R.K. Saha, T.I. Khan - *Effect of applied current on the electrodeposited Ni-Al<sub>2</sub>O<sub>3</sub> composite coatings*, Surface & Coatings Technology xxx (2010) xxx–xxx,
- [74]. Q. Zhou, H. Ge, G. Wei, Q. Wu - *Influence of bath composition on the electrodeposition of Cobalt-Molybdenum amorphous alloy thin films*, Materials, 15 (2008) 611.
- [75]. E. Gomez, E. Pellicer, E. Valles - *Influence of the Bath Composition and the pH on the Induced Cobalt/Molybdenum Electrodeposition*, J. Electroanal. Chem. 556 (2003) 137-145.
- [76]. B. M. Praveen, T. V. Venkatesha - *Electrodeposition and properties of Zn-nanosized TiO<sub>2</sub> composite coatings*, Applied Surface Science xxx xxx–xxx (2007).
- [77]. F. Hou, W. Wang, H. Guo - *Effect of the dispersibility of ZrO<sub>2</sub> nanoparticles in Ni-ZrO<sub>2</sub> electroplated nanocomposite coatings on the mechanical properties of nanocomposite coatings*, Applied Surface Science 252 (2006) 3812–3817.



## EVOLUTION OF COPPER MICROSTRUCTURE SUBJECTED TO EQUAL CHANNEL ANGULAR PRESSING

**Carmela GURAU, Gheorghe GURAU**

"Dunarea de Jos" University of Galati

email: [ggurau@ugal.ro](mailto:ggurau@ugal.ro)

### ABSTRACT

*This paper aims to study bulk severe plastic deformation processes capable to produce ultrafine grain and also nanostructured 3D materials, interesting for processing in current industry. Samples of copper alloy were solution treated and then were subjected to repetitive Equal Channel Angular Pressing at room temperature in 1 to 8 passes, using route C. Severely deformed specimens were studied after each deformation pass. Their microstructural evolution and mechanical properties were investigated. Optical microscopy progression is evaluated on each separate ECAP pass. It is well known that although copper is a deficient resource it is used to the same extent as aluminum, a rich resource on the earth's crust. This research signs up in the category of new technologies for obtaining bulk metallic nanostructures that allow more judicious use of copper alloys by the substantial improvement of properties of use.*

KEYWORDS: SPD, ECAP, UFG, in bulk nanomaterials, copper, microstructural evolution

### 1 Introduction

Ultrafine grain materials and much interesting materials with nanoscale dimensions nowadays are a challenge for researchers and also an issue up to date. Special attention is given now to study how to obtain massive nano materials. In bulk nanostructures have all three dimensions at the nanometric scale (3-D). Numerous methods have been developed for the manufacturing of nanomaterials. Severe plastic deformation is remarkable way for metallic massive material. In this approach it can be obtained crystalline grain size varies from less than 100 nm or up to 200 nm until 500 nm for ultra-fine grained in bulk metallic materials [1-3].

Since the 80s when Ruslan Valiev developed equal channel angular extrusion, this type of top-down methods, investigations using this method have exploded. Since then has tried producing massive material with three dimensions at the nanoscale by ECAP. Equal channel angular pressing or extrusion (ECAP or ECAE) have been defined that a process used to applied severe plastic deformations (SPD) to processed materials with the target of improving their mechanical properties by reducing the grain size. ECAP uses a die where there are cut two channels, equal in cross-section, intersecting at an inner angle

denoted in literature with  $\Phi$ , which is generally close to  $90^\circ$ . The sample is pressed around a sharp corner. ECAP introduce large plastic strains in metals and their alloys to reduce grain size, using repetitive pressing. The final ECAP products have nanometric grains or ultrafine grains, but keep the cross section and shape like initial sample. Therefore the ECAE process allows the achievement of very refined grains as a consequence of the shear deformation that takes place in the billet when crossing the intersection between channels. ECAP is based on increasing the free energy of polycrystalline alloys initial coarse grain, thru introduction high density of defects, especially dislocations [4].

The advanced materials science has got in central topics getting an optimal combination of properties of hardness and plasticity simultaneously. The interest increasingly higher in all used or potential severe plastic deformation methods of grain refinement is related to the fact that homogeneous pore-free polycrystals with ultrafine grain can be achieved currently. In this way ECAP is far one of the most promising SPD methods due to its potential for industrial exceeding the limits [5].

The properties of bulk nanostructured or UFG alloys differ very much from those polycrystalline with the same average chemical composition, massive



with micrometer scale. In case of ECAP, the grain size of the final product can be varied by controlling: die designed angles ( $\Phi$  and  $\psi$  the outer angle), pressure, number of successive passes, processing route. Two of the most important contribution are processing route and die angle because of slip process during ECAP. They are mostly reflected in the contributions of newly activated slip systems and reversed slip systems at the pass-to-pass processing, [6] different for each route applied.

In the present work we studied technical pure copper, which especially occur the grain size and influence of deformation, often deviates from simple shear, due to the existence of friction, strain hardening of material, or die design.

ECAP are feasible process for bulk nanostructure or ultrafine grain materials for copper alloys, whose performance increased spectacular by severe deformation. That allows more judicious use of copper alloys in the industries.

## 2. Experimental

This study was carried out on a technical pure copper, supplied as rolled billets 10 mm x10 mm and cut at 10mmx10mm x50mm. The billets were pressed in ECAP die with channel section 10mm x10 mm. The specific die angles, inner  $\Phi$  90<sup>o</sup> and outer  $\Psi$  13<sup>o</sup> determine effective strain 1.07 in one pass [7].

Specimens were pressed via route C at room temperature. After first pressing the ECAP die was rotated and the specimen was pressed back in the vertical channel. Then specimen was pushed without extraction 8 passes, only with die rotates. The constant pressing was employed using a 20 tf press. Before pressing the samples were lubricated with a suspension of graphite in mineral oil to reduce friction. The speed of pushing plunger was 17.3 mm/s. Similar ECAP process was conducted to obtain specimens with 1, 2, 3, and 8 passes, equivalent strain: 1.07, 2.14, 3.21, respectively 8.56.

Following the ECAP procedure were obtained eight samples, with different equivalent strain. The samples were used for investigations after severe plastic deformation. The force variation in both processes, ECAP respectively direct extrusion was monitored with Hottinger Spider 8 system and force-stroke data was recorded.

Micro-Vickers hardness measurements were made on center and margin ECAP samples in longitudinal section using a digital instrument 400DAT2 NAMICON, fitted with of accuracy optical and electrical systems. HV<sub>0.05</sub> measurements were made using 50gf pressing force, pressing for 30 seconds, five determination for every sample on center and 2-3 $\mu$ m on margins.

The optical microscopy study has been carried out using a microscope Olimpus BX45 with digital image resolution at higher magnifications. Metallographic samples were processed in longitudinal section for ECAP deformed samples and attacked to specific reagent, ferric chloride.

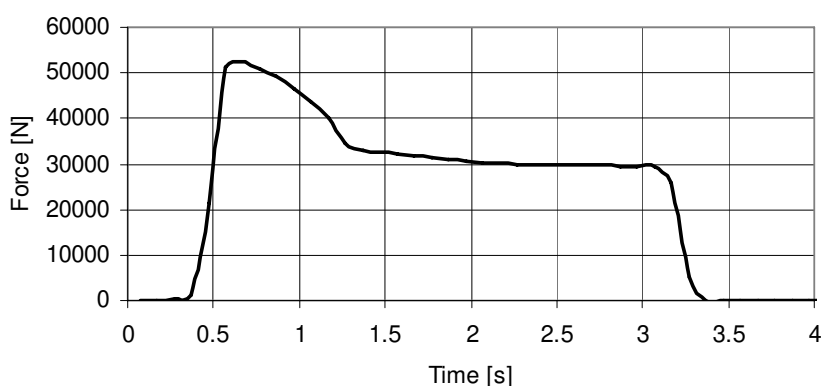
## 3 Result and discussion

### 3.1. Variation of force in ECAP process

Variation of the extrusion force in equal channels angular pressing specifics looks in concordance with similar observation on copper ECAP severe deformation.

When the first layer of material leave the plan shear zone of die, force increases until it reaches a maximum. From the moment force tends to reduce until a value that maintain during deformation appearance a plateau, after which suffers slump in the finish zone of deformation. In figure 1 is presented force versus time of deformation plot for effective plastic strain 8.56 at eight pass.

Maximum force is between 93.646kN and 46.823kN. The maximum value was obtained on sample after first ECAP step. In this case of copper force trend is decreasing pass to pass.



**Fig. 1.** Variation of force in the eighth pass of ECAP process - effective plastic strain 8.56

Variation of force is consistent in the sense that after reach its peak force tends to form a plateau and after all sample cover decrease. In ECAP process force increased continuously until the maximum is achieved then take places a small decreasing variation. To the end of ECAP process force became almost constant. After all billet lives zone of deformation, force decreases dramatically to zero. Entire process takes place in about 25 until 30 seconds.

### 3.2. Microhardness

Micro-Vickers hardness measurements values are presented in Figure 2. Were taken into account the values of severely plastically deformed ECAP samples with different degrees of deformation and measured values in center and at 2 3μm from margin. Note that all samples ECAP increase value of microhardness with each repeated deformation. Hardness value increased by 1.66 times from 78MPa for sample in initial state to 130MPa for sample after eight ECAP passes, in center billets. Same increase took place at the edge samples.

At low temperatures, the increasing of grains boundaries behave as slip barriers, their area being far increased than in micrometric grains bulk alloys. In case of nanomaterials are specific a high density of imperfections and dislocations with different settlement at grain boundaries.

That affects significantly the mechanical properties. Due to their reduced grain size, increase numbers of atoms on surface, nanomaterials are expected to become more ductile at the same temperature then coarse grained polycrystalline alloys with the same composition. More of that, ultrafine grained materials (100–500 nm) exhibit increased yield strength along with good ductility in comparison to nanograined materials. It has been correlated changes in strain hardening behavior with change of grain sizes [2, 3].

Severe plastic deformation leads to an advanced finishing structure. As a consequence hardness increases with increasing deformation. Note that the true deformation degree threshold value 8.56 above which plastic deformation by ECAP have still effect on mechanical properties.

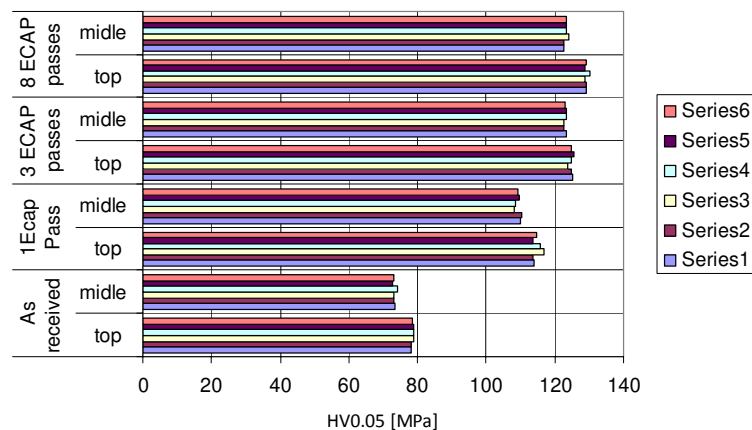


Fig. 2. Micro hardness versus number of ECAP passes (middle and top of X plane)

### 3.3. Study microstructure of technically pure copper severely plastically deformed samples by ECAP

In the investigation were studied by light microscopy copper specimens.

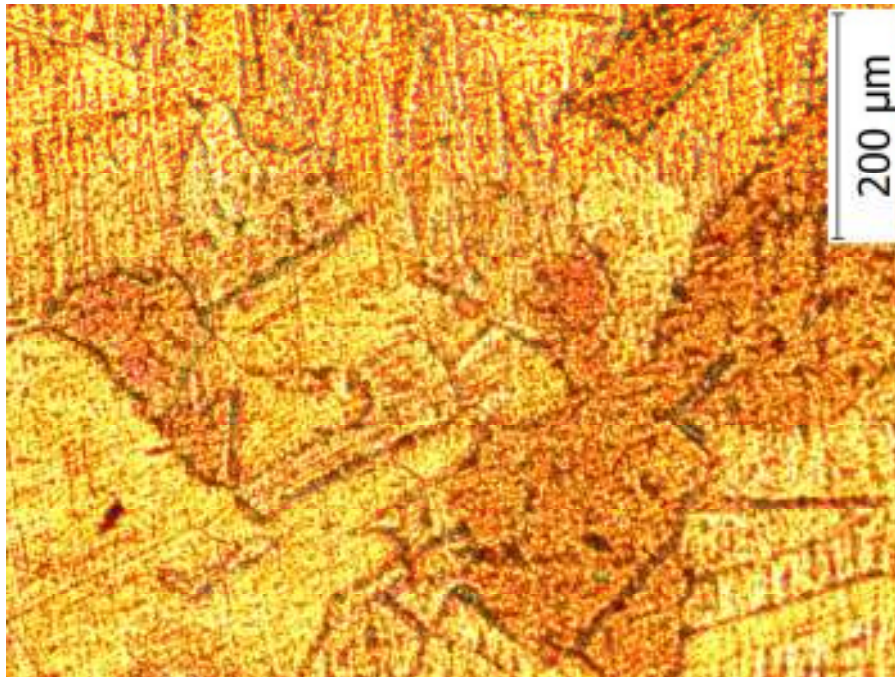
The specimens were observed in initial state and also after severe plastic deformation by ECAP process, with 1, 3 respective 8 passes by route C. Metallographic samples were processed in longitudinal section.

In the initial state in the sample are highlighted undistorted structure consists of a coarse-grained  $\alpha$

solid solution and rarely fine intermetallic compounds precipitated [Fig.3].

The specimens in initial state were solubilized prior to severe plastic deformation.

After solubilization the microstructure of specimens present only equiaxed grains with dimensional inhomogeneity, polyhedral shaped, with straight edges and numerous twins homogenously distributed specific to fcc crystallographic cell. Grain size is about 35μm but is observed also finer grain as 10μm. Grain uniformity is quite obvious. On grains boundaries are evident preferential nucleation of fine precipitates black colored.



*Fig. 3. Optical micrography of copper as received*

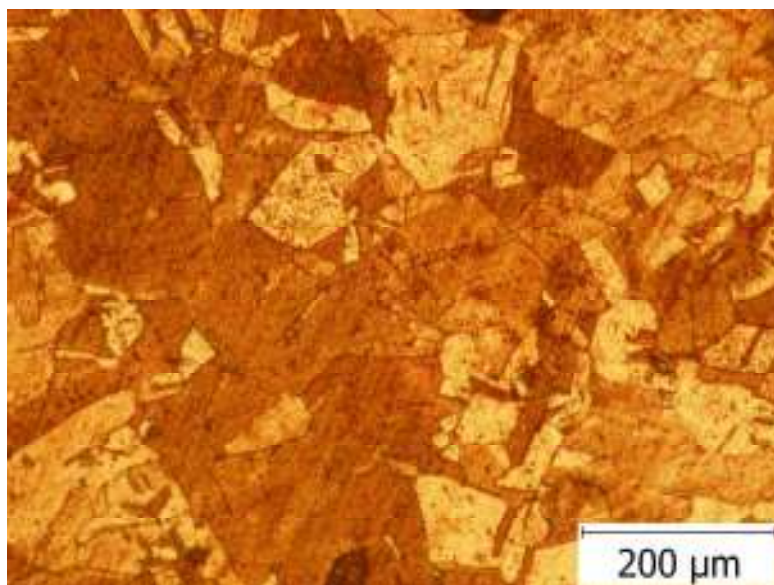
Microstructural aspect of copper after plastic deformation by ECAP method for each successive passages 1, 3, 8 of processing using route C are given in Figures 4-8.

On the outer surface of the sample which is in contact with the mold, especially in entrance area mold took place texturing in longitudinal section of solid solution  $\alpha$ . The phenomenon of distorted appeared even the material is not yet in deformation. Crystalline grains are slightly deformed. Intermetallic

compounds are observed such as dark particles. Texture is only because friction with the mold walls.

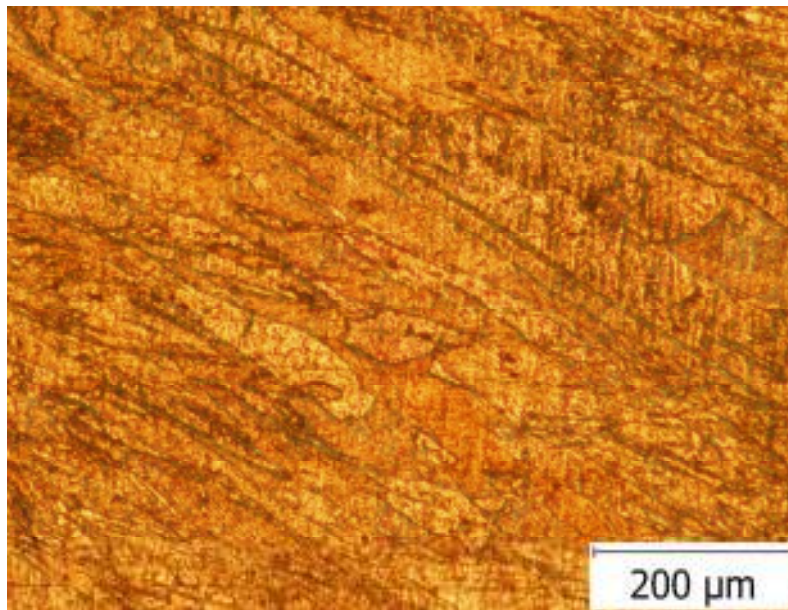
Prior to severe deformation, all rectangular samples were lubricated all over longitudinal contact with the mold.

One possible reason is the effect of friction texture appearance that can not be completely excluded. We strongly believe that at least at beginning of severe deformation process friction is an important factor to be considered.

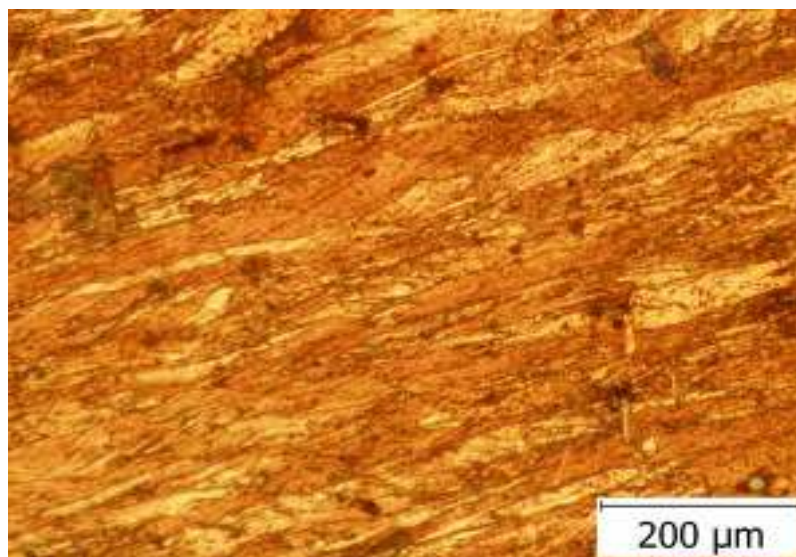


*Fig. 4. Optical micrography Copper in entry area of inner channel*





*Fig. 5. Optical micrography Copper after one pass ECAP*



*Fig. 6. Optical micrography Copper after three passes ECAP at the output of channel*

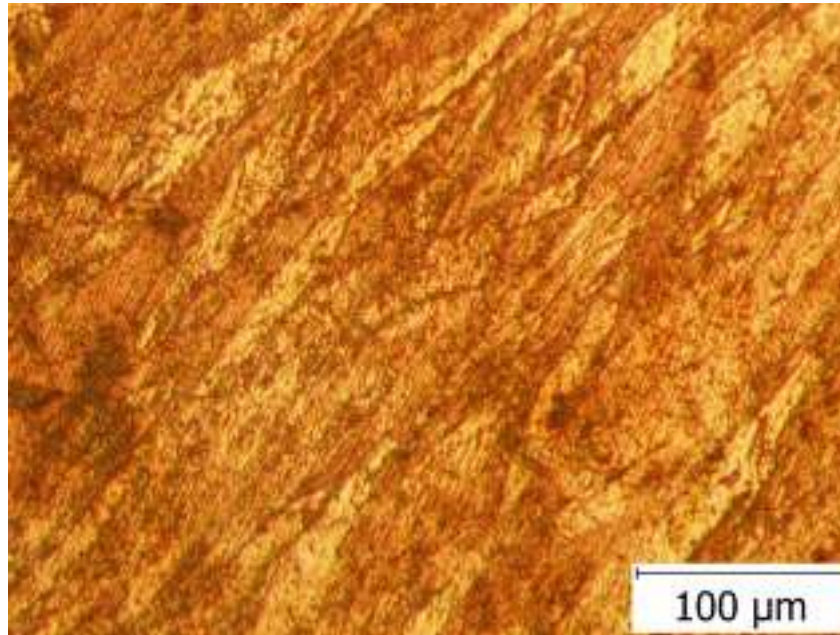
Copper micrographs after one pass ECAP disclose a significantly refinement of grains size and also modification of shape. The new structure is excessive elongated. The grains boundaries have lamellar aspect with parallel strings. The refinement and elongation is due to increasing density of dislocations. The ECAP process is based, like all severe plastic deformations, on high density of dislocations, Fig. 6.

The shape of grains is more and more elongated as the number of passes increased. The grains size is finer and finer. The aspect of grains is corrugated. Waving of the grains is a phenomenon that accompanies severe plastic deformation figures 6 and

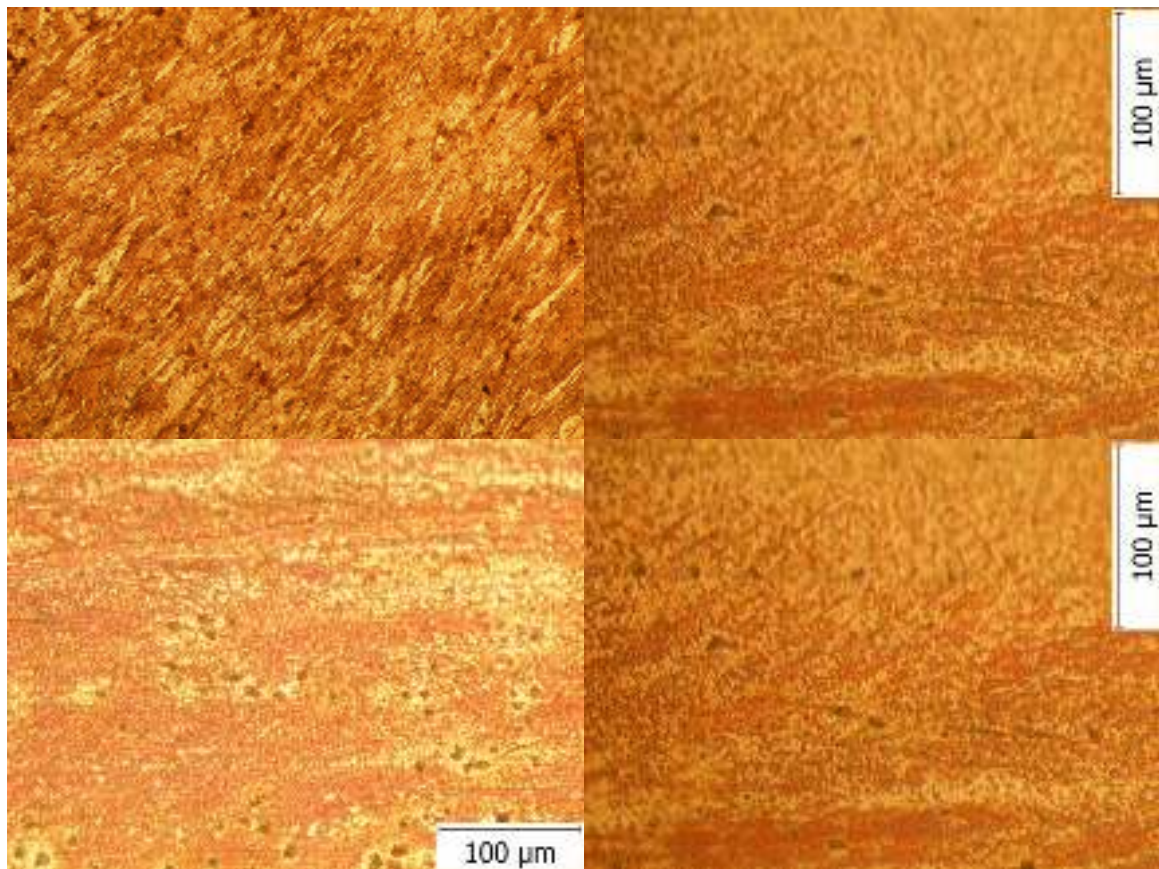
7. In the microstructures of samples after eight passes ECAP it can be observed only flow lines. The grains boundaries no longer distinguished by OM it can be seen fiber of deformation, Figs. 8 a, b, c, d.

The plastic deformation took place almost monotonically in share plan. The share plan is at the intersection between inner channel and outer channel. The solid solution grains begin to refined and corrugated from firs pass of deformation. The deformation is produced by successive shear of grains that are already refined in previous passes. The structure of SPD samples present aligned bands more refiner which highlighted only flow lines in the eighth passes.





*Fig. 7. Optical micrography Copper after three passes ECAP central area*

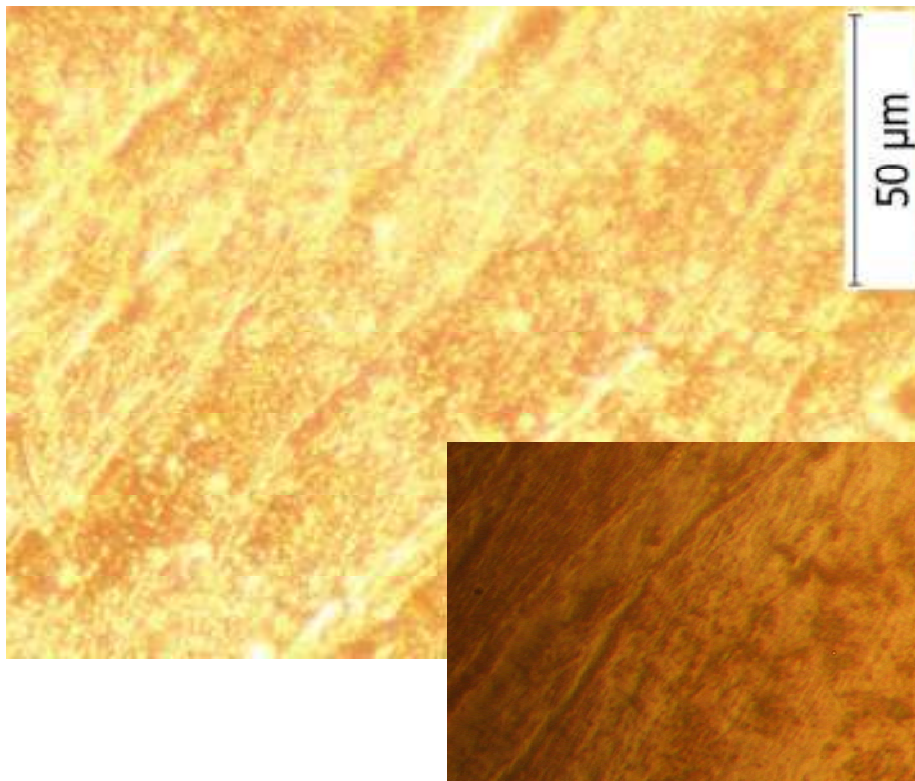


*Fig. 8. OM Copper after eight passes ECAP. Longitudinal section of sample: a) left side, b) central area at superior edge, c) central area, d) right side*

As the degree of deformation increases in the microstructure of samples, it can be observed significant differences, regarding to the internal structure. In the first step microstructure are elongate, after each pass the structure became finer and afterwards ultrafine. The grains boundaries become increasingly less visible, only the fiber flow appears evident. The fiber structure is compressed in transversal direction and is rotated in extruded direction. Central area of samples from picture 9 c, d and e highlighted parallel fiber lines which make an

angle of  $65^{\circ}$  to the vertical direction of extrusion. The aspect of microstructure is uniform and ultrafine. In OM can be seen only alginate bands to shear plan. Inside solid solution it can be observed the same refining of insoluble particles dark colored. Some authors consider that part of these particles can be dissolved in solid solution because of thermal effect in severe deformation by ECAP.

The microstructure aspect of samples after eight passes route C is one very dense with flow lines at  $65^{\circ}$  in all volume.



**Fig. 9.** OM Copper after eight passes ECAP in central area 1000X and detail 2000X

The grain size finishing and also fibrous texture was determined by increasing deformation degree by ECAP process. Extruded samples after eight passes ECAP deformations by route C, have only fiber lines (Fig. 9).

#### 4. Conclusions

Severe Plastic Deformation processes leads to ultrafine grained microstructure even nanostructure. These processes works at high pressure (GPa) and high deformation degrees.

Characteristic for SPD are an intense share process in transverse section of sample and unchanged shape of metal volume (ECAP particular case). The initial grains are divided in finest subgrains

by slipping and rotation on various systems of sharing bands.

The equivalent strain is different for different materials and deformation conditions. Generally the equivalent strain is achieved in successive passes generally more than one.

For example in aluminum case are necessary 5 passes on route C as opposed to copper which need more than 8 passes. True strain starts from 1.07 after firs pass and goes to 5.35 after five passes.

That determines a change of grains shape.

The grains became elongated sometimes corrugated then are reduced gradually until gets simply flow lines. After eight passes for copper we can see only flow lines with fibrous aspect and dense surface.



## References

- [1]. **Ruslan Z. Valiev, Terence G. Langdon** - *Principles of equal-channel angular pressing as a processing tool for grain refinement*, Progress in Materials Science 51 (2006) 881–981.
- [2]. **A. Azushima, R. Kopp, A. Korhonen, D.Y. Yang** - *Severe plastic deformation (SPD) processes for metals*, Manufacturing Technology 37, (2008) 716-735.
- [3]. **H. Gleiter** - *Nanostructured Materials: Basic Concepts, Microstructure and Properties*, Forschungszentrum Karlsruhe, Institut für Nanotechnologie, Postfach 36 40, D-76021 Karlsruhe.
- [4]. **M.A. Meyers et al.** - Progress in Materials Science 51 (2006) 427–556.
- [5]. **S. Ramtani et al.** - *A revisited generalized self-consistent polycrystal model*, Int. J. Eng. Sci. (2008).
- [6]. **Saiyi Li.** - *A crystal plasticity-based explanation for the dependencies of grain refinement on processing route and die angle in equal channel angular extrusion*, Scripta Materialia xxx (2009) xxx–xxx.
- [7]. **A.R. Eivani, A. Karimi Taheri** - *A new method for estimating strain in equal channel angular extrusion*, Journal of Materials Processing Technology 183 (2007) 148-153.





## INFLUENCE OF NIOBIUM AS MICROALLOYING ELEMENT IN 3%Si STEEL GRADE FOR ELECTRICAL INDUSTRY

**Ana DONIGA**

„Dunarea de Jos” University of Galati  
email: ana\_doniga@yahoo.com

### ABSTRACT

*The paper presents the results of the laboratory research on the chemical composition and crystallographic texture in 3% Si steels and their influence on the level of magnetic losses in the final sheet.*

*The magnetic properties have been estimated by means of the core losses observed on samples taken from the three steels after the secondary annealing.*

*It has been noticed that the microalloyed Nb steel showed the highest percentage of Goss texture in the final sheet and the lowest values of the magnetic losses of the three steels under study.*

KEYWORDS: inhibitor phase, Goss texture, core losses

### 1. Introduction

The particles of the secondary phase are in the silicon steel either as inclusions proceeded from steel making for example: SiO<sub>2</sub> AL<sub>2</sub>O<sub>3</sub>; FeO, or as inhibitors of the grains - growth: AlN; TiN; NbN; NbC, MnS and so on.

By their size, shape and distribution, these secondary phases control grain-size growth during secondary recrystallization, which will influence the Goss texture level (110) [100], and therefore the core magnetic losses, the main characteristics of the 3% steel grade. The secondary recrystallization takes place when a certain grain-size is built-up, that

exceeds a critical diameter and has a different crystallographic orientation than that of the matrix.

In a layer near the surface of the cold rolled strip, the grains of (110)[100] texture are building up that are including the adjacent grains if these have same or similar orientation to this component. These are forming "the embryo" or "the potential nuclei" for the secondary recrystallization. [1]

### 2. Experimental materials and procedures

Within this study, three steels of different chemical composition have been investigated, as highlighted in Table 2.

*Table 1. Chemical composition of investigated steels*

Steel grade	Chemical composition (%)						
	C	Si	Mn	S	P	Al	Nb
A (MnS)	0.004	3.04	0.08	0.015	0.009	0.002	0.09
B (AlN)	0.004	3.02	0.07	0.020	0.013	0.007	-
C (NbCN)	0.003	3.04	0.07	0.022	0.009	0.01	-

Steel A originated from a commercially produced continuous cast slab, typical for the silicon steel produced in industrial conditions. The inhibitor phase in this steel is MnS. Steels B and C are laboratory melts of about 50 kg produced in a vacuum induction furnace with a pressure of 60 bar, where either AlN or Nb (C,N) have been selected as inhibitor phase in addition to MnS. The bulk chemical composition of the laboratory heats was similar to steel A of industrial production. For the study of the

secondary phases and their influence on the Goss texture, the specimens were taken from the hot and cold rolled strips, after primary annealing, and from the finished strip, after annealing of the secondary recrystallization [2].

The texture was determined by a reflection method and the volume fractions of the various texture components by an inverse pole figure method. Furthermore, torque measurements were used to confirm these findings. The core losses of the

transformer sheets from the laboratory studies were determined for inductions of 0.5, 1.0 and 1.5 T using single strip samples of 30 mm width and 180 mm length, and were compared with data from industrial production.

### 3. Results and discussions

#### 3.1. Hot rolled samples

All specimens showed a rather high amount of silicate inclusions, often in the form of stringers. Furthermore, steel A contained also elongated manganese sulphides and the two laboratory heats B and C exhibited complex globular inclusions, identified as (Ca, Al, Mn) oxy-sulfides. Besides these inclusions, which had a size of a few micrometers, fine particles of < 100 nm were also found.

These particles were identified by X-ray diffractometry as MnS in steel A, AlN in steel B and both, NbC and NbN, in steel C.

The severity of the Goss texture in the hot rolled samples also depended on the processing conditions. Figure 1 shows that a finish rolling temperature of 1000°C was most favourable to achieve a high amount of the (110)[100] orientation, especially when the higher cooling rate was applied.

The observed reduction in the volume fraction of the Goss texture with higher finish rolling temperatures than 1000°C is according to expectations.

The lower volume fraction of the Goss texture obtained after finish rolling at 900°C is probably caused by a certain transformation from  $\alpha$  into  $\gamma$ -iron at this temperature.

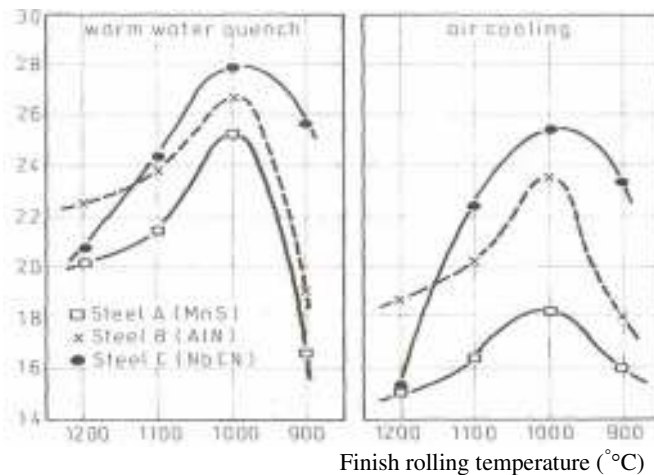


Fig. 1. Influence of hot rolling conditions on the volume fraction of Goss texture

#### 3.2. Cold rolled sheet

In all three cold rolled and annealed steels the volume fraction of the Goss texture was higher than in the hot strip material. It also increased with longer annealing time and in most cases was higher with a

higher annealing temperature. However, for the longest annealing time and the highest annealing temperature tested in this study, not necessarily the highest volume fraction of the Goss texture was obtained, Figure 2 [3].

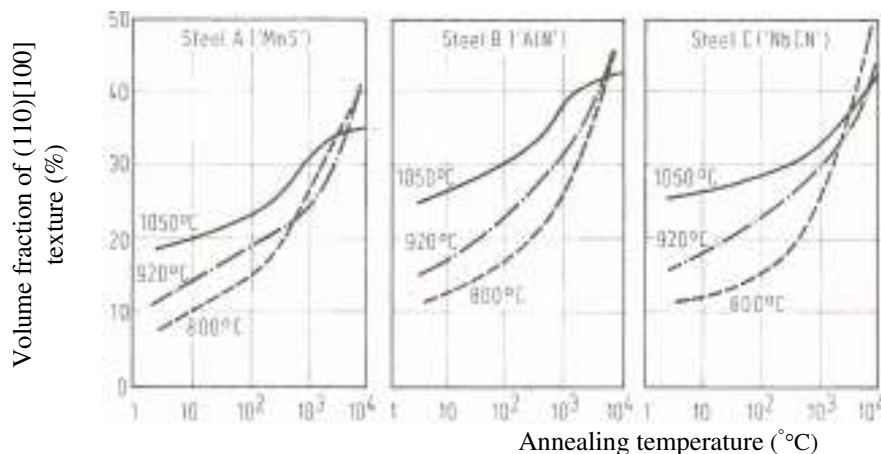
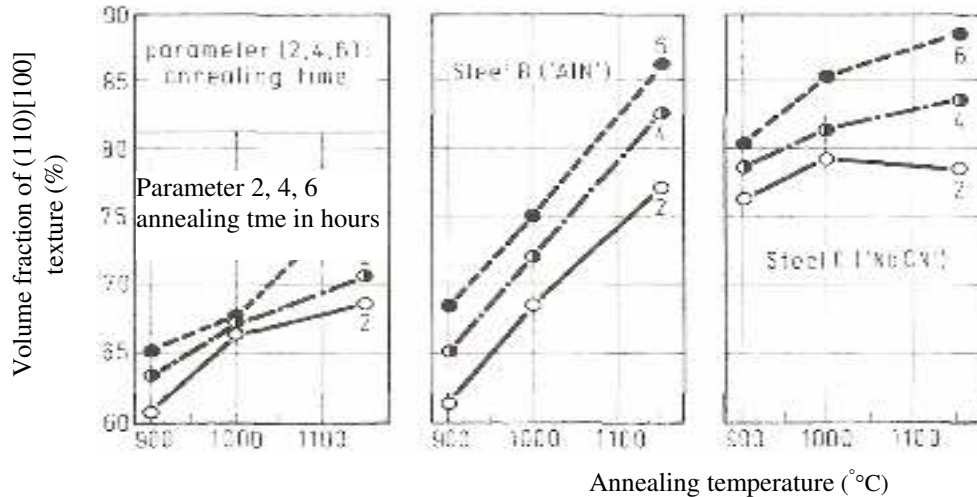


Fig. 2. Volume fraction of the Goss texture after 1<sup>st</sup> recrystallisation annealing



Samples, annealed by recrystallisation at 920<sup>o</sup>C for 5 min were further cold rolled by 50 %. Then the second primary recrystallisation plus decarburisation heat treatment and finally the secondary recrystallisation annealing were carried out. Figure 3 shows that the absolute value of the Goss texture

exhibited more than double the volume fraction compared to the observation after the first recrystallisation treatment. Furthermore, the Goss orientation increased with higher annealing temperature and longer annealing time and the ranking of the three steels became more pronounced.



**Fig. 3.** Goss texture development during secondary recrystallisation

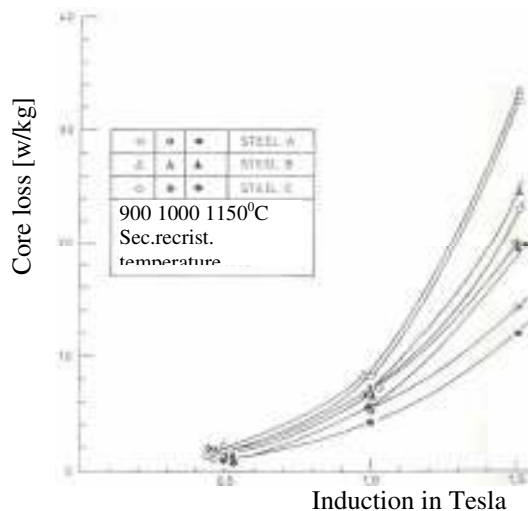
Steel C, based on Nb(C,N) as inhibitor phase showed a (110)[100] volume fraction of more than 75% already at the lowest annealing condition tested, i.e. at 900<sup>o</sup>C for 2 h, and also exhibited the highest value with 88.5%. On the other hand the second best steel B, based on the AlN technology required an annealing temperature of 1150<sup>o</sup>C to obtain a volume fraction of more than 75% of the Goss texture. This is a clear indication of the effective role of Nb(CN) in controlling the grain size which has been drastically reduced after decarburisation, during the first recrystallisation allowing the Goss texture to grow easily. On the other hand the dissolution of AlN particles obviously needs higher temperatures than

necessary for Nb(CN) and thus is in agreement with the solubility products.

These results confirm that the both the Goss and the cube texture, which are present already in the hot rolled material, are stable orientations and were not reduced during cold rolling and primary recrystallisation and the (111)[112] orientation rotates during the secondary recrystallisation to the desired (110)[001] texture component [...].

### 3.3. Core losses

The measurements results obtained with transformer sheets of laboratory trials were compared with industrial production data in Figure 4 [4].



**Fig. 4.** Core loss of steels A, B, C as a function of secondary recrystallization temperature and induction



An inspection of Fig. 4 revealed first that Niobium microalloyed silicon transformer steel in which the niobium carbo-nitrides are the inhibiting second phase has also the lowest core losses, followed by the silicon steel in which the inhibiting second phases are AlN and MnS. This is in good agreement with the higher volume fraction of the (110)[001] Goss texture of the niobium bearing steel developed during the secondary recrystallization high temperature anneal.

#### 4. Conclusions

From solubility product considerations, Nb(C,N) could be a suitable inhibitor phase. The characteristic features of an inhibitor phase are the control of the grain size during the first and second primary recrystallization and permitting the formation of a high volume fraction of the Goss texture during the secondary recrystallisation annealing.

Since niobium also forms carbides, this element might add to ageing stability of the final product, which is not possible by other elements that are typically applied. A two stage cold rolling schedule with an intermediary recrystallisation treatment was necessary to obtain a sharp the Goss texture. In this case a higher annealing temperature and longer holding time during the secondary recrystallisation were favourable for the Goss texture maximisation and the Nb(C,N) variant again gave the best results. Furthermore, the dissolution kinetics of this inhibitor phase opened the possibility to obtain the desired texture already at lower annealing temperatures.

Consistent with the highest volume fraction of Goss texture, the core losses were lowest with the Nb(C,N) inhibitor phase compared to variants with AlN or MnS.

Silicon steel processed via a single stage rolling schedule and total deformation being not higher than 80% will also exhibit relatively low core losses when using niobium microalloying, as a result of the already high level of Goss texture component obtained after the hot rolling operation. This is a technology that can be applied to electrical industry steel sheets manufacturing.

The relatively high volume fraction of Goss texture already existing in the hot rolled material and the effective behaviour as inhibitor phase makes niobium an interesting alloying element for optimising grain oriented electrical sheet. Confirmation of these laboratory results in industrial production is foreseen.

#### References

- [1]. Doniga A., Preda A. - *The consequence of the secondary phase particles in 3% Si steel grade for transformers*, Annals of "Dunarea de Jos" University of Galati, (2001), pag.32-35.
- [2]. Doniga A. - *Secondary phase part of the oriented grains silicon steels*, Rev. Metalurgia International, nr.8/2010 Suplimentar, pag.15 – 19.
- [3]. Hulka K, Vlad C, Doniga A. - *The role of niobium as microalloying element in electrical sheet*, Steel Researches 73 nr 10 /2002, p.453- 460.
- [4]. Doniga A, Vlad C, Hulka K. - *Development of the Goss texture in niobium bearing silicon transformer steel*, Metallurgy and new materials researches, vol VIII, nr.4/2000, ICEM Bucuresti p. 29.



## ENERGETIC AND EXERGETIC EFFICIENCIES OF BIOMASS GASIFICATION PROCESSES

**Daniela TASMA, Tănase PANAIT, Alexandrina TEODORU,  
Georgiana G. ROLEA**

"Dunarea de Jos" University of Galati  
email: dtasma@ugal.ro

### ABSTRACT

*A promising way to use biomass for the production of heat, electricity and other biofuels is through biomass gasification. In the gasification process, the chemical energy of the solid fuel is converted into the chemical and thermal energy of the gas produced. The paper presents the energy and exergy analysis results concerning a biomass gasification process. The use of exergy efficiency gives a clear picture of the quality of energy conversion of biomass into product gas. Energetic efficiency values are higher than the values obtained by the exergetic efficiency analysis.*

KEYWORDS: biomass, energy, exergy, efficiency, gasification

### 1. Introduction

Because of the continuous rise of the cost of fossil energy resources, biomass looks as one of the most promising and viable alternatives, being classified as the third energy source after coal and oil. It is renewable and neutral concerning carbon dioxide emission issue. Biomass resources include wood and wood waste, agricultural crops and their waste by-products, municipal solid waste, residues from agro-industrial and food processes, aquatic plants such as algae and water weeds [1].

A promising way to use biomass for production of heat, electricity and other biofuels is through biomass gasification. In the gasification process, the chemical energy of the solid fuel is converted into the chemical and thermal energy of the gas produced [2]. Gasification is partial thermal oxidation which results in a high proportion of gaseous products (CO<sub>2</sub>, water, CO, hydrogen and gaseous hydrocarbons), solid products (small quantities of char), ash and condensable compounds (tars and oils). The gas produced is easier and more versatile to use than the original biomass. The oxidant or gasifying agents can be air, pure O<sub>2</sub>, steam, CO<sub>2</sub> or their mixtures. Air is a cheap and widely used gasifying agent. This oxidant contains a large amount of nitrogen which lowers the heating value of the gas produced.

The heating value of the gas produced will increase if pure O<sub>2</sub> is used as the gasifying agent, but the operating costs will also increase due to O<sub>2</sub> production costs. If steam is used as the gasifying

agent, the heating value and H<sub>2</sub> content of the gas produced can be increased. The use of CO<sub>2</sub> as the gasifying agent is promising because of its presence in the gas produced. CO<sub>2</sub> with a catalyst can transform char, tar and CH<sub>4</sub> into H<sub>2</sub> and CO, thus increasing H<sub>2</sub> and CO contents. A mixture of steam or CO<sub>2</sub> and air or O<sub>2</sub> can be used as the gasifying agent, and the partial combustion of biomass with air /O<sub>2</sub> provides the heat required for gasification [3]. The choice between gasifying agents depends more on the required gas compositions. For steam gasification, the gas produced contains mainly methane and carbon dioxide and for air gasification the main product gases are hydrogen, carbon monoxide and nitrogen.

The gasification process consists of the following steps: pre-heating, drying, pyrolysis, char gasification, char-oxidation and ash formation. Different gasifiers are employed in the gasification process: fixed bed, moveable bed and fluidized bed.

The objective of this paper is to determine the energetic and exergetic efficiencies of the biomass gasification process. To provide an efficient and effective use of fuels, it is essential to consider the quality and quantity of the energy used to achieve a given objective. According to the first law of thermodynamics, energy can never be lost. Energy conversion processes do not have energy losses, except for losses from the process system into the environment. The second law of thermodynamics should also be considered. Energy conversion processes are accompanied by an irreversible increase in entropy, which leads to a decrease in exergy

(available energy). Thus, even though the energy is conserved, the quality of energy decreases because energy is converted into a different form of energy from which less work can be obtained [4].

Exergy is the expression for loss of available energy due to the creation of entropy in irreversible systems or processes. The exergy loss in a system or component is determined by multiplying the absolute temperature of the surroundings by the entropy increase. While energy is conserved, exergy is

accumulated. The use of exergy efficiency gives a clear picture of the quality of energy conversion of biomass into product gas. The following results depending on the moisture content in the biomass and gasification temperature are presented: compositions, higher heating values, physical and chemical exergies of the product gas, and energy and exergy based efficiencies [2]. The fuels were characterised by means of the higher heating value (HHV), elemental analyses and energy density (Table 1).

The higher heating value, in [MJ/kg], was calculated by the following equation:

$$\text{HHV} = 0.3491C^{\text{db}} + 1.1783H^{\text{db}} + 0.1005S^{\text{db}} - 0.1034O^{\text{db}} - 0.0151N^{\text{db}} - 0.0211A^{\text{db}} \text{ [MJ/kg]} \quad (1)$$

where  $C^{\text{db}}$ ,  $H^{\text{db}}$ ,  $O^{\text{db}}$ ,  $N^{\text{db}}$ ,  $S^{\text{db}}$  and  $A^{\text{db}}$  represent carbon, hydrogen, oxygen, nitrogen, sulphur and ash contents expressed in mass percentages on dry basis.

**Table 1. Fuel properties**

Fuel sample	Ultimate analysis (wt% of wet fuel with ash)						Higher heating value, HHV [kJ/kg]	Energy density [GJ/Nm <sup>3</sup> ]	
	C	H	N	S	O	Moisture			Ash
Acacia wood log	49.6	6.0	0.9	0.1	33.8	5.4	4.2	20793.11	14.97
Sawdust	50.0	5.9	1.8	0.0	33.6	6.0	2.6	20845.66	15.78

## 2. Energy and exergy calculations

The energy distribution of the biomass conversion process can be obtained from the energy balance [5]:

$$\sum_{\text{IN}} H_j = \sum_{\text{OUT}} H_k + Q_{\text{losses}} \quad (2)$$

where  $\sum_{\text{IN}} H_j$  and  $\sum_{\text{OUT}} H_k$  are enthalpy flow of all entering and leaving material streams, respectively, and  $Q_{\text{losses}}$  is the energy lost during the gasification process.

$$\sum_{\text{IN}} H_j = H_{\text{air}} + H_{\text{dry biomass}} + H_{\text{biomass moisture}} + H_{\text{steam}} \quad (3)$$

$$\sum_{\text{OUT}} H_k = H_{\text{produced gas,dry}} + H_{\text{unconverted carbon}} + H_{\text{steam}} \quad (4)$$

$$Q_{\text{losses}} = f \cdot \left( \sum_{\text{IN}} H_j \right) \quad (5)$$

This energy balance is responsible for the determination of the temperature of the system for a given air-to-fuel ratio, or the other way around.

The exergy balance of the biomass conversion process can be represented in the following form:

$$\sum_{\text{IN}} E_j = \sum_{\text{OUT}} E_k + I \quad (6)$$

where  $\sum_{\text{IN}} E_j$  and  $\sum_{\text{OUT}} E_k$  are exergy flows of all entering and leaving material streams, respectively.

$$\sum_{\text{IN}} E_j = E_{\text{air}} + E_{\text{dry biomass}} + E_{\text{biomass moisture}} + E_{\text{steam}} \quad (7)$$

$$\sum_{\text{OUT}} E_k = E_{\text{produced gas,dry}} + E_{\text{unconverted carbon}} + E_{\text{steam}} \quad (8)$$

The difference between all entering exergy streams and that of leaving streams is called irreversibility (I), and it is given by the following equation [6]:

$$I = T_0 S_{\text{gen}} \quad (9)$$

where  $S_{\text{gen}}$  is the rate of entropy generation.

The reference state was taken as  $t_0 = 25^\circ\text{C}$  and  $p_0 = 0,1013\text{MPa}$ .

For the exergy flow the amounts of chemical exergy and physical exergy are considered:

$$E = E_{\text{ch}} + E_{\text{ph}} \quad (10)$$

The standard specific chemical exergy of a pure chemical compound  $\varepsilon_{ch}$  is equal to the maximum amount of work obtainable when a compound is brought from the environmental state, characterized by the environmental temperature  $T_0$  and environmental pressure  $p_0$ , to the dead state, characterized by the same environmental conditions of temperature and pressure, but also by the concentration of reference substances in standard environment. The specific chemical exergy of the mixture is determined by:

$$\varepsilon_{ch.M} = \sum_i x_i \varepsilon_{ch,i} + RT_0 \sum_i x_i \ln x_i \quad (11)$$

The specific physical exergy can be calculated as:

$$\varepsilon_{ph} = (h - h_0) - T_0(s - s_0) \quad (12)$$

where  $h$  and  $s$  are enthalpy and entropy of a system at given temperature and pressure, and  $h_0$  and  $s_0$  are enthalpy and entropy of a system at the environmental temperature and pressure.

$$(h - h_0) = \int_{T_0}^T c_p dT \quad (13)$$

$$(s - s_0) = \int_{T_0}^T \frac{c_p}{T} dT - \int_{p_0}^p \frac{R}{p} dp \quad (14)$$

### 3. Energy and exergy efficiencies

The energetic efficiency of a gasification process can be determined as:

$$\eta = \frac{LHV_{gas}}{LHV_{biomass}} \quad (15)$$

where  $LHV_{gas}$  and  $LHV_{biomass}$  are the net heats of combustion (lower heating values) of gas and biomass, respectively.

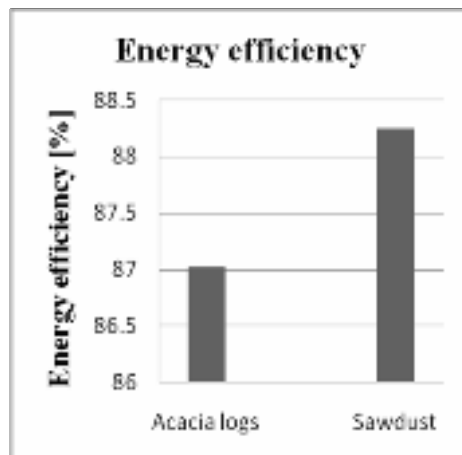


Fig. 1. Energy efficiency

The exergetic efficiency of a gasification process is the ratio between the chemical exergy of the gas produced and the biomass feed:

$$\psi = \frac{\varepsilon_{ch,gas} + \varepsilon_{ph,gas}}{\varepsilon_{ch,biomass}} \quad (16)$$

The specific chemical exergy of the biomass is calculated from the correlations for technical fuels using the LHV, calorific value of sulfur,  $C_s$ , and mass fractions of organic material,  $z_{org}$ , sulphur,  $z_s$ , water,  $z_w$ , and ash,  $z_A$ , in the biomass:

$$\varepsilon_{ch,biomass} = z_{org}(\beta \cdot LHV_{org}) + z_s(\varepsilon_{ch,S} - C_s) + z_w \varepsilon_{ch,water} + \varepsilon_A \varepsilon_{ch,ash} \quad (17)$$

$\beta$  is the chemical exergy coefficient and defined for solid hydrocarbons fuel (for  $O/C < 2$ ) as

$$\beta = \frac{1.044 + 0.0160H/C - 0.3493O/C(1 + 0.0531H/C)}{1 - 0.4124O/C} + \frac{0.0493N/C}{1 - 0.4124O/C} \quad (18)$$

where  $C$ ,  $H$  and  $O$  are the solid compounds of the species in the wood; their proportions are given in Table 1.

### 4. Results and discussion

The energetic efficiencies are shown in Figure 1, which shows a comparison between the results obtained for acacia wood logs and sawdust gasification. The highest value for energy efficiency is obtained from burning sawdust.

The value of energy efficiency is influenced primarily by the boiler load, the operating conditions and then by the fuel type. As observed, efficiency ratios are higher than the values obtained by the exergetic efficiency analysis. This could be explained by the fact that the  $\beta$  factor used to calculate the exergy input of the biomass is higher than 1 and thus, decreases the final efficiency value.

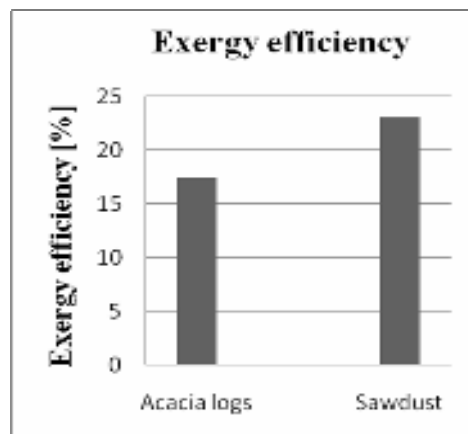


Fig. 2. Exergy efficiency





The exergy contained in the biomass is converted by gasification into the chemical and the physical exergy of the produced gas, and part of the exergy of the biomass is lost due to process irreversibilities. The exergetic efficiency shows the ratio between the exergy of useful gasification products and the feedstock exergy. This way different fuels can be compared based on the degree of utilization of their chemical exergy. Figure 2 shows that the exergetic efficiency is higher for sawdust than for acacia wood logs. The exergetic efficiencies of gasification process are lower than the energetic efficiencies.

The moisture content in the biomass is the main problem related to the gasification process. If it is too high, then there will not be enough energy (low temperatures) to start up the process. To take place, gasification needs temperature above 800K.

The moisture content is responsible for an increase in the destruction of exergy inside the reactor, as a result of an increase of the energy required to evaporate the moisture. Despite the increase in H<sub>2</sub> formation, the influence of thermal losses is similar to that of moisture. It reduces the energy available in the process and increases exergy destruction (heat transfer to the environment). Prins et al. [4] state that the main source of exergy destruction, in the gasification and oxidation processes, is the presence of chemical reactions. Following them, heat transfer between products and reactants is a second major source of exergy destruction. In this sense, pre-heating air and/or biomass might reduce such destruction, due to lower temperature differences between products and reactants. However, this reduction is quite small if compared with the increase of exergy destruction due to moisture or thermal losses [5].

## 5. Conclusions

In order to substitute fossil fuels by renewable fuels, solid biofuels could replace coal as a

gasification feedstock. Biomass is a resource which is paid more attention these days and it is classified energy as third energy resource after coal and oil. The gasification process appears to offer attractive technology and friendly to utilize biomass in energy generation.

This paper shows the results of the energetic and exergetic analyses of the biomass gasification process. The exergy contained in the biomass is converted by gasification into the chemical and the physical exergies, of the produced gas, and part of the exergy of the biomass is lost due to process irreversibilities. The exergetic efficiency of the gasification process is lower than its energetic efficiency.

## Acknowledgment

Publication of this paper was supported by Project SOP HRD – PhD EXPERT 21/1.5/G/19524. The work of this paper was supported by Project SOP HRD – EFICIENT 61445/2009 and by Project SOP HRD - SIMBAD 6853, 1.5/S/15 - 01.10.2008.

## References

- [1]. Antonio C. Caputo, Mario Palumbo, Pacifico M. Pelagagge, Federica Scacchia F. - *Economics of biomass energy utilization in combustion and gasification plants: effects of logistic variables*, Biomass and Bioenergy 28, (2005), pp. 35–51
- [2]. Rade Karamarkovic, Vladan Karamarkovic - *Energy and exergy analysis of biomass gasification at different temperatures*, Energy 35, (2010), pp. 537-549.
- [3]. Lijun Wang, Curtis L. Weller, David D. Jones, Milford A. Hanna - *Contemporary issues in thermal gasification of biomass and its application to electricity and fuel production*, Biomass and bioenergy 32, (2008), pp. 573-581.
- [4]. M. J. Prins, K. J. Ptasinski and F. J. J. G. Janssen - *Thermodynamics of gas-char reactions: first and second law analysis*, Chemical Engineering Science 58, (2003), pp. 1003-1011.
- [5]. Luiz Felipe Pellegrini, Silvio de Oliveira Jr. - *Exergy analysis of sugarcane bagasse gasification*, Energy 32, (2007), pp. 314–327.
- [6]. Abuadala A., Dincer I., Naterer G. F. - *Exergy analysis of hydrogen production from biomass gasification*, International Journal of Hydrogen Energy 35, (2010), pp. 4981-4990.



## THE CONSEQUENCES OF HEAVY METALS IMPACT ON PRIMARY TEETH

**Diana Daniela Daciana ZMARANDACHE, Rodica LUCA,  
Ioana-Andreea STANCIU, Cătălina FARCAȘIU**

Paediatric Dentistry Department,  
"Carol Davila" University of Medicine and Pharmacy, Bucharest  
email: [prelipceandaciana@yahoo.com](mailto:prelipceandaciana@yahoo.com)

### ABSTRACT

*Since the metals deposited in the teeth during formation and mineralization processes are to a large extent retained, human teeth receive a considerable attention as indicators of heavy metal exposure. The objective of the present work was to assess the relationship between the concentration of lead from the hard dental tissues of schoolchildren's deciduous teeth and the prevalence of dental caries. In 2008, a cross-sectional study was conducted on 157 children: 90 children from an industrial urban area (44 boys and 46 girls), mean age  $7.66 \pm 0.6$  years and 67 children from a reference area (31 boys and 36 girls), mean age  $7.75 \pm 0.6$  years. For dental status evaluation there were determined mean values and standard deviation for the following parameters: the number of caries free children, the prevalence index (Ip), the decayed, missing, filled teeth/surfaces (dmft/s index) and the Significant Caries index (SiC30 and SiC10). A correlation was made between these indices and the heavy metals concentrations from the temporary teeth collected from the two areas, the data being obtained from Politechnica University, Bucharest, our partner in a CNMP project. Statistical analyses were performed using the SPSS program.*

KEYWORDS: heavy metals, caries experience, primary teeth

### 1. Introduction

The subject of this paper – the consequences of the action of heavy metals on human teeth – brings to attention a topic that is probably not very commonly known within the technical world, but which could well be an interesting subject for interdisciplinary research.

It is common knowledge that disturbing actions of environmental factors during tooth formation (odontogenesis) may induce anomalies of dental hard tissues, known as tooth development anomalies [1-4]. These anomalies are evident at the moment of tooth eruption or become noticeable shortly afterwards and show that the subject was submitted to the negative influences of environmental factors during tooth formation [5,6].

It seems out of all environmental factors, heavy metals (lead-Pb, cadmium-Cd, magnesium-Mg, zinc-Zn and cooper-Cu) have a great impact on tooth formation and mineralisation, taking into account

their capacity of accumulation in time in heavy dental tissues [7-10].

Like in a bone, calcium can be partially substituted by a small amount of heavy metals [11-15]. This process is well known and may also take place in a tooth structure [15]. This is rather a complex process that is affected by various factors including the chemical form of the metal and its binding sites, age, gender, genetic inheritance and environmental quality [16,17]. Thus, the levels of the metals in teeth can be used to estimate especially the long-term environmental exposure [18].

During the last years, the dynamic behavior of dental structures from areas with heavy metal risk became the subject of some papers mainly for evaluating environmental effects on vulnerable groups of children, as their exposure and susceptibility are greater than those of adults. Studies conducted in Bahrein upon 280 primary teeth found toxic concentration of lead in 35% of the teeth of the studied children.

The level of lead in the teeth was not influenced by the child's sex, nationality, area of residence or socio-economic status [19]. Studies conducted in Germany reported higher levels of lead in children living in urban areas, compared to those from suburban/rural areas. The highest concentrations were found in children living in the smelter area and in those whose parents are lead-workers. The same studies reveal that lead level depends on the period of time the subject spent in the lead-smelter area as well as on the degree of local environmental pollution, in essence on the lead content of the atmospheric dust fall-out around children's home [20, 21].

Various studies on the consequences of high levels of lead in the teeth reported possible connections with a higher level of caries [3, 22]. However, there is no convergence of opinions on the matter. Because of the divergences in the literature and scarcity of data on this subject among Romanian communities, an epidemiological investigation was made in order to determine the relationship between the concentration of lead present in the enamel of Romanian schoolchildren's deciduous teeth and the prevalence of dental caries. The two target groups were selected from an industrial area, an urban area with high pollution, and from a reference area, a rural area from the mountain region of Romania.

## 2. Material and methods

An epidemiological, cross-sectional study was conducted upon first and second grade schoolchildren attending random schools from those towns. Sample 1 consisted of 90 children from Bucharest (44 boys and 46 girls), mean age  $7.66 \pm 0.6$  and median age 7.75 years. Sample 2 consisted of 67 children from Pătârlagele (31 boys and 36 girls), mean age  $7.75 \pm 0.6$  and median age 7.75 years (Figures 1, 2 and Table 1). The 6-7 years old is one of the ages recommended by WHO for children oral health evaluation because at this age primary dentition is in total functionality.

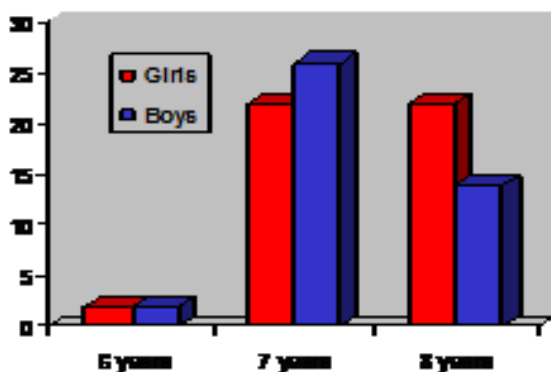


Fig. 1. Sample 1- Age and sex distribution

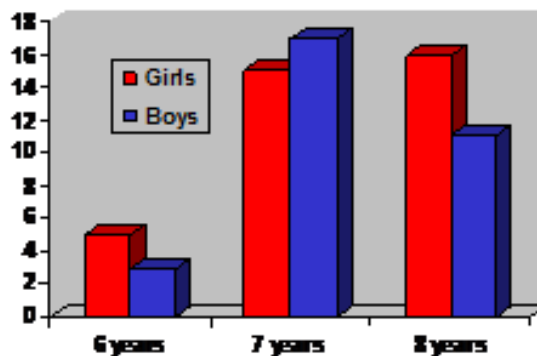


Fig. 2. Sample 2- Age and sex distribution

Written consent was obtained from the local public health authorities of the cities included in the study, from the local administration authorities and from the school authorities. The school authorities obtained the written informed consent from the parents of the recruited children.

The clinical examination was carried out in the school classes, using plain mouth mirrors, ball-ended dental probes under natural optimal light. Standard infection-control protocols were followed [23].

The World Health Organization (WHO) criteria were used for the caries diagnosis and registration [6]. Dental caries was diagnosed at the caries into dentine, using a visual method without radiography, fibre-optic transillumination, or compressed air. Enamel and precavitated lesions were excluded. The data were registered on individual charts: the presence and distribution of caries, fillings and missing teeth due to caries.

For caries experience evaluation there were determined:

- the number of caries-free children;
- the prevalence index (Ip);
- the dmft/dmfs indices – the sum of the number of teeth/surfaces decayed, missing/extracted or filled because of decay.

After the data were gathered and centralised, we analysed if there are any differences regarding the heavy metals concentration in the primary teeth belonging to the children born and raised in the two urban areas (Bucharest and Patarlagele). The primary teeth, extracted due to their exfoliation, were collected by the dentists from the local school dental clinic, in the same year with the examination. The heavy metals concentration were determined by the Politechnica University, Faculty of Applied Chemistry and Materials Science, our partner in a CNMP (National Centre of Management Programs) project. In this project, the "Carol Davila" University of Medicine and Pharmacy Bucharest, represented by the Paediatric Dentistry Department, provided the



primary teeth that were analysed, those teeth being collected during the exfoliation period.

The primary teeth belonged to all morphological types (incisors, canines and molars), were sound teeth and also decayed teeth.

Data were analyzed by using the statistical package SPSS v. 16.0. Associations of variables were tested by means of ANOVA unifactorial tests and Independent sample t-test at the 5% level of significance.

For heavy metal level determination an ELAN DRC-e induced plasma coupled spectrophotometer was used (ICP-MS). This method is a type of mass spectrometry that is highly sensitive and capable of the determination of a range of metals and several

non-metals at concentrations below one part in  $10^{12}$  (part per trillion) [24-26].

### 3. Results

#### 3.1. Caries experience

The prevalence index, Ip, had very high values for both samples, in the urban area being 80%. The dmft index was  $4.21 \pm 3.43$ , and the dmfs index  $8.83 \pm 8.31$  (Table 1).

For the second sample, the Ip was 82.5% the dmft index was  $7.09 \pm 4.15$ , and the dmfs index was  $16.31 \pm 11.9$  (Table 1).

The differences between the data were statistically significant ( $p < 0.05$ ).

**Table 1.** Caries experience indices for both samples

Index	Sample 1	Sample 2	
Ip (%)	80	82.5	SS
Caries free (%)	20	17.5	SS
dmft	$4.21 \pm 3.43$	$7.09 \pm 4.15$	SS
dmfs	$8.83 \pm 8.31$	$16.31 \pm 11.9$	SS

#### 3.2. Heavy metals concentration in primary teeth

Our results were compared with those reported by the Department of Bioengineering and Biotechnology. The amount of heavy metals was determined for the extracted primary teeth, for each sex and for enamel and dentine. The tables below present the mean values obtained by our partner, because they calculated the concentrations for each kind of teeth (molars, canines and incisors).

The heavy metal concentrations were generally higher in Bucharest than at Patarlagele.

Regarding the heavy metal concentration for both sexes, the values were higher for the boys than for the girls.

Taking into consideration the concentration of the two layers, enamel and dentine, the amount of heavy metals from the enamel was higher than the dentine, although those metals are normally deposited mostly in the dentine [26].

**Table 2.** Heavy metal concentration in enamel-boys [26]

Area	Mn	Cu	Zn	Cd	Pb	Hg
	[ppm]					
Urban	30.5	44.03	36.13	57.21	38.32	29.6
Rural	24.04	45.5	25.7	37.16	15.6	10.74

**Table 3.** Heavy metal concentration in enamel-girls [26]

Area	Mn	Cu	Zn	Cd	Pb	Hg
	[ppm]					
Urban	42.5	56.16	51.06	38.14	38.56	28.16
Rural	11.05	53	5.95	46.5	5.2	9.35





**Table 4. Heavy metal concentration in dentin-boys [26]**

Area	Mn	Cu	Zn	Cd	Pb	Hg
	[ppm]					
Urban	26.46	33.48	26.17	39.55	16.5	12.45
Rural	10.07	34.72	10.05	22.1	2.1	5.42

**Table 5. Heavy metal concentration in dentin – girls[26]**

Area	Mn	Cu	Zn	Cd	Pb	Hg
	[ppm]					
Urban	35.7	45.84	41.7	28.24	16.64	17.2
Rural	9.7	45.05	5.2	39.15	4.95	8.25

In order to see if there is an association between the caries experience and the heavy metal concentration, the ANOVA test was used.

No statistical association was found between caries experience and the amount of heavy metals in these teeth (Table 6,  $p > 0.05$ ).

**Table 6. ANOVA test results**

Correlated parameters	ANOVA-p
Mn	0.56
Cu	0.72
Zn	0.85
Cd	0.76
Pb	0.32
Hg	0.25

#### 4. Discussion

There are few studies in Romania regarding the impact of heavy metals on hard dental tissues. In this respect, the purpose of our study was to analyze if there is any correlation between the heavy metal content in the enamel and dentine of primary teeth and caries prevalence from a polluted area and a reference area.

Based on human and animal studies, a number of 6 types of elements have been proposed in the literature, depending on their cariogenicity. This proposal which summarized the cariogenic effect of many of the minerals included in the cariostatic group some elements like F and P, and placed various heavy metals, such as Mn, Sn and Zn, in the range of middle cariostatic [27-29]. Other elements like Al, Ni and Fe are treated as caries inert, while some other aggressive heavy metals, like Cd and Pb are defined as caries promoting.

No defined reference values exist in the literature for the concentrations in dental enamel that would reflect a condition of lead poisoning or, furthermore, would relate to enamel defects and caries.

The studies in the Brazilian literature have established reference values only for blood and have reported the importance of verifying lead levels as a

routine examination. However, blood measurements indicate acute lead contamination, thus differing from dental enamel, which indicates past contamination [30].

The heavy metal content in the deciduous teeth was higher in children's primary teeth from the polluted town than the reference area.

The heavy metal content was bigger in enamel than in dentine.

Nonetheless, no relationship was found between any of the lead concentrations analyzed in the present study and caries experience in the deciduous teeth, but there is a correlation between these concentrations and local pollution.

It is needed to point out that there are many factors, including nutrition and socio-economic problems which may affect the caries experience and oral health in general and therefore a correlation is very difficult to be established.

Our results are in agreement with previous studies made in Piracicaba, Sao Paulo, on preschool children, which also found no correlation between the heavy metal content in high polluted areas and caries experience or enamel hypomineralisation [29].

Also in Poland no data was found that would give evidence of a relationship between the Cd, Cr, Cu, Fe, Mg, Zn, K, Ca and Mg concentrations in the decayed tooth roots and the sound teeth [29].



## 5. Conclusions

Many studies on this topic are needed, with focus on children from the same social category or other polluted areas in order to see if there is a correlation between caries experience and heavy metals.

## References

- [1]. F. Gil, A. Facio, E. Villanueva, M.L. Pérez, R. Tojo, A. Gil - *The association of tooth content with dental health factors*, Sci Total Environ (1996);192:183-91.
- [2]. A.H. Brook, J.M. Fearn, J.M. Smith - *Environmental causes of enamel defects*, Symposium on Dental Enamel, 1996, Ciba Foundation. Proceedings. New York: John Wiley & Sons, (1997).
- [3]. J.D. Spouge - *Developmental Abnormalities of Enamel*, Oral Pathology, C. V. Mosby Comp., Saint Louis, (1973):145-165.
- [4]. R. Luca - *Criterii de alegere si modalitati de tratament in unele distrofii ale smaltului, (Choosing criteria and treatment therapy in some enamel defects)*, Stomatologia (Bucuresti), (1996); XLIII (3-4):67-71.
- [5]. R. Luca, D. Constantinescu - *Consideratii etiopatogenice asupra hipoplaziilor de smalt de cauza locala (Etiopathogenic considerations on enamel local hypoplasia)*, Buletin informativ al Asociatiei Romane de Ortodontie Nr. 2 (Cursuri si lucrari stiintifice a filialei "ANRO" Bucuresti, 1995 si cel de al II-lea Congres "ANRO"), Ed. Medicala, Bucuresti: 13-16.
- [6]. R. Luca, *Conceptii actuale asupra amelogenezei (Actual conception on amelogenesis)*, Revista Nationala de Stomatologie (1998); I: 44-49.
- [7]. V.E. Gomes, R.F. Gerlach, M.L.R. Sousa, F.J. Krug - *Concentração de chumbo em dentes decíduos de pré-escolares de Piracicaba, SP, Brasil — Estudo Piloto. Lead Concentration from enamel preschool children from Piracicaba, SP, Brazil-Pilot study* Rev Odonto Ciência (2003);18:3-7.
- [8]. V.E. Gomes, M.L.R. Sousa, F.Jr. Barbosa, F.J. Krug, M.C.P. Saraiva, J.A. Cury, R.F. Gerlach - *In vivo studies on lead content of deciduous teeth superficial enamel of preschool children*, Sci Total Environ (2004); 320:25-35.
- [9]. P. Malara, J. Kwapulinski, B. Malara - *Do the levels of selected metals differ significantly between the roots of carious and non-carious teeth?* Science of the Total Environment (2006); 59: 369-373.
- [10]. I. Demetrescu, I.D. Iordachescu, D. Ionita, S. Manea - *Proceedings of Bioceramics 21 Conference*, Key Engineering Materials (2009); 35: 396-398.
- [11]. R.F. Gerlach, A.P. Souza, J.A. Cury, S.R.P. Line - *Effect of lead, cadmium and zinc on the activity of enamel matrix proteinases in vitro*, Eur J Oral Sci (2000);108:327-34.
- [12]. T.J. Simons - *Cellular interactions between lead and calcium*, Br Med Bull (1986); 42:431-434.
- [13]. G. Boivin, P. Deloffre, B. Perrat, G. Panczer, M. Boduelle, Y. Mauras - *Strontium distribution and interactions with bone-mineral in monkey iliac bone after strontium salt (S-12911) administration*, J Bone Miner Res (1996); 11:1302-11.
- [14]. J. Kwapulinski, B. Brodziak, M. Bogunia - *Relative change of elements in human osseous tissue*, Bull Environ Contam Toxicol (2003); 70:1089-96.
- [15]. M. Manea-Krichtchen, C. Patterson, G. Miller, D. Settle, Y. Erel - *Comparative increases of lead and barium with age in human tooth enamel, rib and ulna*, Sci Total Environ (1991); 107:179-203.
- [16]. H.M. Tvinnereim, R. Eide, T. Riise - *Heavy metals in human primary teeth: some factors influencing the metal concentrations*, Sci Total Environ (2000); 255:21-7.
- [17]. E. Burguera, Z. Romero, M. Burguera, J.L. Burguera, H. de Arenas, C. Rondon - *Determination of some cationic species in temporary teeth*, J Trace Elem Med Biol (2002); 16:103-12.
- [18]. B. Nowak, H. Kozlowski - *Heavy metals in human hair and teeth*, Biol Trace Elem Res (1998); 62:213-28.
- [19]. F. Al-Mahroos, F.S. Al-Saleh - *Lead Levels in Deciduous Teeth of Children in Bahrain*, Ann Trop Paediatr (1997); 17(2): 147-154.
- [20]. U. Ewers, A. Brockhaus, G. Winneke, I. Freier, E. Jermann, U. Kramer - *Lead in Deciduous Teeth of Children Living in a Non-ferrous Smelter Area and a Rural Area of the FRG*, Int Arch Occup Environ Health (1982); 50(2): 139-151.
- [21]. A. Brockhaus, W. Collet, R. Dolgner, R. Engelke, U. Ewers, I. Freier, E. Jermann, U. Kramer, N. Manojlovic, M. Turfeld - *Exposure to Lead and Calcium of Children Living in Different Areas of North-West Germany*, Results of Biological Monitoring Studies 1982-1986. International Arch Occup Environmental Health, (1988); 60(3): 211-222.
- [22]. G.E. Watson, B.A. Davis, R.F. Raubertas, S.K. Pearson, W. H. Bowen - *Influence of maternal lead ingestion on caries in rat pups*, Nature Med (1997); 3:1024-5.
- [23]. World Health Organization - *Oral Health Surveys: Basic Methods*. 4th ed. Geneva: W.H.O. Library Cataloguing in Publication Data; (1997).
- [24]. I. Demetrescu, R. Luca, D. Ionita, D. Bojin - *ICP/MS in evaluation heavy metal influence on the behavior of natural temporary teeth*, Key Engineering Materials (2009); 396-398: 175-178.
- [25]. M. Prodana, R. Luca, F. Miculescu, D. Bojin - *A new approach in evaluation surface properties of natural temporary teeth from high polluted area*, Key Engineering Materials (2009); 396-398: 21-24.
- [26]. I. Demetrescu, R. Luca, D. Ionita, M. Prodana - *The evaluation of heavy metals concentration of temporary teeth from areas with different pollution level*, Molecular crystal and Liquid Crystals (2010); 523: 73-81.
- [27]. M. Prodana, A. Meghea, G. Stanciu, R. Hristu - I. Demetrescu, *Aspects of correlation between the surface analysis and heavy metal content in temporary teeth from areas with various pollution levels of Romania*, International Journal of Environmental Science and Development (2010); 1: 47-52.
- [28]. K. Bercovitz, D. Laufer - *Carious teeth as indicators to lead exposure*, Bull Environ Contam Toxicol (1993); 50: 724-729.
- [29]. J. M. Navia - *Prevention of dental caries: Agents which increase tooth resistance to dental caries*, International Dental Journal (1972); 22:427-440.
- [30]. V. E. Gomes, R.S. Wada, J.A. Cury and Rosário de Sousa M - *Lead level, enamel defects and dental caries in deciduous teeth.* Rev Saude Publica (2004); 38(5):1-6.



## EVALUATION OF THE SONIC SYSTEM EFFICIENCY FOR RAW WATER TREATMENT

**Carmen CÎRNU, Marian BORDEI, Aurel CIUREA**

"Dunarea de Jos" University of Galati  
email: mbordei@ugal.ro

### ABSTRACT

*Water pollution is defined as the change in the water composition that is harmful to human health, unsuitable for economic use or reactive and that can cause damage to the aquatic flora and fauna. In the appreciation of the World Health Organization, approximately 2/3 of illnesses are due to polluted water, and the main pollutants come from industry. The paper presents an analysis of the technical systems used for raw water decanting with a view to making it drinkable.*

KEYWORDS: raw water, clarifier, sonic, ultrasonic, efficiency

### 1. Introduction

Through their process wastewater, mining and metallurgy industries are the main source of pollutants, such as lead, zinc, copper, cadmium, arsenic, mercury and others. Heavy metals generally act on living organisms as toxic substances, causing inhibition of cellular enzymatic processes or causing numerous other physiological disorders.

Process wastewater is potentially dangerous for the environment, because of direct or indirect chemical reactions. Some process waters are already biologically degraded process and thus require immediate oxygen demand.

The most harmful substances in industrial wastewaters are organic substances, suspended substances, toxic substances and heavy metals.

The efficiency, of the wastewater treatment is defined by the relation:

$$b = ((M-m) / M) * 100$$

where M is the initial concentration of the substance and m, its concentration after treatment. Efficiency is usually calculated for suspended substances, organic substances (expressed in CBO<sub>5</sub>), oxygen O<sub>2</sub>, pH and toxic substances [1].

### 2. Unconventional water treatment technologies

The conventional water treatment technology involves successive stages of settling, chemical treatment filtration with material consumption, high energy and labor, aspects that determined more and

more its replacement with more modern performative techniques.

Classic technologies present a number of disadvantages, reason for seeking alternative solutions to conventional processes, to eliminate these drawbacks and, in particular, to ensure a higher water quality.

Analyzing the technical systems for raw water decanting in view of making it drinkable, we can deduce that the most convenient solution is to use vertical clarifiers specific to the treatment of small and medium water flows (required municipalities below 10,000 inhabitants) which can be equipped with gas-dynamic sonic generators.

Concurrent processing with acoustic waves and aeration of technological is a liquids scientific novelty in the raw water treatment processes. Another novelty could be the coexistence with the helps of gas-dynamic sonic generators of two simultaneous processes: clarification (decantation) and disinfection. In the specialized bibliography it is recommended that the operating mode of ultrasonic systems to be intermittent. Using the sound and ultrasounds gas-dynamic generators can be beneficial to the process of aeration too because these devices enhance the diffusion of oxygen into the water and accelerate the chemical reactions between water and coagulant. Based on the analysis of types of generators the best can be considered the Lavasseur generator type, which is stable in operation and can provide airflow sufficient working small working pressures (up to 0.5 bar - specific pressure turbochargers existing in water plants) to provide raw water aeration processes [3, 6, 7].

### 3. Sonic decantation device

Given the fact that decanters are uncovered devices which retain suspended substances gravimetrically sediment from the raw water to be treated, they are located upstream the filters.

The number of settlers in operation is at least 2 units.

Vertical decanters (Fig. 1) can be circular or square shaped in plan, where the water movement is inverted, vertically. They are used for low flow rates, maximum daily flow less than 10,000 m<sup>3</sup> and diameters up to 10 m.

The working methodology in experimental research was as follows:

- develop a new method for calculating the gas-dynamic generators with two resonators and flat jet;
- developing the method for calculating the experimental vertical settler combined with accelerator type - ascending with the possibility to equip the sonic gas-dynamic generator;
- establish working arrangements for

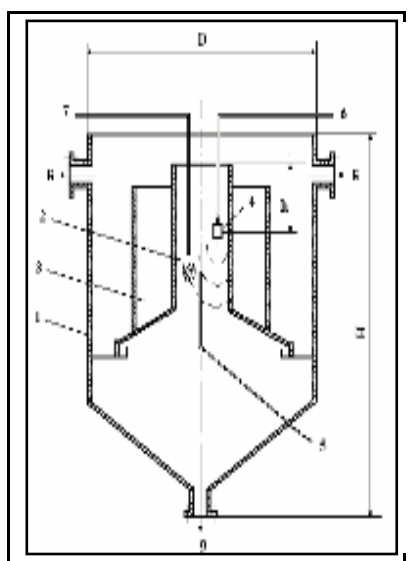
installations where the water flow is constant in the experimental decanter (raw water flow of 0.9144 m<sup>3</sup>/h of raw water upward speed of 0.145 mm/s);

- establishing the flow solution of the coagulating agent (a dose of 40 - 60g/m<sup>3</sup> aluminum sulphate Al<sub>2</sub>(SO<sub>4</sub>)<sub>3</sub>);

- establishing the intermittent working cycle of the sonic generator, depending upward speed of water and the capacity of the experimental decanter (effective operating of the time sonic generator of 60 minutes, alternating with rest periods of 5, 10, 15 or 20 minutes) diving depth generator in the reaction chamber (0, 0.5, 0.75, 1 m) and the generator placement to the chamber (axial or tangential to the wall - central);

- adoption of existing methods of acoustic measurements.

The preliminary tests of the experimental sonic decanter showed the maximum effect of sonic treatment at a distance of 40 mm from the central axis of the reaction chamber, almost tangential to the wall (cylindrical) chamber [2].



**Fig. 1.** Experimental sonic decanter:  
1 - decanter wall; 2 - mixing chamber; 3 - reaction chamber; 4 - sonic generator; 5 - Line pipes for raw water; 6 - working air duct of the generator; 7 - coagulant pipe; 8 decanted water-collection; 9 - sludge collector; D, H – diameter, respectively, decanter height; h - generator depth.

### 4. Influence of sonic generator operating mode with two resonators on physico-chemical and bacteriological quality parameters of raw water

Based on the experiments, the optimal ratio was determined between the period of operation of the generator and the rest period:  $t_{rap} = 5\text{min}/15\text{min}$ , set in an operating cycle of one hour, which is the average turbidity of  $T_x = 2.56\text{NTU}$ , and is lower than that obtained in the classical decanter (value between 4.2 and 4.8 NTU), which proves that the sonic decanter is more effective with 36.415% compared to a traditional decanter.

Due to the bi-acoustic frequency field (sonic frequency of 10.76 kHz ultrasonic frequency of 21.520 kHz), the following results were obtained:

- decrease of amount of water oxydisability (oxydisable organic substances) by 1.5 times compared to that obtained by conventional technology and 1.826 times compared to the raw water;

- reduction aluminum ions content in water of 1.66 times compared with traditional technology;

- decrease from 110 mg/L to 100 mg/L sulfate ion content in some water sonic decanted compared with classic decanting.

When replacing the sonic generator with an aerator in the experimental decanter, it was observed



that the value of oxydisability of the water decanted is more than 1.3 times compared to water treatment with generator.

This confirms that in parallel with the aeration through bubbling, occurs the water degassing due to cavitation processes. The influence of sonic generator operating mode with two resonators on parameters of microbiological quality of raw water was also studied: aerobic mesophilic bacterial number (mesophilic), the probable number of coliform bacteria (total coliforms), the probable number of thermotolerant coliform (fecal coliform), and the probable number of faecal streptococcus.

The sonic treatment of water has a significant bactericidal effect. In all experiments it was observed that the bacteriological indicator values are "0". No matter the effective functioning of sonic generator (from cyclical variations) or the immersion depth of sonic generator. The microorganisms, the behavior under the influence of the ultrasonic generator, depend on cavitation.

Thus, if the germs and streptococcus are destroyed by pressure waves produced by sonic waves, then total and fecal coliforms are resistant to sonic waves but destroy themselves at the cavitation bubble implosion (the so-called phenomenon "hot spot"). Due to the acoustic bi - the frequency field (sonic frequency of 10.76 kHz and 21.52 kHz ultrasonic frequency, the overall level of 112.32 dB

acoustic intensity), there is total destruction of microorganisms in water [4,5].

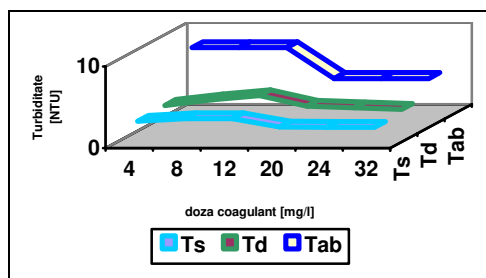
## 5. Evaluation of synergistic effect of the raw water sonic treatment

Suspension and the any type of impurities that may interact chemically are those which count in the calculation that underlies the decanters efficiency. Both water used in industrial processes and for drinking should have the turbidity, as small as possible, depending on the decantation level.

Based on measurements made at the experimental stand with a sonic decanter, decant water turbidity was determined at different doses of coagulant sulfate aluminum 4 mg/L (10%), 8 mg/L (20%), 12 mg/L (30%), 20 mg/L, (50%), 24 mg/L, (60%), 32 mg/L (80%).

As shown in Fig. 3, the lowest turbidity values are obtained for sonic treatment, water turbidity increasing with dose escalation to 10 mg/L (in solution: 50 mL/L) coagulant, then decreasing to 20 mg/L (in solution: 100 mL/L), after which the dose does not influence turbidity any more.

As shown in Figure 3 and Table 1 the lowest dose at which the control turbidity coincides with the sample turbidity is 0.2 mL/L of aluminum sulphate solution.



**Fig. 2.** Turbidity variation depending on the dose of aluminum sulphate:  $T_s$  - turbidity at sonic treatment;  $T_d$  - turbidity to classic decanter;  $T_{ab}$  - raw water turbidity;  $D$  - dose of aluminum sulphate.

**Table 1.** Variation of average turbidity values (control and working) depending on dose values of coagulant solution (aluminum sulphate)

Indicators	Coagulant dose solution	Average turbidity value - working	Average turbidity value - martor
	[mL/L]	[NTU]	
Values	5	15.1	4.2
	4	14	4.1
	3	12	3.8
	2	6.4	4
	1	5.9	4
	0.8	6.1	3.9
	0.6	7.4	3.8
	0.4	5.9	4
	0.2	3.9	4
	0.1	5.2	3.9

Analysis of synergetic effect of sonic treatment on coagulant dosage was revealed by reducing the dose of coagulant required in the water treatment process. Based on experiments made in the sonic decanters with different doses of coagulant effective results were obtained for dose reduction with 50% aluminum sulfate and aluminum polihydroxiclorure dose with 40%.

## 6. Technical and economic efficiency system of the sonic raw water treatment

In water treatment plants for drinking water it is used during decanter, decanters batteries, in most cases of an even number of decanters, minimum 2 (double). We believe that the experimental sonic decanter is part of a battery of 4 such decanters required for treatment plants that supply a city (or a

territorial administrative unit) of more than 10,000 inhabitants.

The price of a cubic meter of raw water (water of the Danube) purchased from "Apele Romane" National Company is considered to cost € 0.0148. The price for a cubic meter of drinking water in Braila, for the analyzed period, is 0.788 €.

The data presented in Table 2 show that the more we approach the area of the Danube flowing mouth into the Black Sea the more the price of drinking water from this source increases.

Implicitly, the closer the Danube approaches the flowing mouth, the more loaded it is and machining process requires additional costs, which are reflected in increasing doses of chemicals used: coagulants (aluminum sulfate, aluminum polyhidroxiclorure, polyelectrolytes) and disinfectants (chlorine).

**Table 2.** Price of a cubic meter of drinking water (obtained by treating raw water from river water) in different Danube areas

Zone	Giurgiu	Alexandria	Craiova	Calarasi	Braila	Tulcea
Price, lei/m <sup>3</sup>	2.74	2.75	3.062	3.137	3.31	3.844

For waters from deep sources, the expenses with greatly reduced the use of chemicals decrease very much even below 10%, but increase on additional equipment to remove sand and various metals existing in deep water.

To treat raw water during the settling stage, aluminum sulfate (the treatment plant in Braila), aluminum polyhidroxiclorure (treatment plants in Chiscani and Gropeni) are used as coagulants, and one polyelectrolyte coagulation as an adjuvant.

To establish the effectiveness of modern methods of treating raw water with ultrasonic waves two specific situations are taken into consideration in which the type of decanters is different:

- sonic decanter using the bi-frequential gas-dynamic generator;
- classic decanter, where the aluminum sulfate is used as coagulant, and polyelectrolyte (polyacrylamide anionic) as an adjuvant.

Profit is calculated by taking into account certain formulas in the economic sphere, as follows:

$$\text{Price-sales function: } p_{(x)} = a - b \cdot x$$

$$\text{Income function: } R_{(x)} = p_{(x)} \cdot x = (a - b \cdot x) \cdot x$$

$p_{(x)}$  = price according to quantity;  $x$  = amount;  $R_{(x)}$  = profit.

$$\text{Profit function: } \pi = R_{(x)} - C_{(x)} = (p \cdot x) - C_{(x)} = (p \cdot x) - (AVC \cdot x) - F$$

where:  $\pi$  = profit;  $p_{(x)}$  = price according to quantity;  $x$  = quantity;  $AVC$  = average variable costs;  $MC$  = marginal cost;  $F$  = total fixed costs

$$\frac{\partial R}{\partial x_i} = p_i \left( 1 - \frac{1}{|\eta_{xip}|} \right) \quad (1)$$

where:  $\eta_{xip}$  is the price elasticity.

In case of threshold, there are 2 situations:

a) the costs are covered (breakeven point):

$$\pi = R - C = 0$$

b) critical amount of income (breakeven

$$\text{quantity): } x = \frac{C_f}{p - c_v}$$

where:  $x$  = quantity;  $c_v$  = cost per piece, variable;  $C_f$  = fixed costs total;  $p$  = price per piece ( $x$ ).

Cost is calculated using the formula [120]:

$$C_{uf} = \frac{\sum_{i=1}^m C_{hi}}{Q_j} \quad (2)$$

where:  $C_{uf}$  = total unit cost;  $C_h$  = finished production expenses;  $Q$  = quantity of finished products;  $i$  = item calculation;  $j$  = object calculation.

To calculate the effective efficiency of the sonic decanter plant, it is following are considered:  $V_a$  - volume of water decanted within an hour, m<sup>3</sup>;  $n_d$  - number of decantation units;  $n_g$  - number of sonic generators;  $\tau$  - time of turbocharger operations, min;  $n_t$  - number of operation of the turbocharger in an hour;  $t_o$  - time necessary to 1 m<sup>3</sup> of water decantation in the sonic decanter, h;  $P_t$  - acting electric power turbocharger;  $C_e$  - the cost of electricity, Euro/kW·h;



$C_{CG}$  - the cost of coagulant (aluminum sulfate), lei/kg;  
 $C_p$  - coagulation adjuvant (polyelectrolyte) cost, lei/kg;  $C_{Cl}$  - disinfectant (chlorine) cost, lei/kg;  $C_g$  - sonic generator cost, Euro/pc;  $C_{aCl}$  - chlorination unit cost, USD/pcs;  $C_x$  - general expresses sonic treatment of raw water, lei;  $d_x$  - the optimum dose of coagulant for sonic decanter, mg/L;  $d_c$  - average dose of coagulant used in a classic decanter, mg/L;  $M_x$  - decanted mass coagulant in sonic decanter, kg;  $M_c$  - coagulant mass used in classic decanter, kg;  $M_p$  - polyelectrolyte mass (coagulation adjuvant - flocculation) used in classic decanter, kg.

1. The calculation begins by determining electricity consumption ( $W_0$ ) necessary to sonic decantation of water within one hour:

$$W_0 = P_t \cdot \frac{t_0}{\tau \cdot n_1}, \text{ kW} \quad (3)$$

where:  $P_t = 3\text{ kW}$ ;  $\tau = 5\text{ min}$ ;  $n_1 = 3$ ,  $t_0 = 1\text{ h} = 60\text{ min}$ .

Results:  $W_0 = 0.75\text{ kW}$ .

2. Electricity costs for sonic decanters of  $1\text{ m}^3$  of fresh water which decants within 1 h is:

$$C_0 = C_e \cdot W_0 \cdot t_0 = 0.0107\text{ €}, \quad (4)$$

where:  $C_e = 0.014\text{ €/kW}\cdot\text{h}$ ;  $W_0 = 0.75\text{ kW}$ ;  $t_0 = 1\text{ h}$ .

3. Sonic electric energy cost of raw water settling in the 4 units dams, within 1 h is:

$$C_4 = C_0, \text{ €} \quad (5)$$

where  $C_0 = 0.0107\text{ €}$ .

4. Amount of coagulant (aluminum sulfate) used in the process of sonic decanters of  $1\text{ m}^3$  of fresh water is

$$M_x = d_x / 1000 = 0,02\text{ kg}, \quad (6)$$

where  $d_x = d_c / 2 = 20\text{ mg/L}$ .

5. Amount of coagulant (aluminum sulfate) used in the raw water pond SOIC within 1 h is:

$$M_{4x} = 4 \cdot M_x, \text{ kg} \quad (7)$$

where:  $M_x = 0.02\text{ kg}$ .

6. Daily expenses for settling sonic raw water from the treatment plant (4 units tailings) are:

$$C_z = (M_{4x} \cdot C_{CG} + C_4) \cdot 24 = 0.6035\text{ €} \quad (8)$$

where:  $M_{4x}$  is  $0.08\text{ kg}$  and the  $C_{CG}$  is  $0.3\text{ €/kg}$ .

7. General annual expenses for sonic raw water decanter under the above conditions are:

$$C_z = (M_{4x} \cdot C_{CG} + C_4) \cdot 24 = 0.6035\text{ €} \quad (9)$$

where:  $C_z = 0.6035\text{ €}$ ;  $C_g = 100\text{ €/pc}$ .

8. Annual profit obtained by sonic treatment of raw water in comparison with a classic treatment, as a treatment stand:

$$P_f = \{[(M_c \cdot C_{CG} + M_{Cl} \cdot C_{Cl}) \cdot 4 \cdot 24] \cdot 365 + M_p \cdot C_p + C_{aCl} \cdot 1\text{ buc.}\} - C_x, \text{ €} \quad (10)$$

or  $P_f = C_{gen} - C_x = 355.24\text{ €}$

where:  $M_c = 0.04\text{ kg}$ ;  $C_{CG} = 0.3\text{ €/kg}$ ;

$M_{Cl} = 0.00416\text{ kg}$ ;  $C_{Cl} = 0.388\text{ €/kg}$

$M_p = 10\text{ kg}$  (mean consumed in a year);

$C_p = 3.214\text{ €/kg}$

$C_{aCl} = 476.2\text{ € / pcs}$  (average market)

$C_x = 620.3\text{ €}$

$C_{gen} = 975.53\text{ €}$  (annual costs for treating raw water classic).

9. Sonic decantation efficiency (annual) in comparison with traditional decanting within the treatment stand is:

$$E_f = 100 - \frac{C_{gen}}{P_f} \cdot 100 = 36.415\%, \quad (11)$$

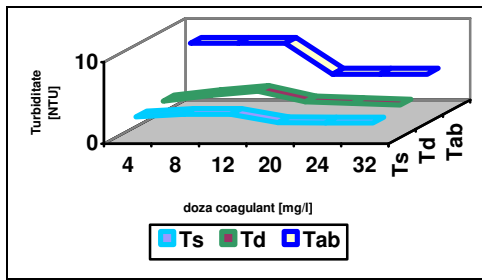
where:  $P_f = 355.24\text{ €}$ .

The cost of water treatment by the classic method is 2.67% from the water cost (ie € 0.02 from 0.788 € - price for  $1\text{ m}^3$  drinking water in Braila) due to sonic decantation efficiency ( $E_f = 36.415\%$ ) the cost of water treatment by the sonic method represents 0.67% of the drinking water and the price obtained will be  $0.772\text{ € / m}^3$ .

## 7. Conclusions

We determined the ratio between the period of the generator operation and the break period = 5min/15 min, set in an operating cycle of one hour at which the average turbidity value = 2.56 NTU being of the  $T_x$  and is lower than that obtained in the classic decanter (value between 4.2 and 4.8 NTU), which proves that the sonic decanter is 36.415% more effective compared with a traditional decanter.

The analysis of the synergetic effects of sonic treatment on coagulant dosage was revealed by reducing the dose of coagulant required in the water treatment process. Based on experiments made on the same decanter with different doses of coagulant, effective results were obtained for dose reduction the (by 50% aluminum sulfate and by 40% aluminum polyhidroxyclorure).



**Fig. 2.** Turbidity variation depending on the dose of aluminum sulphate:  $T_s$  - haze at sonic treatment,  $T_d$  - turbidity to settle fever;  $T_{ab}$  - raw water turbidity,  $D$ -dose of aluminum sulphate

**Table 1.** Variation of average values of turbidity (control and working) solution function coagulant dose values (aluminum sulphate)

Indicators	Coagulant solution dose	Average value of working turbidity	Average value of reference turbidity
	[ml/l]	[NTU]	
Values	5	15.1	4.2
	4	14	4.1
	3	12	3.8
	2	6.4	4
	1	5.9	4
	0.8	6.1	3.9
	0.6	7.4	3.8
	0.4	5.9	4
	0.2	3.9	4
	0.1	5.2	3.9

In the final price of water distribution to users, water treatment represents a very small percentage (less than 3%), but in the case of the sonic water treatment it becomes lower than 1%, which shows the efficiency and profitability of this new raw water treatment technology for obtaining drinking water compared to the conventional technology.

### References

[1]. **Stingaciu, E., Simionescu, C., M.** - *Supravegherea și controlul calității apelor naturale*, Ed. Matrix Rom, București, (2009).  
 [2]. **Cîrnu C., Bălan G., Dumitraș P.** - Decantorul sonic pentru tratarea apei brute în vederea potabilizării, *Revista Meridian Ingineresc*, nr. 1/2011, Editura UTM, Chisinau, Republica Moldova, pag. 14-19  
 [3]. **Cuciuc T., Cîrnu C., Balan G.** - Computing of the Levasseur type air- jet flat generator with two resonators, *Revue Roumaine de*

*Science Tech., Mécanique Appl.*, Tome 56, N<sup>o</sup>1, Bucharest, (2011).  
 [4]. **Cîrnu C., Bălan G., Dumitraș P.** - *Oxydability, aluminium and sulphates at the raw water sonic regime treatment*, *Revista Meridian Ingineresc*, nr. 4/2010, Editura UTM, Chisinau, Republica Moldova, pag. 88-92.  
 [5]. **Cîrnu C., Ștefan A., Bălan G.** - *Sonomicrobiology of raw water at the treatment by air-jet generators*, The 9<sup>th</sup> International Conference "Constructive and Technological Design Optimization in the Machines Building Field" OPROTEH-2011, Bacău, 24-26 May, (2011), (în curs de publicare).  
 [6]. **Cîrnu C., Ștefan A., Bălan G.** - *Acoustic parameters of the flat air-jet generator with two swirl resonators*, The annual symposium of the institute of solid mechanics SISOM 2011 and Session of the Commission of Acoustics, Bucharest, 25-26 May, (2011), pg. 216-222.  
 [7]. **Bălan G., Ciurea A., Bordei M., Balan V.** - *The Sonic Technologies*, Quatrieme edition du Colloque Francophone en Energie, Environnement, Economie et Thermodynamique COFRET'08, 11 – 13 June 2008, Nantes - France , pp. 17-25  
 [8]. **Ebbeken, K., Possler, L., Ristea, M.** - *Calculația și managementul costurilor*, Ed. Teora, București, (2000).





## COMPARISON OF THE EFFICIENCY OF THREE TYPES OF SOLAR COLLECTORS

**Catalin Bogdan MOCANU, Tanase PANAIT,  
Alexandrina TEODORU, Daniela TASMA**

"Dunarea de Jos" University of Galati  
email: Catalin.Mocanu@ugal.ro

### ABSTRACT

*Solar energy is one of the most abundant resources energy available in the world. Solar collectors have evolved in the last decades, but still they haven't reached very high efficiencies.*

*The collector efficiency is dependent on the temperature of the plate which in turn is dependent on the nature of the fluid flow inside tube, solar isolation, ambient temperature and top loss coefficient, the emissivity of the plate and glass cover. This paper presents the test results of three different solar collectors and compares their efficiency.*

KEYWORDS: heat transfer, solar collector, solar energy, system efficiency, thermal performance

### 1. Introduction

Solar energy is one of the most available, cleanest and cheapest energy of all sources on the surface in the world.

Because of that and of the global shortage of fossil energy source and environmental pollution, it became increasingly favorable.

Scientists ask themselves how we can get hold of solar energy such that it can be stored and transported from the sun and the uninhabited region of the earth's sunbelt to the world's industrialized and populated zones.

This question has motivated them to find methods to capture solar energy even if it happens to be a cloudy or rainy day, good enough reason for increasing its potential utilization.

Recently they have found a method [2] who converts solar energy into solar fuels. In what follows, we will analyze several types of solar collectors producing heat.

### 2. Models of collectors

#### 2.1. Collectors without concentration of solar radiation

A **flat-plate collector** is shown in Fig. 1. When solar radiation passes through a transparent cover and impinges on the blackened absorber surface of a high absorptive, a large portion of this energy is absorbed by the plate and then transferred to the transport medium in the fluid tubes to be carried away for storage or use.

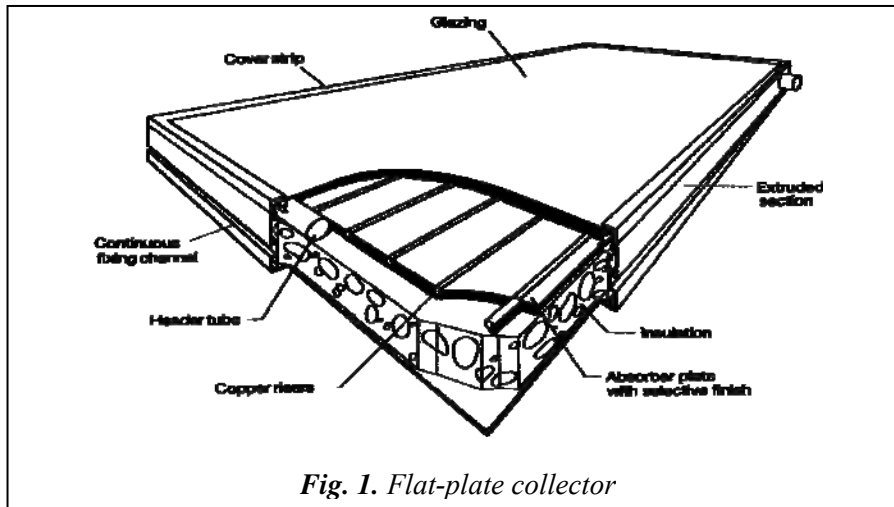
*Glazing:* one or more sheets of glass or other diathermanous (radiation-transmitting) material. Tubes, fins, or passages: helping to conduct or direct the heat transfer fluid from the inlet to the outlet.

*Absorber plates:* flat, corrugated, or grooved plates, to which the tubes, fins, or passages are attached. The plate may be integral with the tubes.

*Headers or manifolds:* to admit and discharge the fluid.

*Insulation:* to minimize the heat loss from the back and sides of the collector.

*Container or casing:* to surround the aforementioned components and keep them free from dust, moisture.



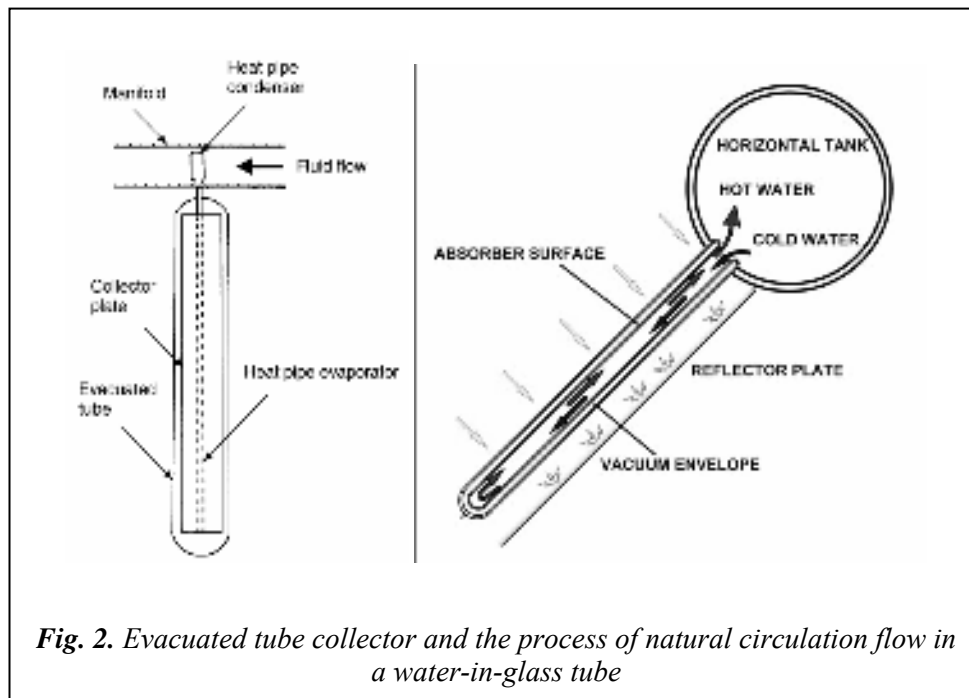
*Fig. 1. Flat-plate collector*

The evacuated tube collector (Fig.2) uses liquid–vapors phase change materials to transfer heat at high efficiency. These collector works by converting energy into tubes.

They have a heat pipe (a highly efficient thermal conductor) placed inside a vacuum-sealed

tube. The pipe is made of copper, contains a small amount of fluid (e.g. methanol). The vacuum envelope reduces convection and conduction losses, so the collectors can operate at higher temperatures.

These types of collectors can reach higher values of temperature than flat-plate collectors.

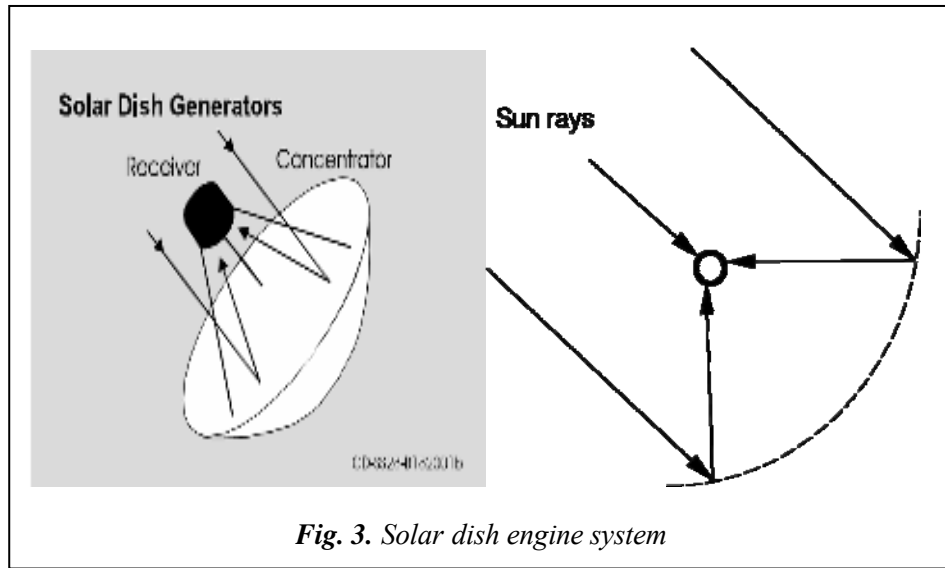


*Fig. 2. Evacuated tube collector and the process of natural circulation flow in a water-in-glass tube*

## 2.2. Collectors with concentration solar radiation

**Dish/Engine** systems use an array of parabolic

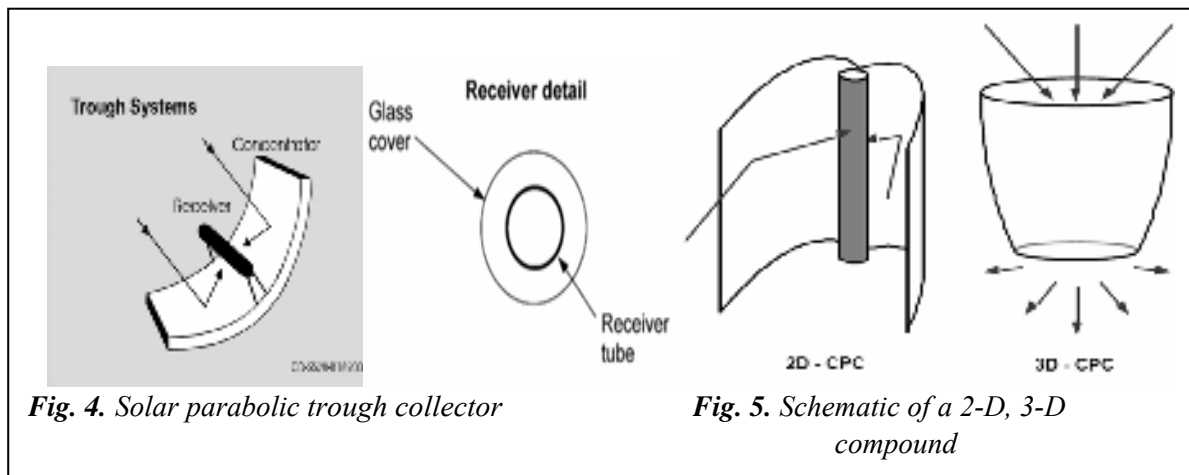
dish-shaped mirrors (stretched membrane or flat glass facets) to focus solar energy onto a receiver located at the focal point of the dish (Fig. 3). The fluid in the receiver is heated to 750°C (1,382°F).



**Fig. 3.** Solar dish engine system

Collector Parabolic Trough systems use parabolic trough-shaped mirrors to focus sunlight on thermally efficient receiver tubes that contain a heat

transfer fluid (Fig. 4). This fluid is heated to 390°C (734°F) and pumped through a series of heat exchangers to produce superheated steam.



**Fig. 4.** Solar parabolic trough collector

**Fig. 5.** Schematic of a 2-D, 3-D compound

These types of collector have reflective inner walls that are used to augment the solar flux concentration of the primary concentrator.

Higher concentration ratio imply lower heat losses from smaller receiver, and consequently, higher attainable temperatures on the receiver.

The power flux concentration can be increased by a factor  $\rho (\sin\Phi_{rim})^{-1}$  for 2-D CPC and  $\rho (\sin\Phi_{rim})^{-2}$  for 3-D, where  $\Phi_{rim}$  is the angle of the primary concentration system and  $\rho$  is the inner wall total hemispherical reflectance of the CPC.

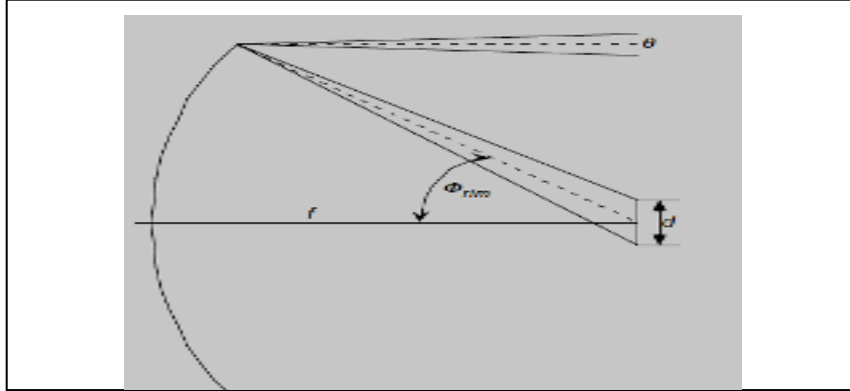
### 3. Principles of solar energy concentration

This conventional method, of parabolic-shaped mirrors, presupposes collecting solar energy from a large area and delivering it onto a small one. A parabola focuses rays parallel to its axis into focal point. The angle focusing on extremities is approximated at  $\theta=0.0093$  radian. It considers that the focal length  $f$  is perfectly positioned and the rim angle  $\Phi_{rim}$  is aligned to the sun, and the reflection of the rays at the focal plane forms a circular image centered at the focal point (Fig. 6).

The diameter is:

$$d = \frac{f \cdot \theta}{\cos \theta_{rim} (1 - \cos \theta_{rim})} \quad (1)$$

When the dish is aligned toward the sun, the reflection of the sun rays at the focal plane forms a circular image centered at the focus of diameter  $d$ .



**Fig. 6.** Concentration of sunlight by a parabolic dish of focal length  $f$  and rim angle  $\Phi_{rim}$

On this circle, the radiation flux intensity is maximum and uniform in the paraxial solar image (the "hot spot"). It decreases for diameters larger than  $f \cdot \theta$  as a result of forming elliptical images. The theoretical concentration ratio  $C$  at the hot spot is defined as the ratio of the radiation intensity on the hot spot to the normal beam insolation, where  $C$  - solar flux concentration ratio,  $\theta$  - angle subtended by the sun at the earth's surface.

$$C \approx \frac{4}{\theta^2} \sin^2 \phi_{rim} \quad (2)$$

For a rim angle of  $45^\circ$  the theoretical peak-concentration ratio exceeds 23,000 suns, where 1 sun refers to the normal beam insolation of  $1\text{kW/m}^2$ . The thermodynamic limit for solar concentration is given by the factor  $\sin^{-2} \phi \approx 46,000$  suns.

#### 4. The efficiency of solar collectors

The table below presents the performances of different types of solar collectors described above [5].

**Table 1.** Solar energy collector

Motion	Collector type	Absorber type	Concentration ratio	Indicative temperature range (°C)
Stationary	Flat plate collector (FPC)	Flat	1	30-80
	Evacuated tube collector (ETC)	Flat	1	50-200
Single-axis tracking	Linear Fresnel reflector (LFR)	Tubular	10-40	60-250
	Parabolic trough collector (PTC)	Tubular	15-45	60-300
Two-axes tracking	Parabolic dish reflector (PDR)	Point	100-1000	100-500

The efficiency of a solar collector is shown below:

$$\eta = F_t \left[ (D \cdot A) - \frac{K(T_i - T_a)}{E \cdot k} \right], \% \quad (3)$$

where:  $F_t$  - is heat transmission factor,  $D \cdot A$  - transmission-absorption product for incidence angle,  $K$  - overall heat loss coefficient,  $T_i$  - fluid inlet temperature,  $T_a$  - ambient temperature,  $E$  - solar radiation on a horizontal surface,  $k$  - collector concentration ratio.

The absorption coefficient must be larger and the transmission coefficient must be smaller.

The heat transmission factor represents real useful heat which might be obtained in the collector if the absorbing medium would have the fluid inlet temperature.

This is:

$$F_t = \frac{m \cdot c_p (T_e - T_i)}{A_c [E_a - k(T_i - T_a)]} \quad (4)$$

where:  $m$  - mass flow working fluid;

$c_p$  - specific heat;  $A_c$  - heat exchanger surface area;  $E_a$  - solar radiation absorbed.



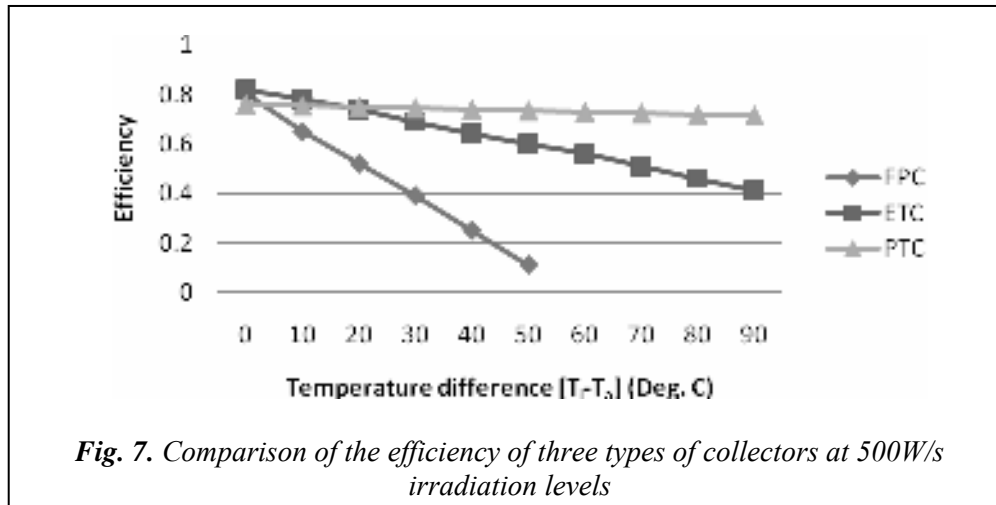


Fig. 7. Comparison of the efficiency of three types of collectors at 500W/s irradiation levels

The table presents the efficiency of flat-plate collector, evacuated tub collector and parabolic trough collector.

As seen in Figure 7, the better efficiency and the higher performance have been observed for vacuum tube collectors and parabolic trough collectors and retain high efficiency even at higher collector inlet temperatures.

## 5. Conclusion

The paper compares several of the most common types of collectors. The various types of collectors described include flat-plate, evacuated tub collector, dish engine and parabolic trough.

The thermal analysis method of collectors is presented to evaluate their performances.

The application areas described in the paper show that solar energy collectors can be used in a different places where are not fully developed, could provide financial benefits, and can be used whenever possible and in terms of environmental protection.

## Acknowledgements

The work of this paper was supported by Project SOP HRD - SIMBAD 6853, 1.5/S/15 - 01.10.2008 and Project SOP HRD – EFICIENT 61445/2009.

## References

- [1]. Aldo Steinfeld, Robert Palumbo. - *Solar Thermochemical Process Technology*, R. A. Meyers Ed., Academic Press, Vol. 15, pages 237-256, (2001).
- [2]. Iuliana Burda, Constantin Neaga - *Analiza eficientei termice a unor tipuri constructive de captatoare solare destinate incalzirii apei*. Universitatea Politehnica Bucuresti 25 June, (2010).
- [3]. Rakesh Kumar, Marc A. Rosen - *Integrated collector-storage solar water heater with extended storage unit*. Applied Thermal Engineering, Volume 31, Issues 2-3, February, (2011), Pages 348-354.
- [4]. \*\*\* - *Solar Energy Potential on the U.S. Continental Shelf* <http://ocsenergy.anl.gov>, (2006).
- [5]. Soteris A. Kalogirou - *Solar thermal collectors and applications*. Department of Mechanical Engineering, Higher Technical Institute, P.O. Box 20423, Nicosia 2152, Cyprus Received 18 June 2003; accepted 10 February, (2004).
- [6]. Xu Xinjian, Yang Lei, Zhang Xiaosong and Peng Donggen - *Review on the development of flat-plate solar collector and its building-integrated designing*. School of Energy & Environment Southeast University Nanjing, 210096, China rachpe@seu.edu.cn.

## INCREASE OF BOF CONVERTER LIFE BY OWN SLAG COATING

**Viorel MUNTEANU<sup>1</sup>, Viorel DRAGAN<sup>1</sup>, Dan ZORLESCU<sup>2</sup>**

<sup>1</sup>"Dunarea de Jos" University of Galati, <sup>2</sup>Arcelor Mittal Galati  
email: [munteanu\\_viorel48@yahoo.com](mailto:munteanu_viorel48@yahoo.com)

### ABSTRACT

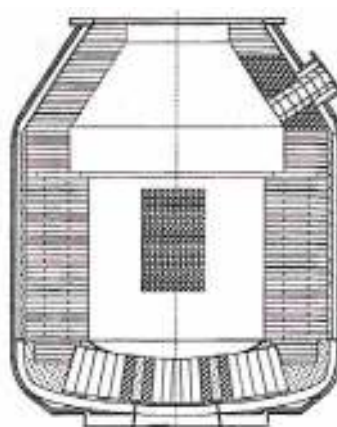
*This paper presents a method for the improvement of the lining life of the BOF converter by slag coating, under nitrogen pressure. Own slag coating of converter lining is put in practice after steel tapping. Dolomite blocks are used like standard wear converter lining. Nitrogen blowing for own slag coating is carried out by oxygen lance. After steel tapping without slag, the converter is tilt in blowing position and the oxygen lance is let down in the lowest position. The nitrogen is blown under 10-12 barr pressure and 450-500 Nm<sup>3</sup>/min rate, for 3 minutes. By this slag coating technology the performance of refractories has been improved from about 370 heats per campaign in reference year to about 800 heats per campaign at the end of two years of experiments, and therefore refractory consumption decreased from 5.25 kg/t under 3.00 kg/t and the cost of converter refractories decreased by 0.24 \$/t. Another variant for improvement of the BOF converter lining life was the use of magnesia bricks for selective lining areas (trunion rings area and charging mouth). The own slag coating technology has been used also. In the case of this variant, the lining life of converter has been improved to about 800 heats per campaign at the end of two years of experiments and so the refractories consumption decreased under 2.45 kg/t. Because of the higher price of magnesia bricks and of the lower price of dolomite blocks, the cost for converter refractories has decreased only by 0.02\$/t.*

**KEYWORDS:** BOF converter, refractories, lining life, magnesia bricks, dolomite blocks

### 1. Control system for own slag coating

There are only two ways in order to remain on the steel manufacture market: quality improvement and cost reduction. One of the ways for cost reduction is to increase the lining life of converters. The nitrogen blowing by oxygen lance in the lowest position, at a pressure of 4-16 barr and a rate of 450-500 Nm<sup>3</sup>/min. The converter lining sketch for dolomite variant and for magnesia bricks variant is shown in Fig. 1. As it can be seen, magnesia bricks have been used for selective lining areas only (trunion rings area and charging mouth). The control system for own slag converter coating is shown in Fig 2.

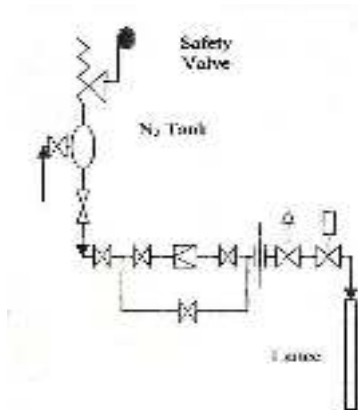
The chemical composition of the converter slag at tapping is presented in Table 1.



**Fig.1.** Converter lining sketch

**Table 1.** Chemical composition of converter slag, [%]

CaO	SiO	MgO	Al <sub>2</sub> O <sub>3</sub>	MnO	P <sub>2</sub> O <sub>5</sub>	Fe
53-55	14-16	1.5-1.8	0.4-0.6	5.3-5.7	2.1-2.4	17.1-17.7



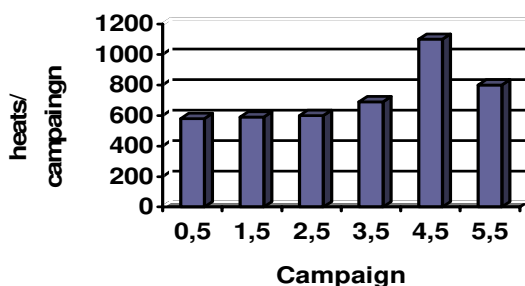
**Fig. 2.** Control system for nitrogen blowing

After the steel from the converter and the using of slag free tapping system, the converter is tilt in blowing position and the oxygen lance is let down in the lowest position. Then the quickly closing valve for nitrogen is shut of and the lance valve also. The nitrogen is blowing for 3-4 min under 10-12 barr pressure and 450-500 Nm<sup>3</sup>/min rates.

So the slag is spreading in radial and vertical direction onto the vessel refractories by the nitrogen spurts that come out from the nozzle of lance. The nitrogen has no negative reaction with slag and the lining of converter.

During cooling process the dreading slag is flowing on the converter lining. In this process the slag is "frozen" on the most used lining areas that are the coolest ones. So the coating of converter lining is obtained for the next heat.

After the first tests of own slag coating technology, the using cycle of nitrogen blowing was stabilized (Table 2).



**Fig. 3.** Evolution of lining life (heat/campaign) for converter no. 1 – first year

**Table 2.** Cycle of nitrogen blowing for own slag coating

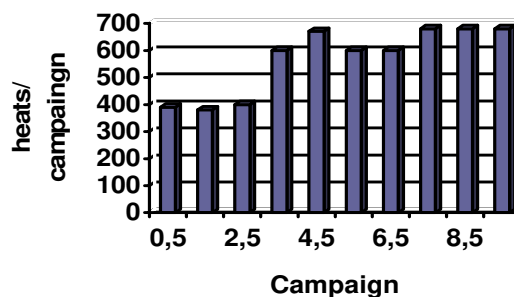
Stage converter campaign [heats]	Nitrogen blowing regime
1-50	Without nitrogen blowing
50-150	One nitrogen blowing/24h
150-300	One nitrogen blowing/8h
After 300	One nitrogen blowing/3h

The own slag coating technology has the following advantages:

- decreasing of the gunning masses;
- increasing of the lining life;
- decrease of the perforating risk for cylindrical area of the vessel.

## 2. The technological results of own slag coating technology

Figures 3, 4 and 5 present the results of the lining life (number of heats/campaign) for the three converters. As it can be seen, by slag coating technology, the lining life has increased from about 370 heats at the beginning to about 800 heats at the end of the experiments. The average values of the lining life for every converter and for the steelmaking shop are presented in Fig 6. The average increasing of the lining life in the first two years of own slag coating technology was about 160 heats/years (from 370 to 668 – Table 3). These average lining life values are used in the steelmaking shop for the economic estimation of the improvement of slag coating technology.



**Fig. 4.** Evolution of lining life (heat/campaign) for converter no. 1 – second year

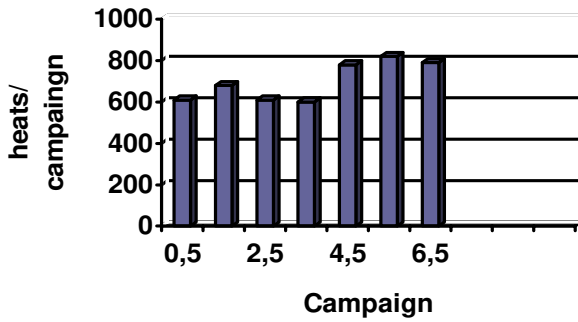


Fig. 5. Evolution of lining life (heat/campaign) for converter no.2 – first year

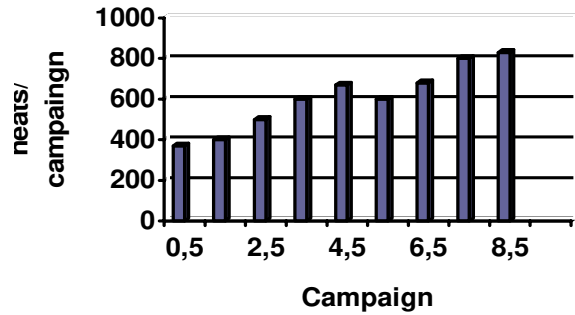


Fig. 6. Evolution of lining life (heat/campaign) for converter no.2 – second year

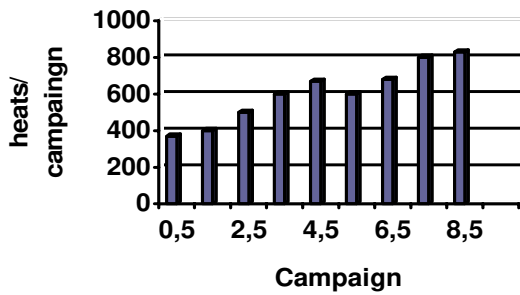


Fig. 7. Evolution of lining life (heat/campaign) for converter no.3 – first year

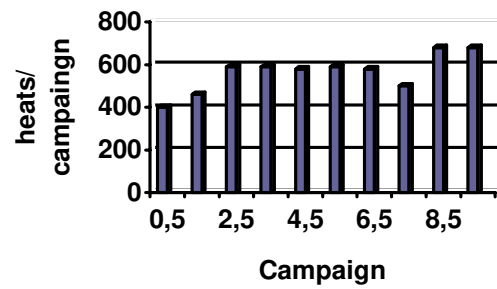


Fig. 8. Evolution of lining life (heat/campaign) for converter no.3 – second year

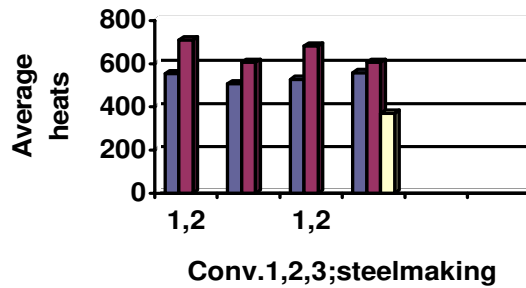


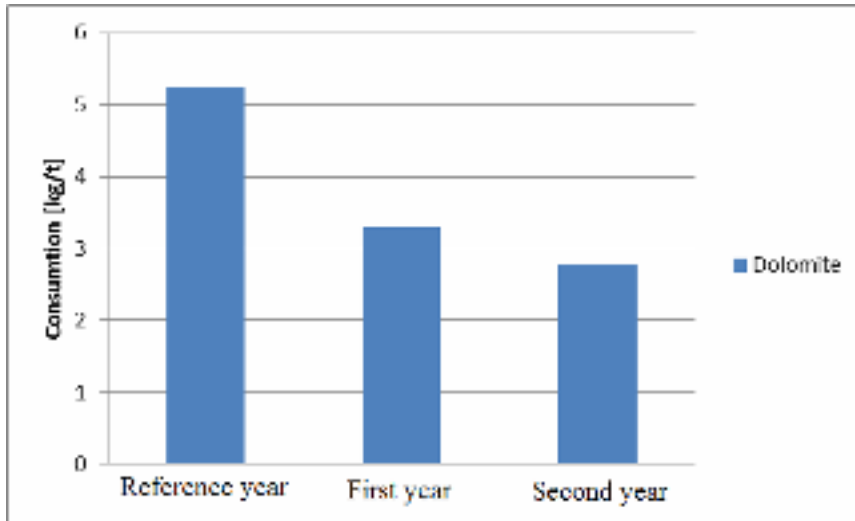
Fig. 9. Evolution of average lining life (heat/campaign)

1 – the first year of experiments; 2 – the second year of experiments;  
 3 – reference year

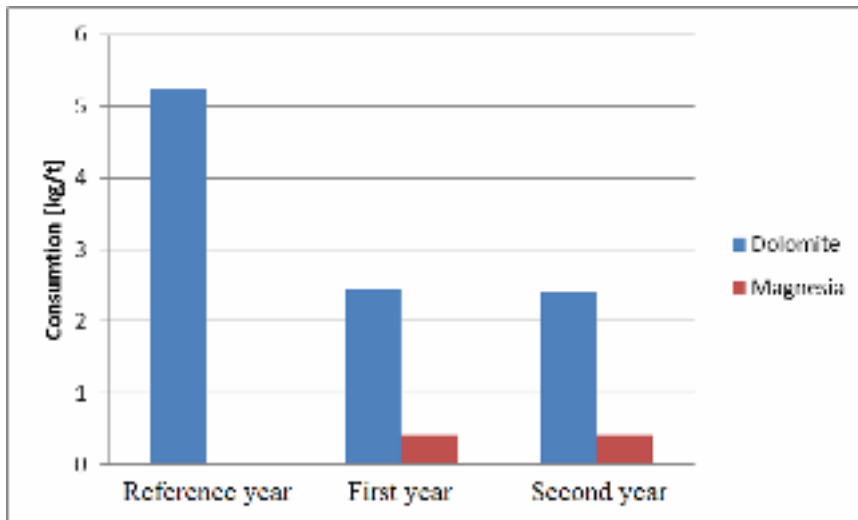
Table 3. Evolution of average lining life (heat/campaign)

	Conv. 1	Conv. 2	Conv. 3	Steelmaking
Reference year				370
The first year	554	597	528	560
The second year	715	606	682	668

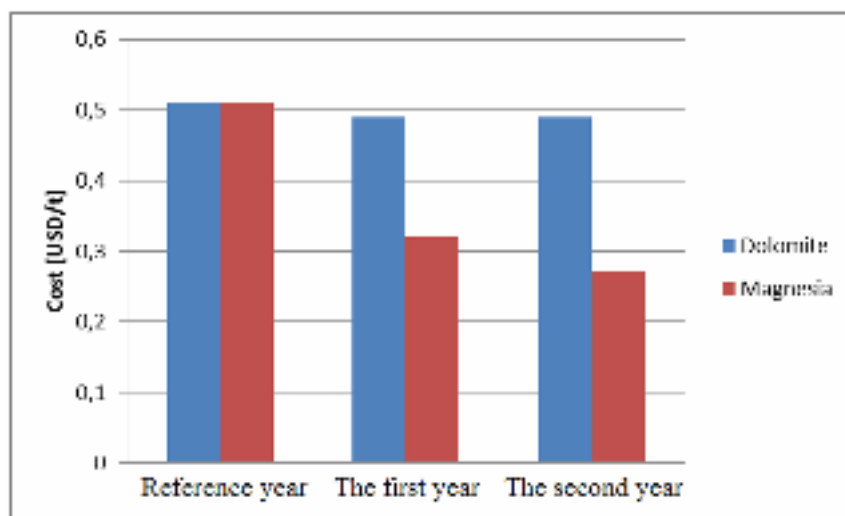




*Fig. 10. Dolomite consumption (dolomite variant)*



*Fig. 11. Dolomite and magnesia consumption (selective lining areas variant)*



*Fig. 12. Evolution of specific cost for refractories*



In the first and second years of experiments two types of lining were used: one of dolomite blocks only and another of magnesia bricks for selective lining areas (trunion rings area and charging mouth). So it was necessary to analyse the influence of the own slag coating technology on every type of lining. In figures 7 and 8 present the evolution of the dolomite and the magnesia specific consumptions relative to the reference year, when own slag coating technology was not used at all.

It can be observed that dolomite consumption decreased with 2.47kg/t for the dolomite blocks only variant and with 2.85kg/t for the magnesia bricks selective lining areas variant, but for this last variant there is a supplementary consumption of 0.42kg magnesia bricks/t.

From this reason it was necessary to analyse these two variants from an economic viewpoint.

### 3. The economical results

The refractories specific consumptions and costs have been used for economic calculations in the case of the two variants.

The results are presented in Table 4 and Fig. 10. It can be observed that, using the own slag coating technology, the specific cost of the refractories was diminished from 0.5\$/t liquid steel to 0.27\$/t for the dolomite blocks only variant.

That means a 0.24\$/t gross profit. In the case of the magnesia bricks selective lining areas variant, the profit is only 0.02 \$/t only.

These economical results have been determined by the very low cost of dolomite blocks and a the high cost of magnesia bricks. So, until now, the best variant is dolomite lining and own slag coating technology.

*Table 4. Specific cost of refractories, [\$/liquid steel, t]*

Year	Lining variant	
	Dolomite	Magnesia selective areas
reference	0.51	0.51
second	0.32	0.49
third	0.27	0.49

### 4. Conclusions

Using the slag coating technology the performance of the refractories has been improved.

The lining life of the converter has been improved from about 370 heats in reference year to about 800 heats per campaign at the end of the two years of experiments and therefore the dolomite refractories consumption decreased from 5.25kg/t under 3.00kg/t.

The cost for converter refractories decreased by 0.24\$/t.

### References

- [1]. C. Blanco, M. Diaz, E. Gorgia, M. Randules - *Analysis of kinetic date industrial steel converter for the operation control*, 5th EOSC, (2006), p.115-122.
- [2]. R. Boom, B. Deo - *Fundamentals of steelmaking metallurgy* Preston Hall International, (UK), Limited, (2003), p.189-191.
- [3]. C. Kattenbest, B. Roffel - *Hibrid Dynamic Modelling for Basic Oxygen Steelmaking in a LD Converter*, STELSIM, (2007) Graz/Seggan, p. 54-59.
- [4]. C. Mustata - *Tehnici moderne de conducere automata a proceselor siderurgice*, Ed. Tehnica Bucuresti, (2007).
- [5]. I. Butnariu - *Modelarea matematica a elaborarii otelului in convertizoare cu oxigen*, Ed. Tehnica Bucuresti, (2002).
- [6]. F. Veters - *Metallurgy of Steelmaking*, (1994), Verlag Stahleisen mbh, Dusseldorf.



## THERMAL DECOMPOSITION OF HAFNIUM ETHOXIDE- MOLECULAR PRECURSOR FOR HAFNIA DIELECTRIC THIN FILMS

Elena Emanuela VALCU (HERBEI)<sup>1</sup>, Viorica MUSAT<sup>1</sup>,  
Timothy LEEDHAM<sup>2</sup>

<sup>1</sup>“Dunărea de Jos” University of Galați, Centre of Nanostructures and Functional Materials, Romania,

<sup>2</sup>Multivalent Ltd. United Kingdoms

emails: [viorica.musat@ugal.ro](mailto:viorica.musat@ugal.ro), [tim.leedham@multivalent.co.uk](mailto:tim.leedham@multivalent.co.uk)

### ABSTRACT

*The HfO<sub>2</sub> thin-film is a very promising gate dielectric material for last generation transistors. The paper presents the thermal decomposition of hafnium ethoxide used as molecular precursor for obtaining hafnia thin films. The investigated molecular precursor is a mixture of Hf<sub>3</sub>O(OC<sub>2</sub>H<sub>5</sub>)<sub>10</sub> and Hf<sub>4</sub>O(OC<sub>2</sub>H<sub>5</sub>)<sub>14</sub> moisture sensitive amorphous powder.*

*The thermal decomposition of hafnium ethoxide precursor was investigated by TG-DTG-DSC analysis from room temperature to 600<sup>o</sup>C in nitrogen atmosphere at 5K/min. The composition of gas products resulted during pyrolytic decomposition has been studied by Fourier Transformation Infrared Spectroscopy (FTIR) and Mass Spectroscopy (MS). In the gas products, hydrogen, methyl, ethyl, vinyl, hydroxyl groups, acetic aldehyde and acetylene were identified. From mass spectroscopy and FTIR data results that the loss of ethoxy groups from the molecular precursor occurs in the decomposition steps between 200 and 375<sup>o</sup>C. That suggests that in different steps, ligands from different coordination spheres are lost.*

KEYWORDS: Hf-ethoxide, thermal behavior, dielectric thin films

### 1. Introduction

Hafnium dioxide (HfO<sub>2</sub>) is a high temperature refractory material with very good dielectric properties [1]. The stoichiometric hafnium oxide has stable monoclinic structure. Heated at temperatures higher than 1700<sup>o</sup>C, it transforms into the tetragonal structure. Further heating at about 2700<sup>o</sup>C allows the further transformation into the cubic polymorphic form having the fluorite structure. A wide range of applications of HfO<sub>2</sub> such high-k gate electronic devices based on TFT [2- 5] as well as near-UV laser AR, dielectric mirror designs and waveguide [6] require thin film material. HfO<sub>2</sub> thin films and coatings can be prepared by various methods, as atomic layer deposition [8–11], pulsed laser deposition [12–14], chemical vapor deposition [15–17], radio frequency sputtering [18–20], plasma oxidation of Hf film [21] and sol–gel routes [22–34].

For MOCVD the preferred precursors are Hf t-butoxide and Hf ethylmethylamide for reasons of volatility. The great interest for using sol-gel method

for preparation of films for multiple application fields is due to low fabrication costs with respect to other methods, advanced control of doping and the possibility of obtaining materials having a predetermined structure by modification of the elaboration parameters. The preparation of HfO<sub>2</sub> coatings by sol–gel method has been reported using different routes and precursors. Nishide *et al.* [22], Shimada *et al.* [23], Yu *et al.* [24], Shimizu *et al.* [25, 26] have prepared HfO<sub>2</sub> using HfCl<sub>4</sub> in ethanol as starting material. Takahashi and Nishide [27] and Nishide *et al.* [28] worked also with HfCl<sub>4</sub> but in water, hafnium hydroxide being an intermediate compound peptized with formic/oxalic acid. Blanc *et al.* [29] used the same Hf-source but in 1-methoxy 2-propanol. Aoki *et al.* [30] used Hf(OBut)<sub>4</sub> toluene/ethanol solution as a hafnium precursor. Goncalves *et al.* [31] used HfOCl<sub>2</sub> in ethanol as starting material. From the thermal decomposition of hafnium molecular precursors, nano size hafnium oxide or HfO<sub>2</sub>-polymer hybrid thin films, can be obtained at low temperatures. The sol–gel preparation

of HfO<sub>2</sub> thin films starting from Hf-ethoxide has been previously reported by several authors [6,33-34]. Villanueva-Ibanez *et al.* dissolved Hf(OC<sub>2</sub>H<sub>5</sub>)<sub>4</sub> in ethanol, in the presence of acetyl acetone [6]. Zaharescu *et al.* successfully prepared HfO<sub>2</sub> coatings on silicon wafer by sol-gel route from Hf-ethoxide, Hf-pentadionate and Hf-chloride precursors [34]. The films prepared from ethoxide and pentadionate precursors were homogenous and uniform with respect to their thickness before as well after crystallization. For this latter route, a nanoporosity was present in the quasiamorphous films as well in the crystallized ones. The molecular structure of Hf-oxo-ethoxide has been investigated by some authors [35], but the simple structure Hf(OEt)<sub>4</sub> has not been characterized.

In this paper we report the thermal behavior of hafnium ethoxide. A better understanding thermal behavior is very important to control the decomposition steps at different temperatures, and consequently the microstructure and properties of the obtained oxide films.

## 2. Experimental details

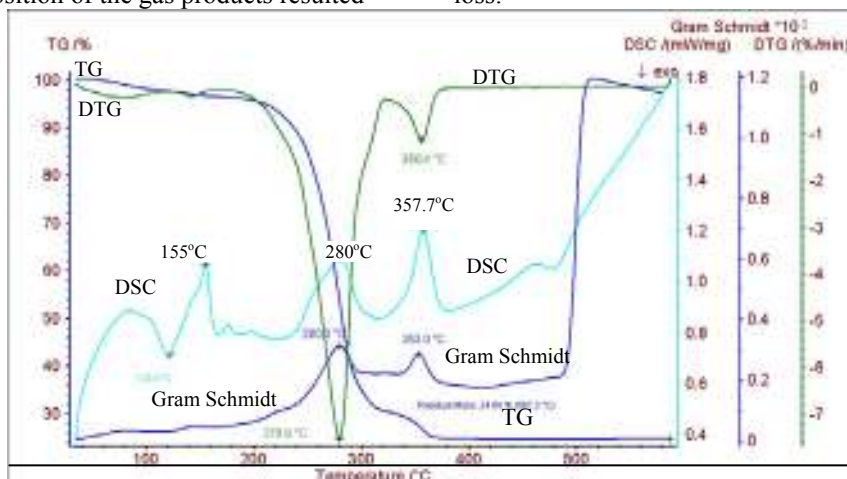
Hafnium ethoxide precursor was purchased from Multivalent Ltd. UK. The thermal analysis (about 10 mg samples weight) was carried out in dry nitrogen atmosphere using an Q5000 IR thermal analyses and a Q20 Differential Scanning Calorimeter, from Thermal Analysis Instruments, in a platinum crucible, at 5K/min rate up to 600°C. For the chemical composition of the gas products resulted

during thermal decomposition of hafnium ethoxide, simultaneous thermogravimetric (TG-DTG), differential scanning calorimetry (DSC), Fourier transformation infrared spectroscopy (FTIR) and mass spectrometry (MS) analysis were conducted, using a NETZSCH simultaneous thermal analysis instrument coupled with FT-IR spectrometer QMS 403C and FTIR Spectrometer Vertex 70.

## 3. Results

Figure 1 shows the results of simultaneous TG-DTG-DSC data for precursor decomposition and the Gram Schmidt mass spectrometry curve of gas products resulting during this decomposition. The very complex decomposition process of hafnium ethoxide with mass change up to 375°C can be observed, with at least four important endothermic peak accompanied by release of gaseous products. The thermal decomposition begins with small mass loss processes (about 5% on TG curve) at ~ 85 and 155°C characterized by endothermic effects (DSC curve), accompanied by two small peak for released gaseous substances (curve Gram Schmidt). Extensive decomposition occurs between 160° and 340°C (with weight loss of ~70%) and intense endothermic DSC peaks at 280 and 356°C. From the DTG curve, one can observe that the most intense process is between 225° and 325°C, were the alkoxide losses the major weight percent (~60% of the hole mass loss).

The decomposition ends with an endothermic DSC peak at 356°C, accompanied by 10% of mass loss.

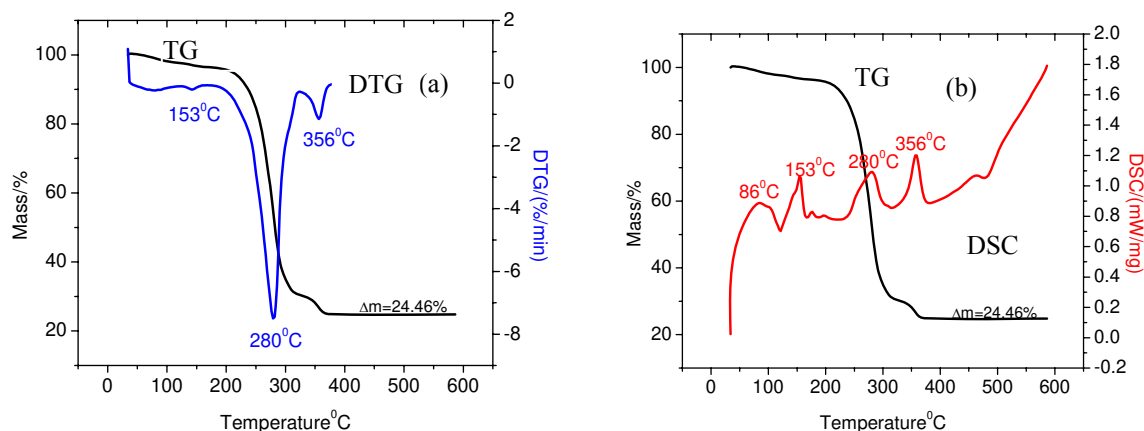


**Fig. 1.** Experimental results of experimental curves recorded simultaneously during TG-DTG-DSC-MS analysis of hafnium ethoxide in dried nitrogen.

Figure 2a reveals that the process with the highest mass loss and endothermic peak at 280°C is carried out with a much higher reaction rate (maximum rate of 7.5%/min) than the other decomposition steps. In the same time, Figure 2b

shows that for this process (step 3) the thermal effect relative to the amount of substance decomposed is much lower than for the others steps. This means that the intermediate compound that decomposed at 280°C is less stable than the compound resulting from its

decomposition and is less stable than the initial sample.

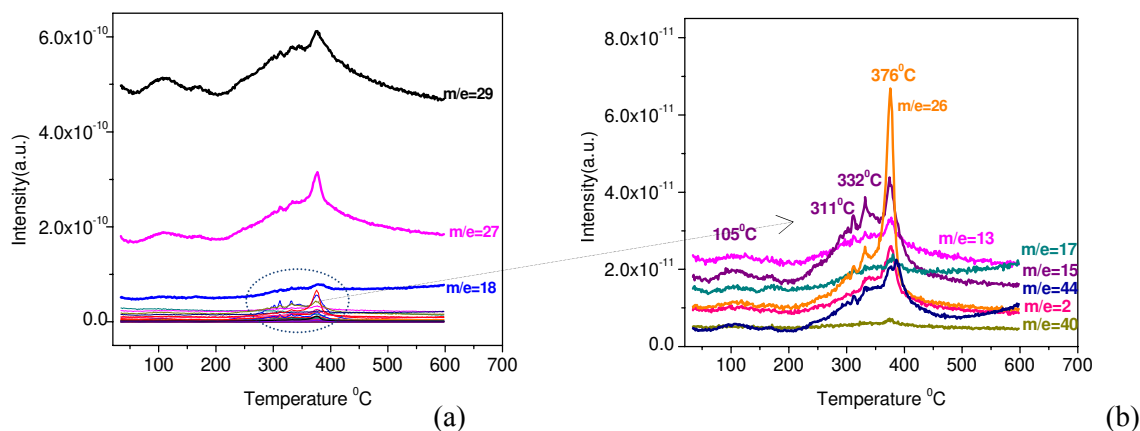


**Fig. 2.** TG -DTG curves (a) and (TG-DSC) curves (b)

In the range of room temperature (RT) to  $\sim 100^\circ\text{C}$ , an evaporation process (2% weight loss) is observed. From  $100^\circ$  to  $170^\circ\text{C}$  other mass loss process (4% weight loss) occurs, very probably, the evaporation of some adducts existing in the sample of two alkoxides mixture. Between  $170^\circ$  to  $375^\circ\text{C}$ , the hafnia ethoxide clusters decompose with the formation of hafnium oxide and the release of

different organics, as can be observed from the mass spectroscopy data (Fig. 3).

The gaseous products evolved during thermal decomposition were identified from mass spectroscopy (Fig. 3) and FTIR spectra (Fig. 4), such as: hydrogen, methyl, ethyl, vinyl, hydroxyl groups, acetic aldehyde and acetylene (Table 1).



**Fig. 3.** Mass spectra of gas products of thermal decomposition of hafnium ethoxide, main peaks (a) and enlargement of smaller peaks (b).

From FTIR spectra, one can conclude that, for the most important decomposition peaks (steps), the evolved gas correspond to the following chemical species: in the range of  $893 - 950\text{cm}^{-1}$  the banding vibration of  $=\text{C}-\text{H}$  and  $=\text{CH}_2$  (usually sharp) from the vinyl group, at  $1750\text{cm}^{-1}$  the stretching vibration for  $\text{C}=\text{O}$  from aldehyde, at  $2973\text{cm}^{-1}$  and  $1382\text{cm}^{-1}$  are the asymmetric vibrations of  $\text{CH}_3$  in alkanes, at  $1163\text{cm}^{-1}$  the vibrations of  $-\text{CH}_2$  in alkanes, at  $2315\text{cm}^{-1}$  is located the band of  $\text{O}=\text{C}=\text{O}$  and  $-\text{H}-\text{C}=\text{O}$ , and at  $3250\text{cm}^{-1}$  are located the vibration of  $\text{OH}$  groups. The MS curves in Figure 3 confirm a

decomposition process starting at  $70^\circ\text{C}$ , in which the components are eliminated until  $375^\circ\text{C}$ .

Taking into consideration the results previously discussed, the decomposition steps of the molecular precursor sample are:

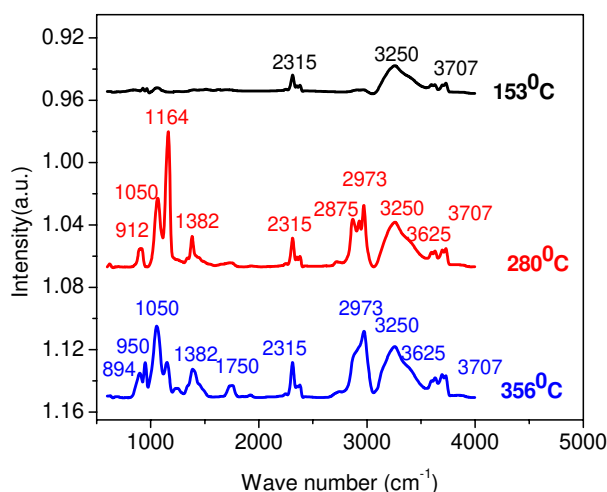
- an evaporation process (4% weight loss), in the range of  $\text{RT} \sim 100^\circ\text{C}$ ;
- the evaporation of some amount of adducts existing in the precursor sample, between  $100\text{-}170^\circ\text{C}$ ;
- the main decomposition of cluster with the lost of majority of ethoxy groups and formation of other smaller clusters, between  $200\text{-}320^\circ\text{C}$ ;



- the final decomposition of the clusters with the loss of last ethoxy groups and formation of hafnium oxide, between 320 - 375°C;
- the elimination of CH<sub>3</sub>-CH<sub>2</sub> and CH<sub>2</sub>=CH· radicals is demonstrated by both MS and FTIR spectra;
- for a better understanding of the decomposition mechanism of Hf-ethoxide molecular precursor, additional characterization of intermediaries products of the thermal decomposition steps mentioned before will be performed, using NMR and FTIR analysis methods.

**Table 1.** TGA-DTG-DSC data of hafnium ethoxide decomposition

ΔT (°C)	T <sub>max</sub> DSC peak (°C)	DSC peak	Weight loss (TG) (%)	Gas products (m/e values)
35-123	86	Endo	4	H <sub>2</sub> O (m/e=18)
123-170	153	Endo	2	2 CH <sub>3</sub> -CH <sub>2</sub> - (m/e=29) 2 CH <sub>2</sub> =CH- (m/e=27)
200-320	280	Endo	60	CH <sub>3</sub> -CHO (m/e=44)
320-375	356	Endo	10	CO <sub>2</sub> (m/e=44) CH <sub>3</sub> -CH <sub>2</sub> - (m/e=29) CH <sub>2</sub> =CH- (m/e=27) C <sub>2</sub> H <sub>2</sub> - (m/e=26) OH- (m/e=17) CH <sub>3</sub> - (m/e=15) CH- (m/e=13) H <sub>2</sub> (m/e=2)



**Fig. 4.** FTIR absorption spectra of gas products resulted from thermal decomposition of hafnium ethoxide

## Conclusions

The thermal decomposition of hafnium ethoxide precursor was investigated by TG-DTG-DSC analysis from room temperature to 600°C in nitrogen atmosphere, coupled with Fourier transformation infrared spectroscopy and mass spectrometry analysis of gas products.

Hafnium ethoxide molecular precursor decompose in four steps below 356°C, and can be used for sol-gel synthesis of HfO<sub>2</sub> polycrystalline thin films or hybride nanocomposite thin films. From mass spectroscopy and FTIR data results that the loss of ethoxy groups from the molecular precursor occurs in the decomposition steps between 200 and 375°C. That suggests that in different steps, ligands from different coordination spheres are lost.

## Acknowledgements

This work was supported by projects FP7-POINTS No. 263042 and 156EU-POINTS.

The work of Elena-Emanuela Valcu was supported by Project SOP HRD – TOP ACADEMIC 78622.

## References

- [1]. Wang J, Li HP, Stevens RJ - Mat Sci 27:5397, (1992).
- [2]. Haussa M, Pantisano L, Ragnarsson LA, Degraeve R, Schram T, Purtois G, De Gendt S, Grosenken G, Heyns MM - Mat Sci Eng R51:37, (2006).
- [3]. Bersuker G, Zeitzoff P, Brown G, Huff HR - Mater Today 7(1):26, (2004).
- [4]. Brezesinski T, Smarsly B, Imura K, Grosso D, Boissiere C, Amenitsch H, Antoinietti M, Sanchez C - Small 1:889, (2005).
- [5]. Supplit R, Husing N, Gross S, Bernstoff S, Puchberger M - Eur J Inorg Chem 18:2797, (2007).
- [6]. Villanueva-Ibanez M, Le Luyer C, Marty O, Mugnier J - Opt Mater 24(1-2):51, (2003).
- [7]. Villanueva-Ibanez M, Le Luyer C, Parola S, Marty O, Mugnier J - Rev Adv Mater Sci 5:296, (2003).
- [8]. Boher P, Defranciaux C, Heinrich P, Wolsenholme J, Bender H - Mat Sci Eng B109:64, (2004).
- [9]. Ferrari S, Modreanu M, Scarel G, Fancinelli M - Thin Solid Films 450:124, (2004).
- [10]. Hausmann DM, Gordon RG - J Cryst Growth 249:251, (2003).
- [11]. Kim YW, Roh Y, Yoo JB, Kim H - Thin Solid Films 515:2984, (2007).
- [12]. Essary C, Howard JM, Craciun V, Craciun D, Singh RK - Thin Solid Films 450:111, (2004).
- [13]. Wang SJ, Lim PC, Huan ACH, Liu CL, Chai JW, Chow SY, Pan JS, Li Q, Ong K - App Phys Lett 82-13:2047, (2003).
- [14]. Lee PF, Dai JY, Chen HLW, Choy CL - Ceram Int 30:1267, (2004).
- [15]. Fang Q, Zhang JY, Wang Z, Modreanu M, O'Sullivan BJ, Hurley PK, Leedham TL, Huywel D, Audier MA, Jimenez C, Senateur JP, Boyd JW - Thin Solid Films 453-454:203, (2004).
- [16]. Fang Q, Zhang JY, Wang ZM, He G, Yu J, Boyd JW - Microel Eng 66:621, (2003).



- [17]. He JQ, Teren A, Jia CL, Ehrhart P, Urban K, Waser R, Wang RH - *J Cryst Growth* 262:295, (2004).
- [18]. Pereira L, Maques A, Aguas H, Nevedev N, Georgiev D, Fortunato E, Martinis R - *Mat Sci Eng B*109:8917, (2004).
- [19]. Lee BH, Kang L, Nieh R, Qi WJ, Lee JC - *App Phys Lett* 76-14:1926, (2000).
- [20]. Gruger H, Kunath Ch, Kurth E, Sorge S, Pufe W, Pechstein T. - *Thin Solid Films* 447-448:509, (2004).
- [21]. He G, Fang Q, Liu M, Zhu LO, Zhang LD - *J Cryst Growth* 268:155, (2004).
- [22]. Nishide T, Honda S, Matsuura M, Ide M - *Thin Solid Films* 37:61, (2000).
- [23]. Shimada S, Sato T - *Carbon* 40:2469, (2002).
- [24]. Yu JJ, Fang Q, Zhang JY, Wang ZM, Boyd IW - *App Surf Sci* 208-209:676, (2003).
- [25]. Shimizu H, Asayama K, Kawai N, Nishide T - *Japan J Appl Phys* 43:6992, (2004).
- [26]. Shimizu H, Sato T, Konagai S, Ikeda M, Takahashi T, Nishide T. - *Jpn J Appl Phys* 46:4209, (2007).
- [27]. Takahashi T, Nishide T - *J Ceram Soc Jpn Suppl* 112-1 PacRim5 Special Issue 112(5):S234-S238, (2004).
- [28]. Nishide T, Meguro T, Suzuki S, Yabe T, - *J Ceram Soc Jpn* 113:77, (2005).
- [29]. Blanc P, Hovnanian N, Cot D, Larbot A - *J Sol-Gel Sci Technol* 17:99, (2000).
- [30]. Aoki Y, Kunitake T, Nakao A - *Chem Mater* 17:450, (2005).
- [31]. Goncalves RR, Carturan G, Zampedri L, Ferrari M, Montagna M, Chiasera A, Righini GC, Pelli S, Ribeiro SLJ, Messaddaq Y - *Appl Phys Lett* 81-1:28, (2002).
- [32]. Phani AR, Passacantando M, Santucci S - *J Non-Cryst Solids* 353:663, (2007).
- [33]. Tardy J, Erouel M, Deman AL, Gagnaire A, Teodorescu V, Blanchin MG, Canut B, Barau A, Zaharescu M. - *Microel Reliab* 47:372, (2007).
- [34]. Zaharescu M, Teodorescu VS, Gartner M, Blanchin MG, Barau A, Anastasescu M. - *J Non-Cryst Solids* 354:409, (2008).
- [35]. Mayer M - SIMNRA Users Guide, Report IPP 9/113, Max, (1997).
- [36]. Sergej Paskoa, Liliane G. Hubert-Pfalzgraf, Adulfas Abrutisb, T - *Materials Letters* 59, 1836- 1840, (2005).

MANUSCRISELE, CARŢILE ŞI REVISTELE PENTRU SCHIMB, PRECUM SI ORICE  
CORESPONDENTE SE VOR TRIMITE PE ADRESA:

MANUSCRIPTS, REVIEWS AND BOOKS FOR EXCHANGE COOPERATION, AS WELL  
AS ANY CORRESPONDANCE WILL BE MAILED TO:

LES MANUSCRIPTS, LES REVUES ET LES LIVRES POUR L'ECHANGE, TOUT AUSSI  
QUE LA CORRESPONDANCE SERONT ENVOYES A L'ADRESSE:

MANUSKRIPTEN, ZIETSCHRIFTEN UND BUCHER FUR AUSTAUCH SOWIE DIE  
KORRESPONDENZ SID AN FOLGENDE ANSCHRIFT ZU SEDEN:

After the latest evaluation of the journals achieved by National Center for the Science and  
Scientometry Politics (**CENAPOSS**), as recognition of its quality and impact at national level,  
the journal is included in B<sup>+</sup> category, 215 code ([http://www.cncsis.ro/2006\\_evaluare\\_rev.php](http://www.cncsis.ro/2006_evaluare_rev.php)).

The journal is indexed in:

CSA: [http://www.csa.com/ids70/serials\\_source\\_list.php?db=mehctrans-set-c](http://www.csa.com/ids70/serials_source_list.php?db=mehctrans-set-c)

EBSCO: <http://www.ebscohost.com/titleLists/a9h-journals.pdf>

Copernicus: <http://journals.indexcopernicus.com/karta.php>

The papers published in this journal can be visualized on the "Dunarea de Jos" University  
of Galati site, the Faculty of Metallurgy, Material Science and Environment, page:  
[www.fimm.ugal.ro](http://www.fimm.ugal.ro).

**Publisher's Name and Address:**

Contact person: Antoaneta Căpraru  
Galati University Press - GUP  
47 Domneasca St., 800008 - Galati, Romania  
Phone:+40 336 130139, Fax: +40 236 461353  
Email: [gup@ugal.ro](mailto:gup@ugal.ro)

**Editor's Name and Address:**

Prof. Dr. Eng. Marian BORDEI  
Dunarea de Jos University of Galati, Faculty of Metallurgy, Materials Science and Environment  
111 Domneasca St., 800201 - Galati, Romania  
Phone: +40 336 130223, Phone/Fax: +40 236 460750  
Email: [mbordei@ugal.ro](mailto:mbordei@ugal.ro)

***AFFILIATED WITH:***

- ***ROMANIAN SOCIETY FOR METALLURGY***
- ***ROMANIAN SOCIETY FOR CHEMISTRY***
- ***ROMANIAN SOCIETY FOR BIOMATERIALS***
- ***ROMANIAN TECHNICAL FOUNDRY SOCIETY***
- ***THE MATERIALS INFORMATION SOCIETY***  
***(ASM INTERNATIONAL)***

**Annual subscription (4 issues per year)**

**Edited under the care of  
Faculty of  
METALLURGY, MATERIALS SCIENCE AND  
ENVIRONMENT**

Edited date: 30.09.2012

Issues number: 200

Printed by

Galati University Press

accredited CNCSIS

47 Domnească Street, 800036

Galati, Romania